Scuola Normale Superiore

Ph.D. Thesis

Label-free polarisation-resolved optical imaging of biological samples

Giuseppe de Vito

Advisor
Dr. Vincenzo Piazza

2016

Cover: Bertrand's Petrological Microscope,
Journal of the Royal Microscopical Society (1883) 3:413–471

"With every tool, man is perfecting his own organs, whether motor or sensory, or is removing the limits to their functioning".

Sigmund Freud, Civilization and Its Discontents, 1930.

Dedicated to my grandparents:
Peppe, Aurora, Elo and Ela.

ABSTRACT

Myelin is a biological structure present in all the gnathostomata. It is a highly-ordered structure, in which many lipid-enriched and densely compacted phospholipid bilayers are rolled up in a cylindrical symmetry around a subgroup of axons. The myelin sheath increases the electrical transverse resistance and reduces the capacitance making the saltatory conduction of action potentials possible and therefore leading to a critically improved performance in terms of nervous impulse conduction speeds and travel lengths.

Myelin pathologies are a large group of neurological diseases that often result in death or disability. In order to investigate the main causes of myelin damage and its temporal progression many microscopy techniques are currently employed, such as electron microscopy and histochemistry or fluorescence imaging. However, electron microscopy and histochemistry imaging require complex sample preparation and are therefore unsuitable for live imaging. Fluorescence imaging, as well as its derivatives, confocal and two-photon imaging, relies on the use of fluorescent probes to generate the image contrast but fluorophores and the associated sample processing, when applicable to living specimens, might nonetheless modify the biological properties of the target molecule and perturb the whole biological process under investigation; moreover, fluorescent immunostaining still requires the fixation of the cells. Coherent anti-Stokes Raman Scattering (CARS) microscopy, on the other hand, is a powerful and innovative imaging modality that permits the study of living specimens with excellent chemical contrast and spatial resolution and without the confounding and often tedious use of chemical or biological probes. This is particularly important in clinical settings, where the patient biopsy must be explanted in order to stain the tissue. In these cases it may be useful to resort to a set of label-free microscopy techniques. Among these, CARS microscopy is an ideal tool to investigate myelin morphology and structure, thanks to its abundance of CH_2 bonds.

The chemical selectivity of CARS microscopy is based on the properties of the contrast-generating CARS process. This is a nonlinear process in which the energy difference of a pair of incoming photons ("pump" and "Stokes") matches the energy of one of the vibrational modes of a molecular bond of interest. This vibrational excited state is coherently probed by a third photon ("probe") and anti-Stokes radiation is emitted.

In this thesis I shall discuss the development of a multimodal nonlinear optical setup implementing CARS microscopy together with general Four-Wave Mixing, Second Harmonic Generation and Sum Frequency Generation microscopies. Moreover, I shall present a novel polarisation-resolved imaging scheme based on the CARS process, which I named Rotating-Polarisation (RP) CARS microscopy and implemented in the same setup. This technique, using a freely-rotating pump-and-probe-beam-polarisation plane, exploits the CARS polarisation-dependent rules in order to probe the degree of anisotropy of the chemical-bond spatial orientations inside the excitation point-spread function and their average orientation, allowing at the same time the acquisition of large-field-of-view images with minimal polarisation distortions. I shall show that RP-CARS is an ideal tool to investigate the highly-ordered structure of myelinated nervous fibres thanks to the strong anisotropy and symmetry properties of the myelin molecular architecture.

I shall also demonstrate that this technique allows the fully label-free assessment of the myelin health status both in a chemical model of myelin damage (lysophosphatidylcholine-exposed mouse nerve) and in a genetic model (twitcher mouse) of a human leukodystrophy (Krabbe disease) while giving useful insights into the pathogenic mechanisms underlying the demyelination process. I shall also discuss the promises of this technique for applications in optical tractography of the nerve fibres in the central nervous system and for the investigation of the effects of ageing on the peripheral nervous system. Moreover, I shall demonstrate by means of numerical simulations that RP-CARS microscopy is extremely robust against the presence of scatterers (such as lipid vesicles, commonly found in the peripheral nervous system). Finally, I shall discuss the results of the exploitation of my multimodal setup in a different area at the boundary of biophysics and nanomedicine: the observation of the internalization of different kinds of nanoparticles (boron-nitride nanotubes, barium-titanate nanoparticles and barium-titanate-core/gold-shell nanoparticles) by cultured cells and the demonstration of the nanopatterned nature of a structure built with two-photon lithography.

CONTENTS

1 INTRODUCTION 1
- 1.1 Microscopy 1
- 1.2 Coherent Anti-Stokes Raman Scattering 3
  - 1.2.1 CARS effect 3
  - 1.2.2 CARS microscopy 6
  - 1.2.3 Examples of CARS-microscopy applications 8
- 1.3 Myelin and its visualisation 12
  - 1.3.1 Myelin 12
  - 1.3.2 Current and emerging techniques for myelin microscopy 15
- 1.4 The CARS polarisation-dependent effect 17
  - 1.4.1 Observation of the polarisation-dependent effect 17
  - 1.4.2 The polarisation-dependent "artefact" in myelin 20
  - 1.4.3 Polarisation-dependent effects as a way to study myelin 21

2 MULTIMODAL SETUP 23
- 2.1 CARS-microscope setup 23
  - 2.1.1 Basic design 23
  - 2.1.2 Rotating-Polarisation system 25
  - 2.1.3 Theory 26
  - 2.1.4 Experimental validation of the RP-system 29
- 2.2 Improvement of the RP-CARS setup 31
  - 2.2.1 Generation of the incoming beams 31
  - 2.2.2 Fast-scanning technique 35
  - 2.2.3 Large-field polarisation-resolved laser scanning microscopy 36
  - 2.2.4 Experimental validation of the large-field scanning technique 42
- 2.3 Pulse characterisation 44
  - 2.3.1 Theory 45
  - 2.3.2 Experimental optimisation of the spectral resolution 48

3 OBSERVATIONS 53
- 3.1 Visualisation and optical tractography of myelinated fibres 53
  - 3.1.1 Myelin visualisation 53
  - 3.1.2 Optical tractography 54
- 3.2 Optical readout of myelin health in a chemical-damage model 58

3.2.1 Introduction 58
3.2.2 Theory 58
3.2.3 Results 62
3.3 Optical readout of myelin health in a genetic model of a leukodystrophy 67
3.3.1 Introduction 67
3.3.2 Results 68
3.3.3 Discussion 77
3.4 Effects of ageing on the myelinated fibres 79
3.4.1 Introduction 79
3.4.2 Results and Discussion 80

4 SIMULATIONS 83
4.1 Introduction 83
4.2 Code development 84
4.3 Results 87
4.4 Conclusions 91

5 OTHER APPLICATIONS 93
5.1 Internalisation of boron nitride nanotubes 93
5.2 Internalisation of barium-titanate nanoparticles 94
5.3 Internalisation of barium-titanate-core/gold-shell nanoparticles 98
5.4 Imaging of nanocomposite scaffold 99

6 CONCLUSIONS AND FUTURE DEVELOPMENTS 103
6.1 Conclusions 103
6.2 Future developments 104

A CODE 107

LIST OF PUBLICATIONS 119

ACKNOWLEDGEMENTS 121

BIBLIOGRAPHY 122

INDEX 155

LIST OF FIGURES

Figure 1.1 Energy diagrams of degenerate FWM processes and of the resonant CARS process. 4
Figure 1.2 Phase-matching condition for the degenerate FWM process. 5
Figure 1.3 Fingerprint and multimodal imaging of murine liver tissue. 10
Figure 1.4 CARS imaging of plant wax. 11
Figure 1.5 Three-dimensional representation generated from the multimodal imaging of a geological sample. 11
Figure 1.6 Scheme of a CNS myelinated-fibre. 13
Figure 1.7 Myelin structure scheme at increasing magnifications. 14
Figure 1.8 Examples of the polarisation-dependent effect in myelin imaging. 18
Figure 1.9 CARS image of a single lipid bilayer. 19
Figure 1.10 CARS images of normal and damaged myelin sheaths acquired with vertical and horizontal excitation polarisations. 21
Figure 2.1 Schematic representation of the initial CARS microscope. 24
Figure 2.2 Spectrum collected from a $BaTiO_3$ nanoparticle. 25
Figure 2.3 Schematic representation of the first RP-CARS setup. 27
Figure 2.4 Polarisation-dependent artefacts. 30
Figure 2.5 RP-CARS imaging of single nerve axon. 31
Figure 2.6 Second RP-CARS setup and detail of the laser-scanning optics. 34
Figure 2.7 Set and real position of the fast-scanning galvanometric mirror. 38
Figure 2.8 Nonresonant RP-CARS images of the glass bottom of a WillCo-dish plate taken with and without the compensation lens. 41
Figure 2.9 Large-scale RP-CARS image of a couple of mouse-nerve rootlets at their point of emergence from the spinal cord. 43
Figure 2.10 Box plot of the difference between the ϕ values of the myelin CH_2 bonds and the spatial orientation angles. 44
Figure 2.11 SEM image of barium-titanate-core/gold-shell nanoparticles. 49
Figure 2.12 CARS spectra of liquid methanol. 51
Figure 3.1 High resolution CARS images of Schmidt-Lanterman incisures. 54
Figure 3.2 Large-scale, high-resolution CARS image of a lumbar transversal section of an EAE rat spinal cord. 55

Figure 3.3 Small scale RP-CARS image of a longitudinal section of myelinated nerve fibres in mouse sciatic nerve. 56
Figure 3.4 Large-scale, high-resolution RP-CARS image of a coronal section of the mouse brain hyppocampus. 57
Figure 3.5 Effects of disorder on RP quantities. 61
Figure 3.6 Correlation plot between the g-ratio and the effective angle $\langle\alpha\rangle$. 63
Figure 3.7 Explanted-sciatic-nerve myelinated fibres imaged by RP-CARS after lyso-PtdCho exposition. 65
Figure 3.8 CARS images of sciatic nerve optical longitudinal sections of WT and TWI mice. 69
Figure 3.9 RP-CARS images of sciatic-nerve longitudinal sections of WT and TWI mice. 70
Figure 3.10 Graph of the average A values of WT and TWI mice of different ages. 71
Figure 3.11 Correlation plot between the average α value of manually thresholded slices and their average A_{dc} value. 73
Figure 3.12 Frequency histograms of the α values in z-stacks representative of the WT condition and of the presymptomatic and symptomatic TWI conditions. 74
Figure 3.13 TEM images of Schwann-cell wrappings in the sciatic nerve of TWI and WT mice. 76
Figure 3.14 RP-CARS analysis of ageing sciatic nerves. 81
Figure 4.1 Schematic representation of Huygens-Fresnel plane wavelets in nonscattering and scattering media. 84
Figure 4.2 Schematics of the simulated samples. 86
Figure 4.3 Sizes of the simulated myelinated fibres and the scattering particle. 87
Figure 4.4 Simulated imaging of the large-diameter myelinated fibre. 88
Figure 4.5 Simulated imaging of the small-diameter myelinated fibre. 89
Figure 4.6 Comparison of the distorting effects induced by the presence of the scattering particle on the α value when linear or circular polarisation is employed. 90
Figure 4.7 Effect of the objective NA on the α value. 91
Figure 5.1 Multimodal image of SH-SY5Y cells treated with BNNTs. 95
Figure 5.2 BTNP cell-internalisation assessment. 97

Figure 5.3 Multimodal imaging of the Ormocomp structure and of the Ormocomp/BTNPs structure. 101

LIST OF TABLES

Table 2.1 Explicit expressions of the coefficients displayed in Eq. 2.23. 47
Table 2.2 Pulse parameters before and after the chirp optimisation. 50

LISTINGS

Listing 1 Custom-made Python software application used to load the raw microscopy data and save them as tiff files. 107
Listing 2 Custom-made Python software application used to compute the average α value for each z-stack (A). 111
Listing 3 Custom-made Python software application used to compute the resultant length (β) of the ϕ values on different spatial scales. 113

ACRONYMS

AP Action Potential

BNNTS boron nitride nanotubes

BTNPS Barium Titanate Nanoparticles

CARS Coherent anti-Stokes Raman Scattering

CNS Central Nervous System

DM Dichroic Mirror

EAE Experimental Autoimmune Encephalomyelitis

FROG Frequency-Resolved Optical Gating

FWHM Full Width at Half Maximum

FWM Four Wave Mixing

GALC galactocerebrosidase

GDD Group Delay Dispersion

BATIO$_3$@GOLDSHELLS barium titanate core-gold shell nanoparticles

HF Huygens-Fresnel

HF-WEFS Huygens-Fresnel Wave-based Electric Field Superposition

HS Hall-effect Sensor

HSV Hue, Saturation, Value

KD Krabbe Disease

LYSO-PTDCHO lysophosphatidylcholine

MBP Myelin Basic Protein

MRI Magnetic Resonance Imaging

MSCS Mesenchymal Stem Cells

NA Numerical Aperture

OPO Optical Parametric Oscillator

PBS Phosphate Buffer Saline

PMT photomultiplier tube

PNS Peripheral Nervous System

PR Polarisation Resolved

PSF Point Spread Function

PSY psychosine

RGB Red, Green, Blue

RP Rotating Polarisation

SCG supercontinuum generator

SEM Scanning Electron Microscopy

SFG Sum Frequency Generation

SHG Second Harmonic Generation

SNR Signal to Noise Ratio

SRG Stimulated Raman Gain

SRL Stimulated Raman Loss

SRS Stimulated Raman Scattering

TEM Transmission Electron Microscopy

THG Third Harmonic Generation

TI-SA Titanium Sapphire

TPF Two-Photon Fluorescence

TWI twitcher

WT Wild-Type

1 INTRODUCTION

In this chapter I shall first very briefly illustrate the field of optical microscopy and then I shall focus specifically on CARS microscopy, with some examples of its modern implementations. After that, I shall discuss the myelin structure and function, together with some current limitations in its visualisation. I shall conclude by describing the polarisation-dependent effect in CARS microscopy, how it affects the myelin visualisation and how it can be fruitfully exploited rather than suppressed.

1.1 MICROSCOPY

Modern microscopy started in 1677 with the observation of *animalcules* by Antony van Leeuwenhoek [1]. At first it was intended to be a tool aimed at merely increasing the resolving power and magnification of the human eye. However in the 20th century new optical imaging modalities arose, including fluorescence microscopy: invented in 1913 [2], it was first used in biology in 1941 [3] to immuno-label pneumococci bacteria. The possibility to generate image contrast based on extremely specific sample properties transformed microscopy into a powerful analytical technique.

In the last few decades the introduction of confocal scanning fluorescence microscopy [4], together with the development of a broad range of specific fluorophores, has enabled high-resolution imaging with biological selectivity and microenvironmental sensitivity [5], providing enormous benefits in the use of light microscopy for biology research. Further modern developments of fluorescence techniques allow e.g. to observe single molecules in live cells [6–15], to overcome the Abbe spatial resolution limit [16–31] and to visualise in real time the whole-brain nervous activity in live animals with cellular resolution [32–39]. The improvement of fluorescent sensors [5], on the other hand, has enabled us to detect with high precision the concentration and the dynamics of a broad range of ions in cells or in the extracellular environment, such as chloride [40–47] or calcium ions [48–62]. Moreover, recent developments allow us to detect with submicrometric resolution physical or chemical local properties such as pH [40, 56, 63–67], oxygenation [68–70], polarity [71–74] and viscosity [75–77] of the medium. In addition, the conjugation of the fluorophore with a monoclonal antibody permits the achievement of a tremendous biological selectiv-

ity, allowing for the discrimination of similar macromolecules that differ even only by a single small post-translational modification [78, 79].

Fluorescence imaging techniques require a fluorescent label to be attached to (or to interact with) the biomolecule of interest in one of the two following ways: the fluorophores can be either genetically expressed by the cells or exogenously introduced in them or in the surrounding tissue [80]. In order for a fluorophore to be expressed by the cells, the cell (or its progenitors) must be transfected or transduced beforehand with its encoding gene. Although both the introduction of the fluorophore or the introduction of its gene and the presence of the fluorophore itself can, in some cases, alter the biological properties of the sample, these issues are usually addressed in experimental settings by carefully monitoring the sample and by thoughtfully comparing the results with data from control experiments.

There are, however, some particular cases where it is not practical or not desirable to perform sample labelling, because it may be time-consuming or problematic. This is particularly true in clinical settings, where the patient biopsy must be explanted in order to stain the tissue. In these cases it may be useful to resort to a set of label-free microscopy techniques, the most important being autofluorescence, Second Harmonic Generation (SHG), Sum Frequency Generation (SFG), Third Harmonic Generation (THG), and Raman imaging and its derived techniques.

The first label-free microscopy technique discovered was autofluorescence, described in 1904 by August Kohler [81]. This technique, together with its two-photon variant [82, 83], is capable of visualising the endogenous fluorescent molecules. Unfortunately, autofluorescence microscopy is limited to a relative small and predetermined set of molecules that are in a sufficiently high concentration in the cells or in the tissues, such as: tryptophan [84, 85], NAD(P)H [86, 87], melanin [88, 89], and elastin [90, 91].

The SHG effect was the first optical nonlinear effect to be proposed as a contrast-generation mechanism for microscopy [92] and one of the first demonstrated [93]. The successive development of pulsed light sources greatly facilitated the experimental implementations of nonlinear microscopy techniques [94]. SHG and SFG require a non-centrosymmetric medium [95] and therefore only the biological structures that have this peculiar structural property (such as collagen fibres [96, 97] or striated muscle myosin [97, 98]) can be visualised. The THG signal, on the other hand, is generated by interfaces, where there is a strong refractive index mismatch [95, 99], and it is therefore frequently used to observe lipid bodies [100] or particular blood pigments [101].

Unlike the aforementioned modalities, Raman microscopy [102] is another label-free imaging modality capable of detecting specific types of chemical bonds [103], i.e. to provide a chemical-based contrast, and therefore in principle it is not limited to a particular subset of endogenous biological components in the sample. However,

the potential of spontaneous Raman scattering is not fully exploited due to its poor cross section leading to a very low Signal to Noise Ratio (SNR) and, therefore, to the necessity of long acquisition times that make it impractical for high-resolution real-time biological imaging [104].

Coherent anti-Stokes Raman Scattering (CARS) microscopy – together with its derived technique: Stimulated Raman Scattering (SRS) – on the other hand, is an innovative imaging modality based on a Coherent Raman Scattering process that maintains the chemical contrast typical of spontaneous Raman and therefore its visualisation capabilities are not limited to a restricted subset of endogenous molecules (like autofluorescence) or to particular molecular symmetry or nanocomposition requisites (like SHG/SFG or THG). CARS offers larger SNRs and therefore shorter acquisition times with respect to spontaneous Raman scattering.

1.2 COHERENT ANTI-STOKES RAMAN SCATTERING

1.2.1 CARS effect

The CARS process was observed for the first time in 1965 in the Scientific Laboratory at Ford Motor Company [105] and it is a particular type of the Four Wave Mixing (FWM) process. In the FWM process, three frequencies (ω_1, ω_2, and ω_3) interact in a nonlinear medium and generate a fourth frequency (ω_4). If two of the three interacting frequencies are equal ($\omega_1 = \omega_3$, as in the common two-colour CARS implementation), then it is named "degenerate FWM". FWM is a parametric process, i.e. the total energy and the total momentum of the incoming and generated electrical fields are conserved and therefore the nonlinear medium acts as a mediator, theoretically without energy absorption. The case:

$$\omega_4 = 2\omega_1 - \omega_2, \tag{1.1}$$

with $\omega_1 > \omega_2$, is of particular interest, since it comprises the CARS process. The energy diagrams of this particular case of degenerate FWM are presented in Figs. 1.1A (in its two-photon variant) and 1.1B, while the diagram of the phase-matching condition is depicted in Fig. 1.2. The theory of this process is treated in great detail in Ref. [106].

The source of the FWM (as well as CARS) signal is the induced third-order medium polarisation:

$$\boldsymbol{P}^{(3)} = \varepsilon_0 X^{(3)} \boldsymbol{E_1} \cdot \boldsymbol{E_2} \cdot \boldsymbol{E_3} \tag{1.2}$$

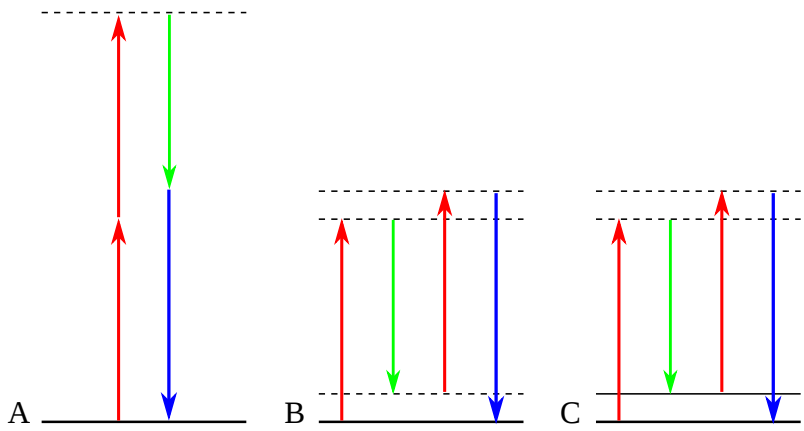

Figure 1.1: Energy diagrams of degenerate FWM processes *(A,B)* and of the resonant CARS process *(C)* in the two-colour implementation. Different colours label photons with different wavelengths: in *(C)* pump photons are depicted in red, Stokes in green and anti-Stokes in blue. The energy ground state is represented by a thick continuous line. In *(C)*, unlike *(B)*, the energy difference of the pump and the Stokes photons matches a vibrational excited state of the molecule (thin continuous line).

where ε_0 is the electrical permittivity of the vacuum, $X^{(3)}$ is the third order susceptibility tensor and the vectors $\boldsymbol{E_i}$ are the incoming electrical fields corresponding to frequencies ω_i (here $i = \in 1, 2, 3$). Under the condition stated in Eq. 1.1 and if the incident fields are approximated as plane waves (with amplitudes A_i) linearly polarised along the x axis and collinearly propagating along the z-axis in a medium of finite length L along the propagation axis, then Eq. 1.2 can be written as the follow:

$$\begin{aligned} &\boldsymbol{P}^{(3)}(z,t) = \\ &\quad \frac{\varepsilon_0}{8} X^{(3)} A_1^2(z) A_2^*(z) \exp\{i[(2k_1 - k_2)z - \omega_4 t]\}\hat{\boldsymbol{x}} + c.c. \end{aligned} \tag{1.3}$$

where k_i are the wavenumbers.

Following Eq. 1.3, the intensity of the FWM signal (I_4) generated from the induced third-order medium polarisation is proportional to:

$$I_4(\Delta k) \propto \left| X^{(3)} \right|^2 I_1^2 I_2 L^2 \operatorname{sinc}^2\left(\frac{\Delta k L}{2}\right) \tag{1.4}$$

where I_1 and I_2 are the intensities of the beams at frequencies ω_1 and ω_2, respectively; sinc is the cardinal sine function ($\operatorname{sinc}(x) = \sin(x)/x$) and $\Delta k = 2k_1 - k_2 - k_4$ is the mismatch among the wavenumbers of the photons involved in the process. The expression in Eq. 1.4 is maximised when $\operatorname{sinc}(0) = 1$, i.e. when

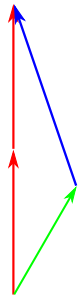

Figure 1.2: Phase-matching condition for the degenerate FWM process. The wavevectors of the beam at frequency ω_1, of the beam at frequency ω_2 and of the beam at frequency ω_4 are depicted in red, green and blue, respectively.

$\Delta kL = 0$. This condition implies that for thick samples (large L) the wavenumber mismatch Δk described in Eq. 1.4 must be small ($\Delta k \ll 2\pi / L$) to have significant FWM signal generation. In this case, the signal propagates mainly in the forward (trans) direction, as the backward-propagating signal is suppressed by destructive interference [107]. On the other hand, for thin samples, when the length of the nonlinear interaction volume L is small (e.g. comparable to the pump beam wavelength or smaller), the destructive interference is not complete (the sinc function in Eq. 1.4 is still close to one) and therefore a non-negligible amount of backward propagating FWM signal is also generated [107] and can be detected in the epi-direction [108]. In a similar fashion, a discontinuity of $X^{(3)}$ in the nonlinear interaction volume could be considered as an extremely small object and therefore it induces the generation of backward propagating signal [109].

In the CARS process the pair of incoming photons are named "pump" and "Stokes" and, unlike the general FWM process, are exploited to coherently and resonantly excite selected vibrational levels of a population of molecules. This is achieved by choosing the beams so that their frequency difference (the beat frequency) matches a vibrational frequency of the oscillating dipoles of interest, as shown in Fig. 1.1C. The third photon is named "probe" and it comes from the same source as the pump in the most frequently used two-colour CARS implementations. This photon coherently probes the phonon population of the vibrational mode, generating anti-Stokes emission at frequency $\omega_{aS} = 2\omega_p - \omega_S$, where ω_p and ω_S (i.e. the frequencies of the pump and Stokes beams respectively) play the role of ω_1 and ω_2 in Eq. 1.1.

In spectral regions where the Raman peaks are well separated, $X^{(3)}$ can be written as the sum of a resonant and a nonresonant term [110]:

$$X^{(3)}(\omega_{aS};\omega_p,-\omega_S,\omega_p) = X^{(3)}_{NR} + \frac{X^{(3)}_R}{\omega_v - (\omega_p - \omega_S) - i\gamma_v} \tag{1.5}$$

where ω_v is the vibrational frequency of the oscillating dipole of interest and γ_v the spectral bandwidth. $X^{(3)}_{NR}$ represents the non resonant contribution to the third-order susceptibility, it is independent from the frequency and originates from FWM processes that occur concurrently with the CARS process [108]. For the sake of readability, in the following I shall use the shorthand notation $X^{(3)}(\Omega)$ in place of $X^{(3)}(\omega_{aS};\omega_p,-\omega_S,\omega_p)$.

Combining Eqs. 1.5 and 1.4 yields:

$$I(\omega_{aS}) \propto \left|X^{(3)}_{NR}\right|^2 + \left|X^{(3)}_R(\Omega)\right|^2 + 2X^{(3)}_{NR}\,\mathrm{Re}\,X^{(3)}_R(\Omega) \tag{1.6}$$

where $\mathrm{Re}\,X^{(3)}_R(\Omega)$ is the real part of $X^{(3)}_R(\Omega)$. The first component of Eq. 1.6 is the cause of the so-called "non resonant background" that decreases the signal-to-background ratio in the CARS spectra and the contrast in CARS imaging. The second component is the resonant term and it dominates $I(\omega_{aS})$ when $\omega_p - \omega_S = \omega_v$. The third component is a mixing factor between the nonresonant contribution and the real part of the resonant contribution, it presents a dispersive lineshape and causes a distortion of the CARS spectrum with respect to the spontaneous-Raman-scattering spectrum. For this reason the peaks in the CARS spectrum are redshifted with respect to their spontaneous-Raman equivalents and present a negative dip at their blue end [111]. It is important to note that $I(\omega_{aS})$ is proportional to $\left|X^{(3)}\right|^2$, which means that, since $X^{(3)}$ is linearly dependent on the number of oscillators, then $I(\omega_{aS})$ depends on the square of the number of oscillating molecules, unlike spontaneous Raman scattering which is linearly proportional [112].

1.2.2 CARS microscopy

In CARS microscopy, spatially-resolved differences in the $X^{(3)}$ of the sample are used to generate magnified images [113]. The nonlinearity of the process and its vibrational selectivity are at the basis of several features of CARS microscopy, some of which are shared with other nonlinear techniques, which make it particularly suitable for biological imaging:

- It generates images with contrast based on the chemical (vibrational) properties of the sample, similarly to spontaneous Raman microscopy. Unlike the latter, however, the high SNR due to the coherent buildup of the CARS signal from dense samples allows for significantly reduced acquisition times.

- The incident-beam wavelengths employed in CARS microscopy generally reside in the near-infrared region of the spectrum. With respect to visible-light excitation, infrared light allows for larger penetration depths inside biological tissues [114], up to 300 μm.

- Thanks to the nonlinear generation of the signal, the spatial resolution is sub-diffraction limited [107] (down to approximately 250 nm).

- Since the signal is generated only in the nonlinear interaction volume, this techniques offers 3D-sectioning capability.

- Unlike Two-Photon Fluorescence (TPF) microscopy, CARS microscopy is insensitive to one-photon (auto)fluorescence backgrounds, since the generated anti-Stokes signal is blue-shifted.

- CARS imaging is not subject to photobleaching effects [115] that affect fluorescence-based microscopy, and it is therefore well suited for prolonged acquisitions.

It should be pointed out that the reduction in the image contrast caused by the nonresonant background represents a significant drawback when imaging samples with low concentrations of the target molecular oscillators. In order to address this limitation, several methods have been developed and proposed in the literature [116, 117].

The first CARS microscope was built using a non-collinear design by Duncan and collaborators in 1982 [118], and represented the first application of a nonlinear microscopy technique to biological studies. The non-collinear design increases the implementation complexity and it was superseded by Zumbush and collaborators in 1999 [114] who presented the first CARS microscope with a collinear design. This was made possible by using a high-Numerical Aperture (NA) objective lens that, thanks to the large-angle incidence cone, allows it to satisfy the phase-matching requirement. Moreover, the beam collinearity enabled for the first time the implementation of galvanometric scanning [119], which allows faster acquisition speeds compared to sample scanning.

Another important improvement in the design of CARS microscopes and their application to biological samples is represented by the implementation of epi-detection

by Cheng and collaborators [108]. In fact, CARS imaging of thick tissues is prevented in the transmitted direction by the severe scattering that light (especially in the visible range) suffers in these samples [120]. The cited authors realized that the same scattering that strongly suppresses the forward-propagating CARS transmission through the tissue, partially redirects the signal in the epi-direction allowing it to be detected by a high-NA objective.

An important technique derived from CARS is SRS [121, 122]. In this technique, the sample is illuminated simultaneously by the pump and the Stokes beams, similarly to CARS, but the detected signal is represented by the decrease in intensity of the pump beam – named Stimulated Raman Loss (SRL) – or the increase in intensity of the Stokes beam – Stimulated Raman Gain (SRG) – mediated by the nonlinear sample-light interactions. Notably, the relative change in beam intensity due to the occurrence of SRL or SRG is very small, even smaller than 10^{-4} for typical biological samples [123], and therefore its detection requires signal-modulation techniques, e.g. homodyne detection by means of lock-in amplifiers (or similar methods [124]). SRS presents several advantages over CARS [123, 125–128], one of the most relevant being the complete suppression of the nonresonant background, thanks to the fact that it does not lead to signal modulation. Other major advantages of these signal-generation processes are: the linearity of the dependence of the signal intensity on the oscillating-dipole concentration, the lack of the emission-spectrum distortions typical of CARS spectra, and the absence of image artefacts caused by interference effects of the resonant signal with non-resonant background. However, it should be pointed out that the increased complexity of the experimental implementation of SRS with respect to original CARS makes it difficult to apply this technique in *in-vivo* settings, although proofs of principle have been reported [129] by using non-standard detectors.

1.2.3 Examples of CARS-microscopy applications

Starting from the early pioneering works [114, 118], CARS microscopy has come a long way to become nowadays a mature technique. During this process several variants in the implementation of this microscopy concept have appeared.

Among these, one particularly promising implementation is "rapid broadband fingerprint CARS imaging" recently described by Camp and collaborators [130]. In broadband CARS [131, 132] multiple molecular vibration modes are excited at the same time by exploiting broadband pump and/or Stokes beams. Therefore, the signal generated by the interaction with the probe beam contains information about the vibrational spectrum of the molecules. In Ref. [130] the authors demonstrated that a combination of a broadband and a narrowband incoming beam allows access

to the entire biologically relevant Raman window ($\approx$ 500-3500 cm^{-1}). The first part of this window (<2000 cm^{-1}) is accessed by exploiting the broadband beam both as the pump- and as the Stokes- beam (in this way the peak excitation frequency is at 0 cm^{-1}) and using the narrowband beam as probe beam, in the so-called intrapulse three-colour CARS implementation. At the same time, the second part of the window (>2000 cm^{-1}) is accessed by using the broadband beam as Stokes beam and the narrowband beam both as pump and as probe beam, in a two-colour CARS implementation. The first part of the window contains the Raman "fingerprint region" [133] that is characterised by multiple weak peaks and which can be used to discriminate the different molecular compositions or states of the sample [134]. The second part is dominated by the strong peaks of the CH_2, CH_3 and OH groups, very abundant in biological samples. The weak peaks in the fingerprint region are addressed thanks to the efficient stimulation of the Raman transitions by the intrapulse three-colour excitation and to the amplification caused by the heterodyne mixing between the signal and the nonresonant background (the Raman spectrum is then retrieved with a post-acquisition data-analysis procedure). In this way, by exploiting the spectral information present in the fingerprint region the authors are able to generate hyperspectral images with contrast based on selected Raman peaks or linear combinations of peaks, as shown in Fig. 1.3.

In recent years the potential of CARS microscopy as an imaging tool for the study of plant tissues has been increasingly highlighted. In fact, it gives access to the investigation of vegetal structures, such as epicuticular waxes (depicted in Fig. 1.4), which are difficult to address *in-vivo* by using other optical-microscopy techniques [135]. However, it should be pointed out that absorption and autofluorescence from chlorophyll and other pigments can hamper CARS imaging inside the vegetal cells [136] and, therefore, this microscopy technique is best suited for the observation of the non-pigmented structures, such as the roots.

CARS microscopy has also proven to be an extremely useful tool for the observation of inorganic samples, such as spatially-heterogeneous geological samples. A recent article [137] reported the exploitation of CARS microscopy and other nonlinear optical microscopies to observe and discriminate water and methane inclusions in samples from deep sedimentary basins and deeper crustal environments. The three-dimensional resolution given by these techniques allowed the determining of the sequence of evolving environmental conditions that the samples underwent to define, for example, the relationship of fluid inclusions with individual micro-fractures, as shown in Fig. 1.5.

As already noted in Section 1.2.1, CARS is a particular case of the FWM process. Typically, CARS microscopes are also able to exploit FWM as an additional contrast generation mechanism. This is particularly useful because a large set of different nanostructures are able to produce strong FWM signals that are compatible with

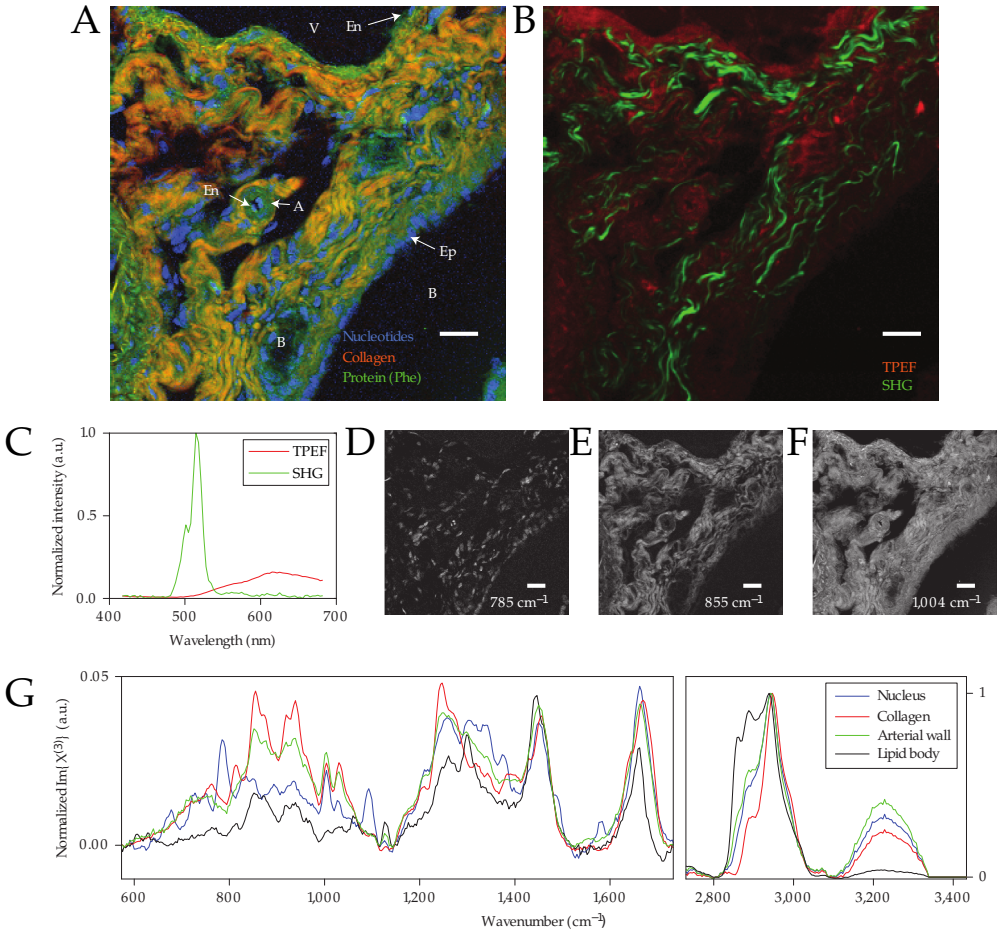

Figure 1.3: *(A)* Spectral image of a portal triad within murine liver tissue with the nuclei in blue, collagen in orange and protein content in green. A, portal artery; B, bile duct; V, portal vein; Ep, epithelial cell; En, endothelial cell. *(B)* SHG image highlighting the fibrous collagen network. *(C)* SHG spectrum for a single pixel. *(D,E,F)* Spectral images of individual vibrational modes represented by the colour channels at 785 cm^{-1} *(D)*; 855 cm^{-1} *(E)*; 1004 cm^{-1} *(F)*. *(G)* Single-pixel spectra from the nucleus (DNA), collagen fibre, arterial wall and a lipid droplet. Scale bars: 20 μm. Figure and legend text reproduced with permission from: C. H. Camp Jr, Y. Jong Lee, J. M. Heddleston, C. M. Hartshorn, A. R. Hight Walker, J. N. Rich, J. D. Lathia and M. T. Cicerone, "High-speed coherent Raman fingerprint imaging of biological tissues," *Nature photonics*, vol. 8, pp. 627-634, 2014 [130]. Copyright Nature Publishing Group.

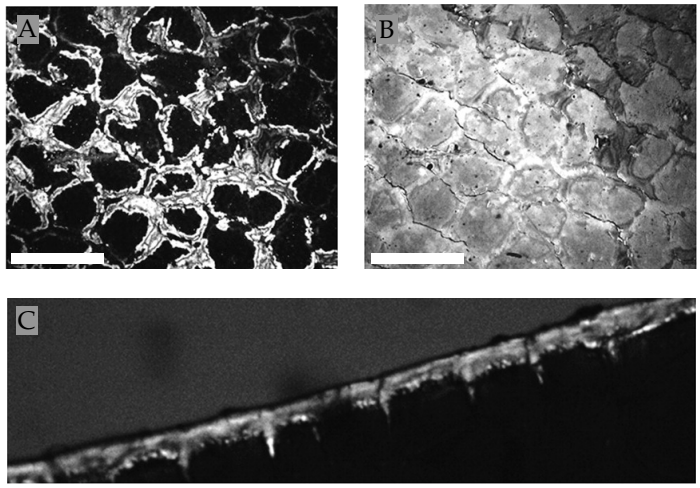

Figure 1.4: CARS imaging of the epicuticular wax of *Hoya carnosa*. *(A)* CARS image acquired in the epi-direction at 2870 cm^{-1}. *(B)* CARS image acquired in trans-direction at the same wavenumber. *(C)* Cross section of the wax layer and the cuticula acquired at 2795 cm^{-1}. Scale bar: 50 μm. Figure adapted with permission from: I. Weissflog, N. Vogler, D. Akimov, A. Dellith, D. Schachtschabel, A. Svatos, W. Boland, B. Dietzek and J. Popp, "Toward in Vivo Chemical Imaging of Epicuticular Waxes," *Plant Physiology*, vol. 154, pp. 604-610, 2010 [135]. Copyright American Society of Plant Biologists.

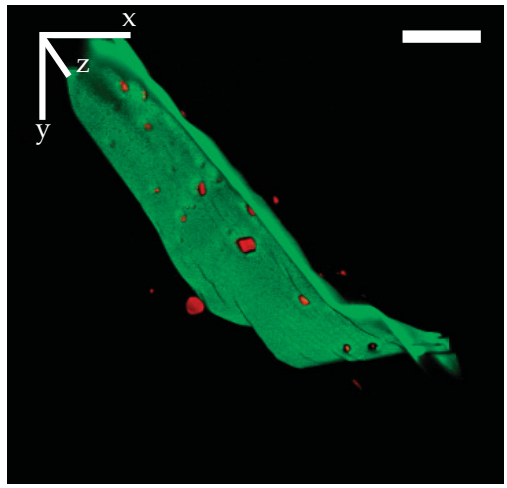

Figure 1.5: Three-dimensional representation generated from multimodal imaging of a geological sample. Red: CARS signal from CH_4-rich inclusions. Green: SHG signal from a healed microfracture. Scale bar: 20 μm. Figure reproduced with permission from: R. C. Burruss, A. D. Slepkov, A. F. Pegoraro and A. Stolow, "Unraveling the complexity of deep gas accumulations with three-dimensional multimodal CARS microscopy," *Geology*, vol. 40, pp. 1063-1066, 2012 [137]. Copyright Geological Society of America.

single-nanostructure fast imaging [138], without additional labelling. This point will be discussed more in detail in Section 5.

CARS microscopy has also been employed for functional studies, in particular to investigate selected molecular pathways in the nervous tissue. In a couple of recent articles by Fu and collaborators [139] and by Huff and collaborators [140], epi-CARS microscopy was used to visualise the myelin retraction around Ranvier nodes in the spinal cord of rats and of guinea pigs. By combining *in-vivo* and *ex-vivo* CARS observations with pharmacological manipulations, the authors demonstrated the presence of a receptor-mediated Ca^{2+} overloading and subsequent calpain activation at the basis of paranodal myelin retraction in response to glutamate excitotoxicity and high-frequency electrical stimulation.

As I shall discuss more in detail in the next Section, CARS microscopy is well suited to visualising myelin thanks to the strong CARS signal that is generated by targeting its extremely abundant CH_2 bonds [141].

1.3 MYELIN AND ITS VISUALISATION

1.3.1 Myelin

Myelin is a biological structure present in all the gnathostomata [142] that consists of a thin insulating multilamellar layer wrapped around a subgroup of axons. It was first described by Virchow in 1854 [143] and it is produced by Schwann cells in Peripheral Nervous System (PNS) and oligodendrocytes in Central Nervous System (CNS) as an extension of a modified plasma membrane, as is shown in Fig. 1.6.

Its purpose is to increase the transverse resistance and to reduce the capacitance, making possible the *saltatory conduction* of the action potential (AP) [144]. In this conduction modality ions are only exchanged across the axon membrane (thus re-generating the AP) in short uninsulated zones called "nodes of Ranvier" (shown in Fig. 1.6), spaced up to 1 mm apart, where ion channels are concentrated and exposed to the external space. *Saltatory conduction* leads to critically improved nerve-impulse propagation, with fewer ions needed to be pumped back to restore the resting potential – leading to smaller energy dissipation – and higher propagation velocities, up to two orders of magnitude.

Myelin is a highly-ordered structure, in which many alternated compacted layers of proteins and lipids are spirally rolled up around the cylindrical axon. The typical myelin-wall thickness is about 1 µm and is composed of approximately 80 wrappings [145]. The layers that compose myelin follow the structure:

"-intracellular proteins-lipid bilayer-extracellular proteins-lipid bilayer-"

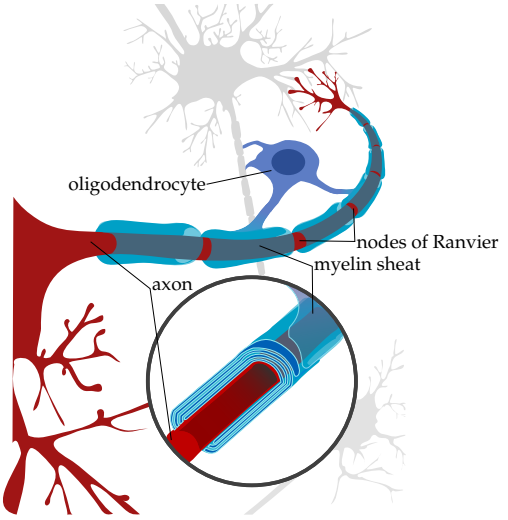

Figure 1.6: Scheme showing an axon in the CNS myelinated by an oligodendrocyte. The nodes of Ranvier are also displayed.

where the proteins are densely packed together and the lipid bilayer, with interposed transmembrane proteins, is similar in structure (but not in composition) to typical cell membranes [146]. Around 70% of the myelin dry weight is represented by lipids [144]. Among the several hundred different lipid molecules present in myelin [147], the most abundant ones are phospholipids, fatty acids, cholesterol, and sphingolipids (such as galactocerebrosides in the CNS). The remaining 30% of the myelin dry weight is composed of proteins. The most abundant myelin proteins in the CNS are the myelin basic protein and the proteolipid protein (and, to a lesser extent, the myelin-associated protein and the myelin-oligodendrocyte glycoprotein); while the most abundant ones in the PNS are the myelin basic protein, the P_0 glycoprotein, the peripheral myelin protein-22, and the P_2 protein (and, to a lesser extent, the proteolipid protein and the myelin-associated protein) [144].

The volume between the outer-face and the inner-face of the lipid bilayers is composed primarily of acyl chains oriented radially with respect to the centre of the fibre. In other words, in this arrangement the linear acyl chains of the phospholipid molecules present a perpendicular orientation with respect to the myelin wall surface. Therefore, in a myelinated nerve fibre a large number of C-C molecular bonds (composing the acyl chain backbone) are ordered around a radial axis of symmetry while the corresponding CH_2 bonds, being perpendicular to the backbone, possess an azimuthal symmetry, as shown in Fig. 1.7.

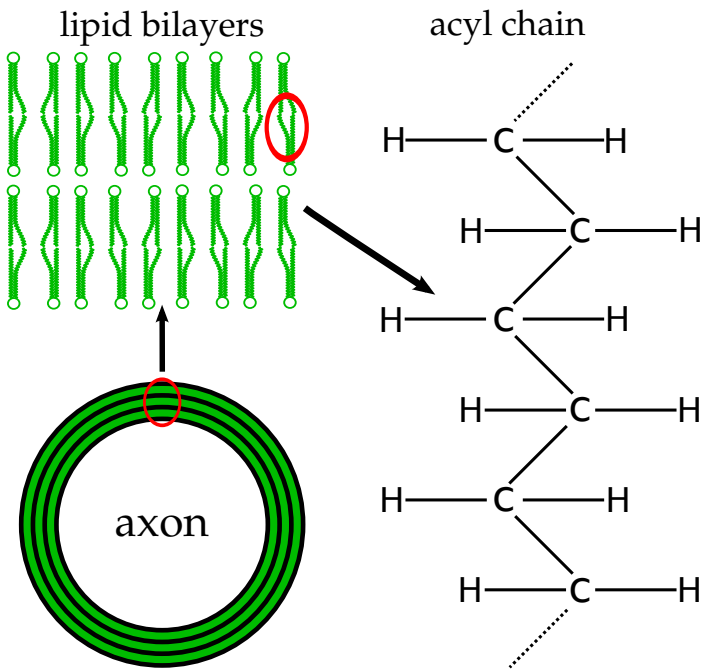

Figure 1.7: Myelin structure scheme at increasing magnifications: myelin (in green) is composed of alternated layers of lipids and proteins enrolled around the nerve axon. The lipid layers are in turn composed mainly of phospholipids, fatty acids, cholesterol and sphingolipids and interposed with transmembrane proteins. In this scheme, for the sake of clarity, only the phospholipid moiety is depicted. All the acyl chains of phospholipid bilayers are aligned in radial symmetry. The CH_2 groups that form the acyl chains are, in turn, aligned in an azimuthal symmetry, therefore their average direction is always tangential to the surface of the nerve fibre.

Myelin can be affected by several pathologies, which often result in death or inability. Myelin pathologies are classified in dysmyelinating diseases and demyelinating diseases [148]. In the former, myelin development is characterised by aberrant structure and/or composition and is therefore inherently prone to successive degeneration [149]. Dysmyelinating diseases are usually of genetic origin and are exemplified by leukodystrophies (e.g. Metachromatic leukodystrophy, Krabbe disease, Canavan disease, X-linked adrenoleukodystrophy and Alexander disease). On the contrary, in demyelinating diseases (also called myelinoclastic demyelinating diseases) normal and healthy myelin is initially formed, followed by degeneration due to several possible factors. These factors can be classified as primary when they involve the early destruction of myelin (even if a subsequent axonopathy can arise), or secondary when the demyelination is a consequence of an axonal or a neuronal damage.

The possible causes of primary demyelinating diseases are [150]:

- Inflammation, in some cases in response to an immune system hypersensitivity reaction (e.g. to infections, vaccinations or giving drugs). E.g.: multiple sclerosis, acute-disseminated encephalomyelitis and acute haemorrhagic leucoencephalitis.
- Viral infections, e.g. progressive multifocal leucoencephalopathy.
- Exposure to biological toxins or inorganic toxic substances (e.g. lead or tellurium).
- Undernourishment or dietary deficiencies (e.g. copper or B vitamins).
- Acquired metabolic alterations, frequently in association with liver diseases (e.g. central pontine myelinolysis and extrapontine myelinolysis).
- Hypoxia or ischaemia. Usually these conditions cause necrosis in the nervous tissue rather than demyelination though in rare circumstances the latter may occur.
- Mechanical compression. Often remyelination occurs when compression is removed.

For many of these pathologies medical treatment can only slow down the progress of the disease, not being able to stop it or to lead to a stable *restitutio ad integrum*.

1.3.2 Current and emerging techniques for myelin microscopy

The clinical diagnosis of several neuropathies causing secondary demyelination (e.g. chronic inflammatory demyelinating polyradiculoneuropathy [151], polyarteritis no-

dosa [152] or particular cases of Charcot-Marie-Tooth disease [153]) requires the microscopic observation of the patient's peripheral nerves.

At present, myelin and – in general – nervous-tissue observation is performed by means of many well-established imaging techniques, such as histochemistry [154–156] (also with fluorescent dyes [157, 158]), Transmission Electron Microscopy (TEM) [156, 159, 160], immunofluorescence [161, 162], and Magnetic Resonance Imaging (MRI) [163–165]. However, the first two techniques require complex sample preparation and for this reason they are unsuitable for live imaging. The third, immunofluorescence, as well as its derivatives, confocal and TPF imaging, relies on the use of fluorescent probes to generate the image contrast but fluorophores and the associated sample processing (i.e. fixation for immunostaining) might modify the biological properties of the target molecule and can perturb the whole biological process under investigation (as discussed also in Section 1.1). MRI, finally, while being capable of *in-vivo* full-body imaging, cannot afford the high spatial resolution offered by electron and optical microscopies. These, in turn, require sample staining in order to provide sufficient imaging contrast, a procedure that cannot be performed without the surgical removal of a nerve sample, causing acute sensory deficit and leading to possible long-term health problems [166].

CARS microscopy, on the other hand, is well suited to observing myelin and its pathological modification without the need for staining procedures, thanks to the strong CARS signal from the abundant CH_2 bonds [141]. CARS imaging therefore constitutes an extremely promising approach to overcoming the mentioned limitations becoming a diagnostic tool to evaluate, *in-vivo*, the health condition of myelinated fibres without damaging the nerve, provided that an optical access to the nerve is made available.

In fact, CARS imaging is already proving itself to be an extremely useful tool to study myelin in preclinical and basic research. Just to cite a few notable examples, it is worth mentioning that it was recently employed to elucidate the cellular mechanisms at the basis of the myelin alterations in glutamate excitotoxicity [139], in lysophosphatidylcholine-induced [167] and in compression-induced [168] damage and during high-frequency stimulation [140]. It is also being extensively exploited to study animal models of multiple sclerosis [169–171] and remyelination processes [172] in view of clinical diagnoses of neuropathologies [173] and also for cardiovascular diseases [174].

The extraction of quantitative morphometric parameters from CARS imaging of myelin must anyhow take into account the presence of a "polarisation-dependent artefact", exemplified in Fig. 1.8. In particular, the image contrast depends on the relative orientation of the myelin walls with respect to the polarisations of the incoming beams [175]. In the following Section I shall discuss the origin and the nature of

this artefact. I shall also show that it can be successfully exploited to extract spatially-resolved useful information about the arrangement of molecules in the sample.

1.4 THE CARS POLARISATION-DEPENDENT EFFECT

1.4.1 Observation of the polarisation-dependent effect

The presence of polarisation-dependent effects stems from the fact that the tensor $X^{(3)}$ does not depend only on the chemical nature of the sample, but also on the distribution of the dipole spatial orientations. Similar effects are present in several other microscopies, including single-photon fluorescence [177–179], TPF [180–182], label-free SHG [98, 183–186], and sample absorption [177, 187].

An example of the observation of this effect in CARS imaging is reported in Fig. 1.9, which shows a CARS image of a single lipid bilayer (the cellular membrane of an erythrocyte ghost) [188]. In this preparation a large fraction of the CH_2 molecular bonds of the phospholipid acyl chains displays an azimuthal symmetry, similarly to what happens in myelin (as discussed in Section 1.3.1). As the Figure shows, the regions of the cellular membrane where the CH_2 bonds are parallel to the incident polarisations appear brighter than those where the CH_2 bonds are perpendicular.

The polarisation dependence of the CARS signal was exploited to perform orientation analysis with Polarisation-Resolved (PR)-CARS spectroscopy [189, 190]. The first implementation of PR-CARS microscopy is described in an article from Cheng and collaborators [191] where the authors exploited the polarisation-dependent effect to demonstrate the ordered orientation of hydration water at the surface of phospholipid bilayers. They created "onion-like" structures consisting of multiple alternate layers of phospholipids and water and then observed that the polarisation-dependent effect was present both at the Raman shift corresponding to the CH_2 bonds (phospholipid) and at the one corresponding to the OH bonds (water). In the OH-case the phase of the angular dependence is perpendicular with respect to the CH_2-case, meaning that the hydration water is ordered, with the molecule symmetry axis oriented along the phospholipid C-C backbone chains.

The polarisation-dependent effect was also exploited to study the molecular structure of vegetal fibres [192, 193]. In Ref. [193] the authors used CARS and SHG PR-microscopy to demonstrate the conservation of molecular alignment of microfibrils in natural and regenerated cellulose, even after hydration.

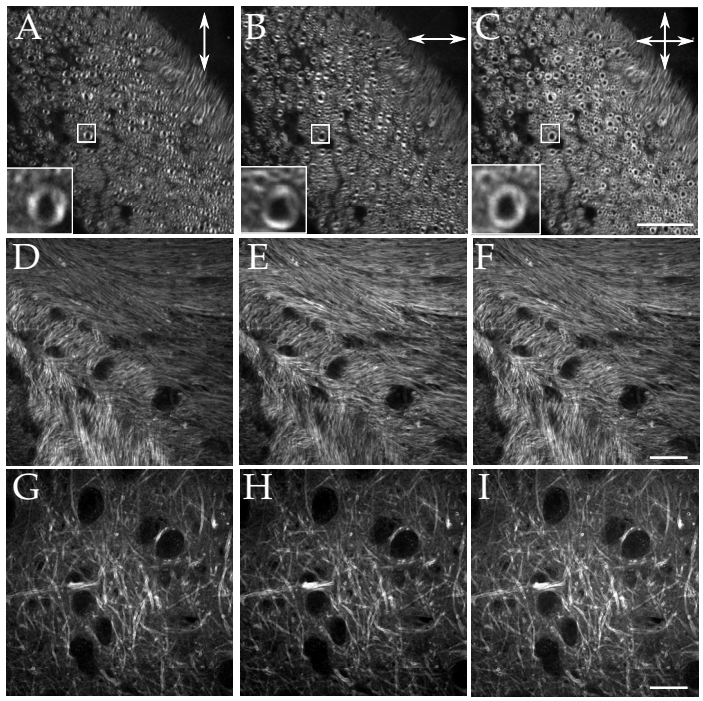

Figure 1.8: Examples of the polarisation-dependent effect in myelin imaging. *(A)*, *(D)*, and *(G)* display CARS images with vertically polarised excitations showing stronger CARS signal from vertically oriented membranes and fibres. *(B)*, *(E)*, and *(H)* display CARS images with horizontally polarised excitations showing stronger CARS signal from horizontally oriented membranes and fibres. *(C)*, *(F)*, and *(I)* display CARS images reconstructed in a post-processing passage by combining the images acquired with the two polarisations. In the reconstructed images the artefact is strongly suppressed. Scale bar: 20 μm. Figure and legend text adapted with permission from: Y. Fu, T. B. Huff, H.-W. Wang, H. Wang, and J.-X. Cheng, "Ex vivo and in vivo imaging of myelin fibers in mouse brain by coherent anti-Stokes Raman scattering microscopy," *Optics Express,* vol. 16, no. 24, pp. 19396-19409, 2008 [176]. Copyright the Optical Society of America.

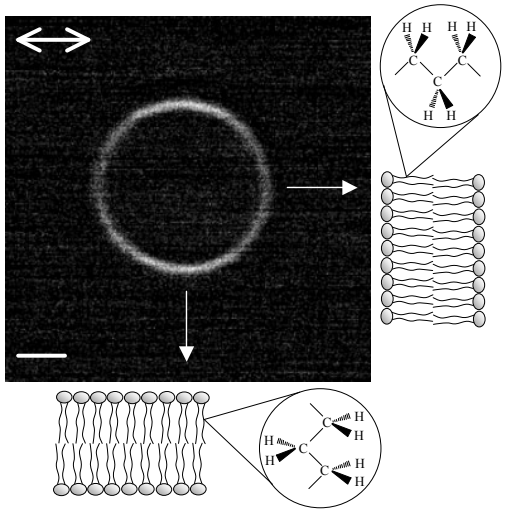

Figure 1.9: CARS image (Raman shift: 2845 cm^{-1}, acquired in the equatorial plane of the sample) of an erythrocyte ghost composed of a single lipid bilayer. The double arrow in the top-left indicates the direction of the linear polarisation of the incoming light. The two single arrows indicate the areas where the CARS signal is maximum or minimum which correspond to where the CH_2 bonds of the lipid acyl chains are parallel or perpendicular to the polarisation plane respectively, as indicated in the schemes on the right and at the bottom of the Figure. Scale bar: 2 μm. Figure reproduced with permission from: E. O. Potma and X. S. Xie, "Detection of single lipid bilayers with coherent anti-Stokes Raman scattering (CARS) microscopy," *Journal of Raman Spectroscopy*, vol. 34, pp. 642-650, 2003 [188]. Copyright John Wiley & Sons, Inc.

1.4.2 The polarisation-dependent "artefact" in myelin

As discussed in Section 1.3.1, CH_2 bonds in myelin display an azimuthal symmetry and CARS imaging of myelin walls displays a polarisation-dependent effect similar to that observed in erythrocyte ghosts [188]. This effect was observed starting from the early reports of myelin CARS imaging [176]. However it was first interpreted as a noxious artefact: a limiting factor for quantitative imaging, since it confounds the extraction of morphometric parameters [175]. Consequently, in order to mitigate this, several methods were proposed in the literature. Among these, the first was proposed by Fu and collaborators [176] and consisted of acquiring two consecutive CARS images of the same field using perpendicular orientations of the incoming light polarisations. The two images were then fused in a computational post-processing step, as shown in Fig. 1.8. It should be borne in mind that this approach, albeit qualitatively effective, is based on a simple approximation of $X^{(3)}$, where only one term of the full tensor expression is considered [175].

A different approach was proposed by Bélanger and collaborators [175]. In this article the authors proposed using circularly polarised incoming light: in this way the polarisation-effect is almost completely suppressed without the need for post-processing the images. It should be pointed out, however, that the conservation of the polarisation state in a beam-scanning microscopy setup is not a trivial task and great care should be taken to this end. In Ref. [175] the authors used a combination of half-wave plates and quarter-wave plates, together with a careful calibration procedure to be repeated before each experiment, to compensate for polarisation distortions, which originate mainly from the dichroic mirror that allows collection of the signal in the epi-direction. In a subsequent publication [194] the same group demonstrated a calibration-free simplified setup based on an additional dichroic, identical to that already present, introducing complementary polarisation distortions that cancel out those introduced by the other element.

A very interesting observation was reported by Fu and collaborators. They demonstrated that damaged myelin, unlike healthy myelin, does not display the polarisation-dependent effect in CARS imaging [167], as shown in Fig. 1.10. In this article rat myelinated nervous fibres (both *in-vivo* in the sciatic nerve and *ex-vivo* in spinal cord) were exposed to lysophosphatidylcholine (lyso-PtdCho), a demyelinating chemical agent, and observed with PR CARS microscopy. This finding shows that the myelin molecular symmetry and spatial anisotropy are also destroyed during this demyelination process.

This observation suggested an intriguing hypothesis: the polarisation-dependent effect should not be considered a noxious artefact that has to be suppressed but possibly an efficient way to determine the local molecular order and extract information about the myelin health status.

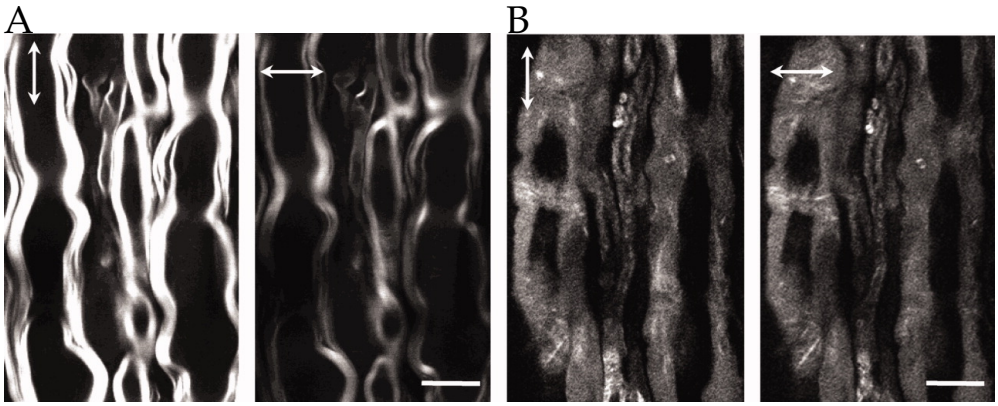

Figure 1.10: CARS images of normal myelin sheaths (*A*) and myelin sheaths exposed to lyso-PtdCho (*B*) acquired with vertical (vertical arrows) and horizontal (horizontal arrows) excitation polarisation. Scale bars: 10 μm. Figure reproduced with permission from: Y. Fu, H. Wang, T. B. Huff, R. Shi, and J.-X. Cheng, "Coherent anti-stokes Raman scattering imaging of myelin degradation reveals a calcium-dependent pathway in lyso-PtdCho-induced demyelination," *Journal of neuroscience research*, vol. 85, no. 13, pp. 2870-2881, 2007 [167]. Copyright John Wiley & Sons, Inc.

1.4.3 Polarisation-dependent effects as a way to study myelin

The CARS polarisation-dependent effect was first exploited by Bioud and collaborators to gather information about the molecular structure of myelin [195], although they made no attempt to link this information to any biological (i.e. not merely structural) properties, such as its healthiness. To this end, they used a powerful analytical framework developed by the same group in the context of FWM [195, 196] and CARS [195, 197, 198] microscopy. It consists of monitoring the signal intensity while rotating the incident-light polarisation plane and is able to accurately estimate the mean orientation of the molecular angular distribution and its second- and fourth-order of circular symmetry.

A very recent alternative approach to studying the zeroth-, second-, and fourth- order circular-symmetry properties of the sample (applied also to myelin) with CARS microscopy was proposed by Cleff and collaborators [199]. In this method the sample is illuminated alternately with left- and right-handed circularly-polarised light and then the left- and right-handed circular-polarisation components of the CARS signal are simultaneously detected. By recording the intensity of these two components while varying the polarisation state of the pump and Stokes beams, it is possible to determine in real-time the symmetry properties of the molecular distribution.

As I shall discuss more in detail in Sections 2.1.3 and 3.2.2, instead of focussing on the extraction of accurate information about the molecular symmetry structure,

I decided to exploit the same optical properties of the CARS process as an effective tool to gather information about the biological status of myelin. To this end, I proposed a CARS microscope based on a rotating linear-polarisation plane of the pump beam and a circularly polarised Stokes beam. By means of this approach it is possible to visualise the degree of orientation anisotropy of selected molecular bonds and to detect their average orientation direction within the Point Spread Function (PSF). Finally, in Section 3 I shall link this information to biological properties of the myelinated nerve fibres, such as the local orientation, the health status and the ageing effects.

2 MULTIMODAL SETUP

In this chapter I shall describe the CARS microscopy setup that I have developed and the experimental validation of the Rotating-Polarisation (RP) system. Then I shall detail the improvements that were implemented to enable fast, wide-area RP-CARS imaging, overcoming all the limitations that were identified in the initial approach. In particular, great care was taken to optimise the scanning speed and to minimise the polarisation distortions. Finally, I shall discuss a simplified frequency-resolved-optical-gating-like approach that I exploited to completely determine the pulse characteristics and to optimise the spectral resolution of the optical setup.

2.1 CARS-MICROSCOPE SETUP

2.1.1 Basic design

The first CARS microscope was a custom-built implementation of a broadband-CARS scheme. It is schematically shown in Fig. 2.1. 800 nm pump and probe degenerate beams were generated by a Titanium Sapphire (Ti-Sa) pulsed laser (Chameleon Vision 2, Coherent Inc., Santa Clara, California, U.S.A.) and spectrally narrowed by a pair of bandpass filters (labelled as 3-nm BP in Fig. 2.1) centred at 800 nm with a Full Width at Half Maximum (FWHM) of 3 nm. Approximately 750 fs pulses were then sent to a telescopic beam expander. A broadband Stokes radiation (covering a wavelength range from 450 nm to 1200 nm) was generated by a nonlinear crystal (SCG, photonic-crystal fiber SCG-800 Newport [200]) pumped by a fraction of the 800 nm pulses diverted from the pump beam by means of a beam splitter (BS). In order to excite the symmetrical stretch vibration of the CH_2 bonds, a spectral region ranging from 1000 nm to 1100 nm was selected from the broadband radiation by means of a combination of short-wave and long-wave pass filters (not shown in the Figure). Stokes radiation chirp was optimised by carefully tuning the power and chirp of the input pulse [201]. A 818 nm long-pass dichroic filter (D) recombined the pump and probe pulses with the Stokes ones. Temporal overlap between the pulses was achieved by adjusting a delay line (DL) on the Stokes-pulse path. The pulses were then routed to the high-numerical-aperture lens (Obj, Zeiss EC Plan-

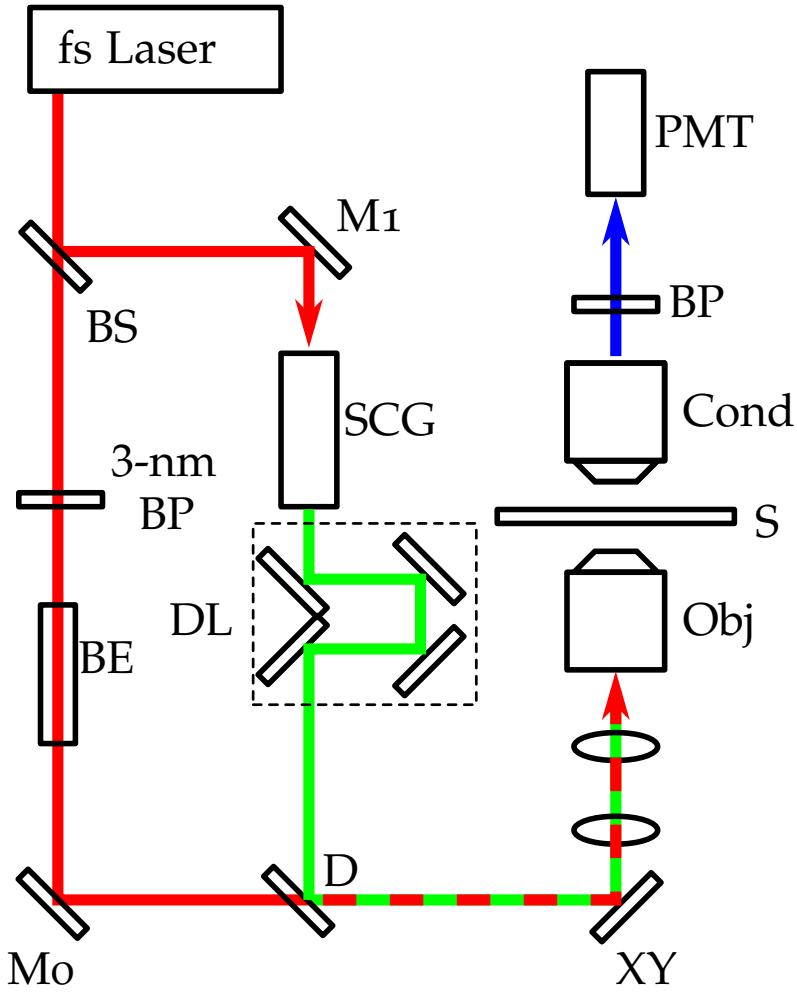

Figure 2.1: Schematic representation of the initial CARS microscope. The 800 nm pulses from the laser (fs Laser), shown as red lines, are split by a beam splitter (BS) and routed to the supercontinuum generator (SCG) and through two 3 nm bandpass filters (3-nm BP) centred at 800 nm. The broadband radiation (green lines) is delayed by a delay line (DL) and recombined with the 800 nm radiation by means of a dichroic mirror (D). The two are then routed to the high-numerical-aperture lens (Obj) through a pair of galvo-scanning mirrors, a scan lens and a tube lens. The CARS signal from the sample (S) is collected by a condenser lens (Cond), band-pass filtered (BP), and routed to a photomultiplier tube (PMT). Mo to M2 are silver-coated mirrors.

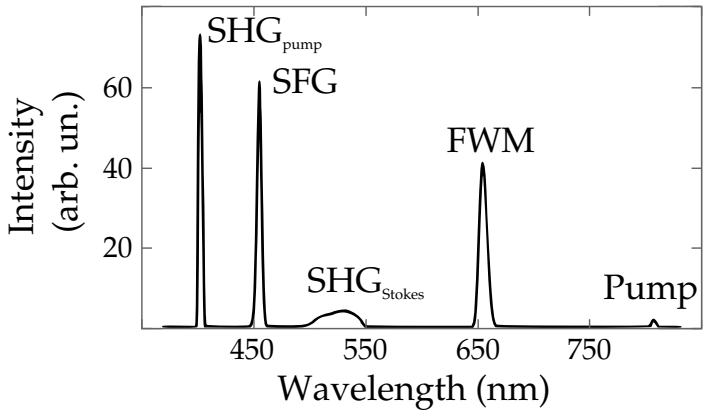

Figure 2.2: Plot of the spectrum collected from a $BaTiO_3$ nanoparticle illuminated with the pump-and-probe and Stokes beams overlapping in time.

NEOFLUAR, 40×, 1.3 NA) of an inverted microscope (Axio Observer Z1, Carl Zeiss MicroImaging GmbH, Göttingen, Germany) through a pair of galvo-scanning mirrors (XY, GVS002, Thorlabs, Newton, New Jersey, U.S.A.), a scan lens and a tube lens.

The CARS signal was collected from the sample (S) by a condenser lens (Cond, 0.55 NA), filtered with a band-pass filter (BP) centred at 650 nm with a FWHM of 10 nm (to select the Raman band of the CH_2 bonds here of interest at 2850 cm^{-1}), and routed to a red-sensitive photomultiplier tube (PMT, R3896, Hamamatsu, Hamamatsu City, Japan). The PMT output was finally sent to a data acquisition/generation board (USB-6366, National Instruments Corporation, Austin, Texas, U.S.A.) which also controlled the two galvo mirrors.

An exemplificative spectrum of the generated multi-modal signals is shown in Fig. 2.2. The pump-and-probe beam and the Stokes beam were temporally synchronised and focused on $BaTiO_3$ nanoparticles (described in Ref. [202]), which were chosen as a test sample because of their strong nonlinear optical properties [203, 204]. The SHG signals from the pump-and-probe beam and from the Stokes beam, the SFG signal from the two beams and the FWM signal are all easily identifiable on the spectrum.

2.1.2 Rotating-Polarisation system

To take advantage of the polarisation selection rules of the CARS process [175], I have further improved the setup described in Section 2.1.1 in order to make it ca-

pable of detecting the local microscopic orientation of the chemical bonds under investigation [205], and I named this new technique: Rotating-Polarisation (RP)-CARS microscopy. As shown in Fig. 2.3, a rotating half-wave retarder (R-$\lambda/2$) was placed on the pump-and-probe beam path before the telescopic beam expander while an achromatic quarter-wavelength retarder ($\lambda/4$) was employed to transform the linearly polarised Stokes pulses into circularly polarised radiation. A second quarter-wavelength retarder was introduced in the pump and probe path in order to compensate for polarisation distortions caused by the 818 nm long-pass dichroic filter (D) [175].

With respect to the approach described in Ref. [176], where all the polarisations of the pump, Stokes, and probe beam were chosen to be linear and parallel to each other at the sample, my implementation consists of a circularly-polarised Stokes beam and a (rotating) linearly-polarised pump and probe beam. This choice avoids a few drawbacks of the all-linear-polarisation approach:

- Rotating the Stokes and pump-and-probe beams with the same half-wave retarder leads to small ellipticity of at least one of the beams due to their different wavelengths, even with an achromatic retarder.
- Rotating the Stokes and pump-and-probe beams with two different half-wave retarders would be technically challenging because the retarders would need to be rotated exactly at the same frequency and phase.

On the contrary, in my approach the rotating half-wave retarder can be matched to the frequency of the narrowband pump-and-probe beam and the Stokes-beam-polarisation circularity can be obtained and tested at the sample by carefully adjusting a quarter-wavelength retarder.

The output of the PMT was fed into a lock-in amplifier, whose reference frequency was generated by a Hall-effect Sensor (HS) mounted in proximity to the electric brushless motor that drives the R-$\lambda/2$. The HS output two TTL pulses for each complete rotation of the retarder. Therefore, this signal has the same frequency of the rotating pump-and-probe polarisation plane and a fixed phase delay with respect to it. For conventional CARS imaging, the PMT output was also sent to the data acquisition/generation board that controlled the two galvo mirrors.

2.1.3 Theory

Following Refs. [176, 206, 207], the third-order susceptibility of the linear acyl chains of the phospholipidic membranes of the myelin layers can be described by a fourth-rank tensor containing just four independent coefficients: c_{11}, c_{16}, c_{18}, c_{33}, as shown in the following:

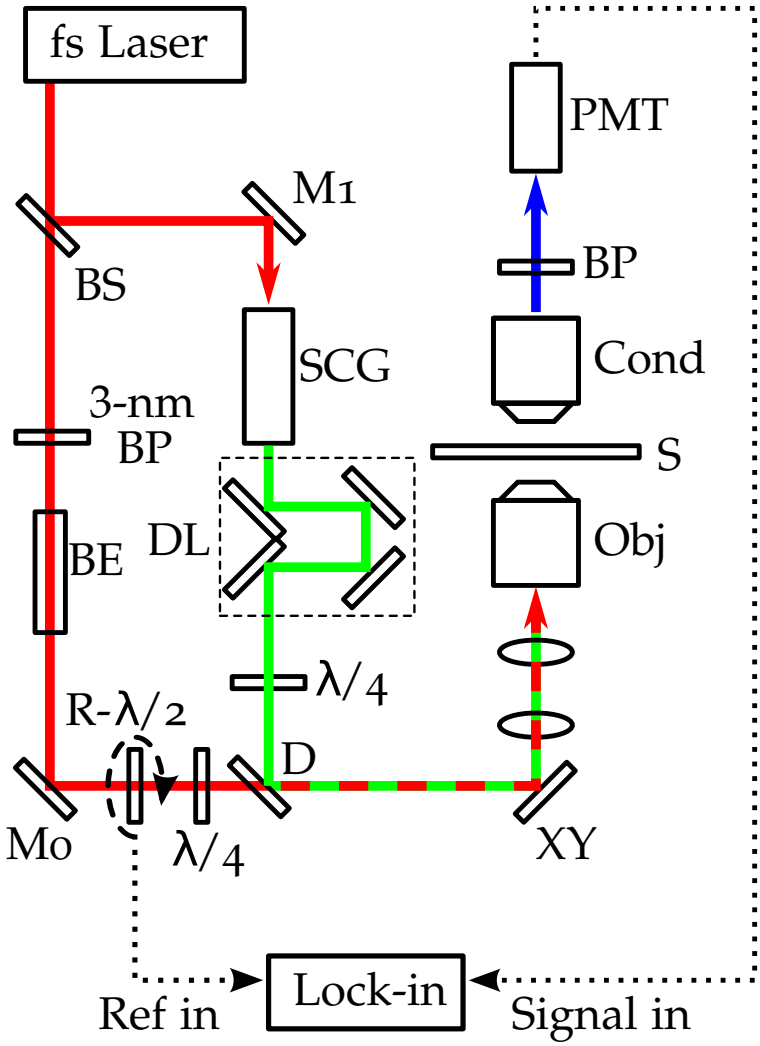

Figure 2.3: Schematic representation of the first RP-CARS setup. With respect to the original setup shown in Fig. 2.1, a rotating $\lambda/2$ retarder (R-$\lambda/2$) was placed on the pump-and-probe beam path (shown as red lines). The linearly-polarised broadband radiation (green lines) was transformed into circularly polarised light by a $\lambda/4$ retarder ($\lambda/4$). A second $\lambda/4$ retarder in the pump-and-probe path compensated for polarisation distortions caused by the dichroic mirror "D". The output of the PMT was measured by phase-sensitive techniques by means of a lock-in amplifier. The reference phase and frequency for the lock-in amplifier was generated by an HS in close proximity to the rotor of the brushless motor that rotates R-$\lambda/2$. For all other symbols in the scheme, please refer to the legend in Fig. 2.1.

$$\begin{pmatrix} \begin{pmatrix} c_{11} & 0 & 0 \\ 0 & c_{18} & 0 \\ 0 & 0 & c_{16} \end{pmatrix} & \begin{pmatrix} 0 & c_{18} & 0 \\ c_{18} & 0 & 0 \\ 0 & 0 & 0 \end{pmatrix} & \begin{pmatrix} 0 & 0 & c_{16} \\ 0 & 0 & 0 \\ c_{16} & 0 & 0 \end{pmatrix} \\ \begin{pmatrix} 0 & c_{18} & 0 \\ c_{18} & 0 & 0 \\ 0 & 0 & 0 \end{pmatrix} & \begin{pmatrix} c_{18} & 0 & 0 \\ 0 & c_{11} & 0 \\ 0 & 0 & c_{16} \end{pmatrix} & \begin{pmatrix} 0 & 0 & 0 \\ 0 & 0 & c_{16} \\ 0 & c_{16} & 0 \end{pmatrix} \\ \begin{pmatrix} 0 & 0 & c_{16} \\ 0 & 0 & 0 \\ c_{16} & 0 & 0 \end{pmatrix} & \begin{pmatrix} 0 & 0 & 0 \\ 0 & 0 & c_{16} \\ 0 & c_{16} & 0 \end{pmatrix} & \begin{pmatrix} c_{16} & 0 & 0 \\ 0 & c_{16} & 0 \\ 0 & 0 & c_{33} \end{pmatrix} \end{pmatrix} \tag{2.1}$$
$$i, j, k, l \in x, y, z$$

In Cartesian coordinates xyz, where the z-axis is oriented along the optical axis, the electric fields of a linearly polarised pump-and-probe beam ($\boldsymbol{E_p}$), with a polarisation plane rotating at an angular velocity ω, and a circularly-polarised Stokes beam ($\boldsymbol{E_S}$) can be modelled as plane waves and described as in the following:

$$\begin{aligned} \boldsymbol{E_p} &= A_p[e^{it(\omega_p+\omega)}(\hat{\boldsymbol{x}} - i\hat{\boldsymbol{y}}) + e^{it(\omega_p-\omega)}(\hat{\boldsymbol{x}} + i\hat{\boldsymbol{y}})] + c.c. \\ \boldsymbol{E_S} &= A_S e^{-i\omega_S t}(\hat{\boldsymbol{x}} \pm i\hat{\boldsymbol{y}}) + c.c. \end{aligned} \tag{2.2}$$

where ω_p and ω_S are the frequencies of the two beams, and $\hat{\boldsymbol{x}}$ and $\hat{\boldsymbol{y}}$ are the unit vectors along the respective axes.

In the described geometry, the time-dependent CARS-signal intensity is proportional to:

$$I_{CARS}(t) \propto I_p^2 I_S \left[A_{dc} + A_{2\omega} e^{(2i\omega t + i\phi)} + A_{4\omega} e^{(4i\omega t + i\phi)}\right], \tag{2.3}$$

where I_p and I_S are the intensities of the pump-and-probe beams and of the Stokes beam respectively, and:

$$\begin{aligned} A_{dc} &= 3c_{11}^2 + 2c_{11}c_{16} + 14c_{16}^2 + 2c_{33}c_{16} + 3c_{33}^2 \\ A_{2\omega} &= 4(c_{11}^2 - c_{33}^2) \\ A_{4\omega} &= c_{11}^2 - 2c_{11}c_{16} - 6c_{16}^2 - 2c_{33}c_{16} + c_{33}^2. \end{aligned} \tag{2.4}$$

Here ϕ is the angle at $t = 0$ between the polarisation plane and the acyl chains. By employing phase-sensitive techniques the three terms A_{dc}, $A_{2\omega}$, $A_{4\omega}$ and the phase ϕ that represents the local orientation of the dipoles can be readily measured.

In order to get accurate results it is of paramount importance to compensate for polarisation distortions, due to different retardation of the p and s components of the fields introduced by the dichroic mirror D. To this end, the FWM signal coming from the glass cover slip can be exploited to calibrate the system, since it contains exclusively an isotropic contribution due to the amorphous nature of the glass. It can be described by the following third-order susceptibility [112]:

$$X_{ijkl} \propto \delta_{ij}\delta_{kl} + \delta_{ik}\delta_{jl} + \delta_{il}\delta_{jk}. \tag{2.5}$$

In the ideal case of a circularly polarised Stokes beam and rotating perfectly-linear pump-and-probe beams, it is easy to see that $I_{CARS}(t)$ is a constant. On the contrary, if the Stokes beam is elliptical rather than perfectly circular, the CARS signal also contains a second-harmonic component:

$$I_{CARS}(t) = I_p^2 I_S \left[B_{dc} + B_{2\omega} e^{(2i\omega t + i\phi)} \right], \tag{2.6}$$

where B_{dc} and $B_{2\omega}$ depend on the amount of distortion from a perfectly circularly polarised beam and ϕ depends on the orientation of the ellipse axis.

The other possible deviation from the ideal case stems from polarisation distortions of the pump-and-probe beam caused by D. In this case $I_{CARS}(t)$ contains both second-harmonic and fourth-harmonic contributions in addition to a constant term.

These considerations imply that it is possible to compensate for polarisation-distortion effects by minimising — introducing opposite distortions using the two additional quarter-wavelength retarders — the second- and fourth-harmonic component of the FWM signal from a glass slide. Ratios $A_{2\omega}/A_{dc}$ and $A_{4\omega}/A_{dc}$ smaller than 0.5% could routinely be achieved.

2.1.4 Experimental validation of the RP-system

In order to validate the described approach, the RP-CARS setup was used to visualise a sample of mouse-brain white matter. The mouse brain is a complex tissue, where grey matter (cell somata and non-myelinated axons) is interposed with white matter (myelinated and non-myelinated axons). White matter gives a strong CARS signal at 2850 cm^{-1} from the highly ordered CH_2 bonds due to the lipid-rich myelin [141, 176, 208].

The incident laser light is linearly polarised in traditional CARS microscopes. This usually leads to the artefact described in Section 1 and similar to the one depicted in Fig. 2.4 that shows an individual myelinated axon placed perpendicularly to the imaging plane: chemical bonds aligned with the polarisation plane of the incident light generate a stronger CARS signal with respect to those aligned perpendicularly.

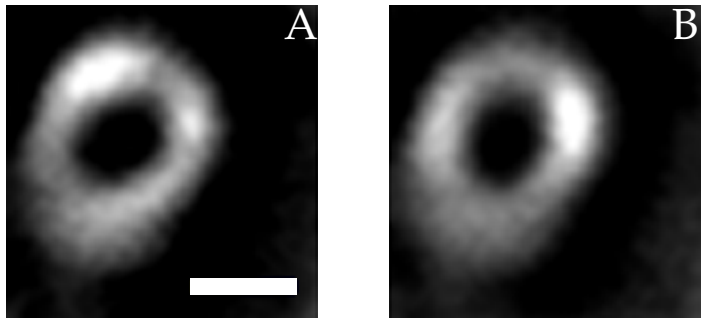

Figure 2.4: Polarisation-dependent artefacts in a CARS image of a single nerve axon in transverse section (CH and CH_2 bonds). (*A*) The polarisation-dependent artefact is evident when linearly-polarised light is used. In this case the CH and CH_2 chemical bonds aligned with the polarisation plane of the incident light (vertical in the image) generate a stronger CARS signal. (*B*): Same as (*A*) but using a perpendicular polarisation plane of the incident light (horizontal in the image). The pump and probe beam and the Stokes beam power was respectively 30 mW and 12 mW. Scale bar: 0.5 µm.

Such artefacts can be mitigated by post-processing two images acquired with orthogonal polarisations [176] or by using circularly polarised light [175].

RP-CARS exploits, rather than circumvents, polarisation selection rules in order to gather information on the local orientation anisotropy of chemical bonds. The radius signal originated by the lock-in amplifier ($A_{2\omega}$, when the second harmonic with respect to the reference frequency is selected) is a measure of the local – within the PSF volume – in-plane anisotropy of the molecular-bond orientation. The phase of the signal (ϕ), measured by the lock-in, corresponds to the average orientation of the target bonds. In order to visualise both signals at the same time, I used the Hue, Saturation, Value (HSV) colour space, where the $A_{2\omega}$ signal is mapped onto the value channel and the ϕ signal onto the hue. Saturation is kept at the maximum value. This visualisation method is described in Fig. 2.5, showing the same single individual axon displayed in Fig. 2.4. Also, by using RP-CARS it is possible to generate images free from polarisation artefacts by exploiting the A_{dc} signal, as shown in Fig. 2.5A. The $A_{2\omega}$ signal and the ϕ signal from the lock-in are shown in Fig. 2.5B and Fig. 2.5C respectively. The final image obtained according to the approach described above is displayed in Fig. 2.5D. ϕ acquires random values when the SNR is very small, but this does not affect the final fusion image because the brightness is small too. The myelin sheath changes colour smoothly, covering all the possible orientations, owing to the directionality of the CH_2 bonds in its phospholipid bilayers: the CH_2 bonds of the phospholipid acyl chains always lie in planes parallel to the surface of the membrane, and therefore gradually assume all possible orientations in the circumference of the sheath.

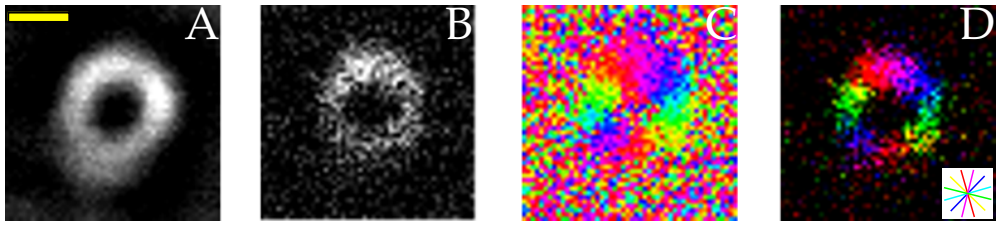

Figure 2.5: RP-CARS imaging of the same single nerve axon as in Fig. 2.4 (CH_2 bonds, transverse section). (*A*): Image constructed using A_{dc}. Compared to the images in Fig. 2.4 it is free from the polarisation artefacts. (*B*): Image constructed using $A_{2\omega}$ (bright pixels indicate that the signal value depends strongly on the light-polarisation orientation). (*C*): Image of the ϕ signal collected from the same region (the colours indicate different light-polarisation orientations). (*D*): RP-image created in the HSV colour space, mapping the ϕ values onto the "hue" channel and mapping $A_{2\omega}$ onto the "value" channel, while keeping the "saturation" channel values at maximum. The myelin sheaths change colour smoothly, covering all the possible orientations. Inset: colour-coding scheme of the hue-mapped orientation. The power levels were the same of Fig. 2.4. The scale bar length is 0.5 μm.

As noted above, lock-in techniques give access to A_{dc}, $A_{2\omega}$ and $A_{4\omega}$ and, in turn, to the coefficients of the third-order susceptibility (up to a proportionality factor). Focusing this microscope on a myelinated fibre wall yielded $A_{dc} = 150$ mV, $A_{2\omega} = 38.5$ mV, and $A_{4\omega} = 2.5$ mV. Inverting Eq. 2.4 the following values for the coefficients can be calculated: $c_{11} = 1$, $c_{16} = 0.28$, $c_{33} = 0.75$, in good agreement with values previously reported for fixed tissues [175].

Biological sample preparation

Adult wild-type (WT) mice were perfused with 4% paraformaldehyde. The fixed brains were extracted from the skull and cut with a vibratome in coronal slices of 100 μm to 150 μm thickness. The slices were then mounted on standard microscopy slides in the presence of Phosphate Buffer Saline (PBS) solution and finally sealed with a glass cover slip and nail polish.

2.2 IMPROVEMENT OF THE RP-CARS SETUP

2.2.1 Generation of the incoming beams

During the first years of my Ph.D. course, several limitations of the original RP-CARS setup were identified and consequently a second setup was developed in order to overcome them. For this purpose, particular attention was given to the following technical aspects: the generation of the incoming beams (described in this

Section), the optimisation of the acquisition process (described in Section 2.2.2), the movements of the scanning mirrors, the minimisation of the polarisation distortions (described in Section 2.2.3) and the spectral focusing (described in Section 2.3).

A major limiting factor for the CARS signal levels (I_{CARS}) was identified in the generation method of the Stokes beam, the supercontinuum generator (SCG). Since I_{CARS} is proportional to the intensity of the Stokes beam (I_S) and to the square of the intensity of the pump-and-probe beam (I_p^2):

$$I_{CARS} \propto I_S I_p^2, \tag{2.7}$$

it follows that, for a fixed total incoming light intensity:

$$I_T = I_S + I_p, \tag{2.8}$$

limited by the photodamage level for biological tissues (here I am assuming for the sake of simplicity that the photodamage does not depend on the wavelength of the radiation), the maximum of I_{CARS} is achievable when:

$$I_p = 2I_S. \tag{2.9}$$

Nevertheless, it was not possible to meet this condition because the light generated by the SCG ranges from 450 nm to 1200 nm [200] and therefore the fraction that excites the Raman band of interest at 2850 cm^{-1} is very small (being limited in the range between 1000 nm and 1100 nm). In order to overcome this limitation, the SCG was replaced by an Optical Parametric Oscillator (OPO). In this way it is possible to convert a greater amount of power from the pump-and-probe beam into a relatively narrowband Stokes beam, leading to greater intensity of the generated CARS signal. The difference in the bandwidth of the Stokes beam can be visualised by comparing the SHG signal generated by barium titanate nanoparticles when exploiting the SCG (Fig. 2.2) or the OPO (Fig. 5.3D).

The improved RP-CARS setup is schematically shown in Fig. 2.6 (left). The 810 nm pump-and-probe beam is generated by the Ti-Sa pulsed laser ("fs Laser"). Part of this beam is used to pump the OPO ("OPO"; Oria IR, Radiantis, Barcelona, Spain) and the 1060 nm signal beam generated by the OPO is used as the Stokes beam (the idler beam of the OPO is dumped). The Ti-Sa laser is optically isolated from the OPO by a Faraday isolator ("Is"), in order to prevent back-reflections from the OPO entering the laser cavity.

Each beam passes through an SF6 optical-glass block ("G" and "G'") and telescopic beam expanders ("BE" and "BE'"). The thicknesses of the optical glass blocks were carefully chosen in order to achieve spectral focusing [209–211] in the sample

optical plane by optimal tuning of the pulse Group Delay Dispersions (GDDs) and are computed in order to yield GDDs of approximately 30000 fs^2 at the wavelengths of interest here for each of the two beams (as is described in great detail in Section 2.3). If the chirps are chosen appropriately, the instantaneous frequency difference between the pump and Stokes beam is constant as a function of time. This approach was shown to yield improved spectral selectivity, comparable with that obtainable with transform-limited pulses with the same duration of the chirped pulses, and increased ratio between the resonant and non-resonant signals.

Before being recombined by means of a 900 nm long-pass dichroic mirror ("D") the Stokes beam is delayed by a delay line ("DL") in order to temporally overlap to the pump-and-probe beam and each beam passes through a pair of waveplates. Specifically, the Stokes beam is circularly polarised by means of a pair of $\lambda/4$ retarders ("$\lambda/4$") that also compensate for polarisation distortions induced by the downstream Dichroic Mirrors (DMs); while a mechanically rotating $\lambda/2$ retarder ("R-$\lambda/2$") is used to continuously rotate the polarisation plane of the linearly polarised pump-and-probe beam and a second fixed $\lambda/4$ retarder ("$\lambda/4$") on the pump-and-probe beam line is used for the polarisation-distortion compensation.

The combined pump-and-probe and Stokes beams are then routed to the high-numerical-aperture (NA) lens ("Obj", Objective C-Achroplan W, 32×, 0.85 NA, Carl Zeiss MicroImaging GmbH, Göttingen, Germany) of the inverted microscope through a pair of galvo-scanning mirrors ("XY"), a scan lens, a DM, a compensation lens, and a tube lens. This lens arrangement is further described in the Section 2.2.3. The CARS signal originating from the sample ("S") is collected both in the trans-direction by a condenser lens ("Cond", 0.55 NA) and in the epi-direction and then detected by means of red-sensitive photomultiplier tubes ("PMT"). In the trans-direction the CARS signal is edge-filtered to remove the excitation photons and band-pass filtered (BP, filter centred at 650 nm and with a FWHM of 50 nm) to select the Raman band of the CH_2 bonds (2850 cm^{-1}). In the epi-direction the CARS signal is routed to the detector by means of a dichroic mirror ("D") situated between the compensation lens and the scan lens and then filtered in the same way as the trans-direction signal ("BP") and focalised by an additional lens. Silver-coated mirrors are labelled with "M".

The output of the PMTs and the signal generated by the HS of the brushless motor that rotates the $\lambda/2$ waveplate are acquired by the digital acquisition board ("Software Lock-in") and elaborated by a custom-made software application (written in LabVIEW programming language, Lab-VIEW 2010 SP1, National Instruments Corporation, Austin, Texas, U.S.A.) running on a PC to compute – in real time and for each pixel – A_{dc}, $A_{2\omega}$, and ϕ of the raw CARS signal. This acquisition method is described in greater detail in Section 2.2.2.

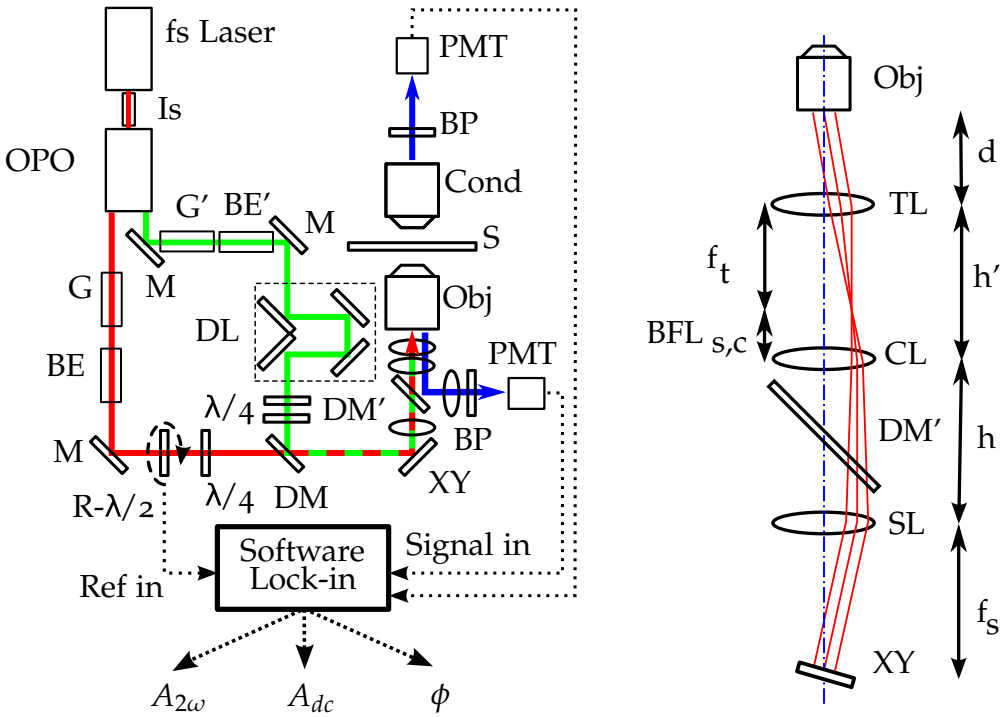

Figure 2.6: (*Left*): Second RP-CARS setup. Femtosecond laser (fs Laser), Faraday optical isolator (Is), optical parametric oscillator (OPO), SF6 optical glasses (G and G'), beam expander (BE), dichroic mirrors (DM, DM'), rotating half-wave plate (R-$\lambda/2$), quarter-wave plate ($\lambda/4$), delay line (DL), galvanometric mirrors (XY), sample (S), microscope objective (Obj), condenser (Cond), band-pass filter (BP), photomultipliers (PMT). The custom-made software (Software Lock-in) computes A_{dc}, $A_{2\omega}$ and ϕ values from the detected signals. Thick red, green, and blue lines show the paths of the pump, Stokes and signal beams respectively. (*Right*): Detail of the laser-scanning optics, showing the scan lens (SL), the compensation lens (CL), the tube lens (TL, inside the microscopy body), the objective (Obj), and the galvanometric mirrors (XY). $BFL_{s,c}$: back focal length of the virtual lens formed by the scan lens and the compensation lens; f_t, f_s: focal length of the tube lens and of the scan lens, respectively. The blue dash-dotted line indicates the optical axis. The red lines indicate the beam path.

2.2.2 Fast-scanning technique

In order to speed up the acquisition process, a software approach was elaborated that mimics a hardware lock-in amplifier [212] and the algorithm was implemented with the LabVIEW programming language. Images are acquired by raster-scanning the laser spot onto the sample using a pair of galvanometric mirrors and digitising under computer control the output of the PMT and the output of the HS by means of the digital acquisition board. In the following I shall refer to lines of pixels along the fast-scan direction as "columns" and those perpendicular to it as "rows". Each column of the image is scanned multiple times (N) while the R-$\lambda/2$ is rotating and the corresponding signal processed after moving the laser spot to the next column.

For each pixel, the signals from the PMT and from the HS are acquired with an integration time of T_p. Care has to be taken in order to choose the time needed to scan the column, $T_L = T_p n_y$ (where n_y is the number of pixels per column) to be much shorter than the rotation period so that each pixel of the column is sampled many times for each rotation period in order to satisfy the Nyquist sampling theorem but, at the same time, long enough to account for the limited dynamics of the galvo mirror (400 Hz resonant frequency). Additionally, the total acquisition time of the column, $2NT_L$ (here the factor of two accounts for the fact that the columns are always scanned in the same direction and the galvo mirror has to go back to the top of the column before starting a new scan), has to be long enough to encompass a few rotations of the R-$\lambda/2$.

This acquisition procedure yields two multidimensional arrays, $S(x, y, i)$ and $H(x, y, i)$, containing the digitised values of the outputs of the PMT and of the HS respectively. Here x and y label the columns and the rows of the image and i represents the multiple acquisitions of each pixel, with $0 < i \leq N$. When the acquisition of the column is complete, the software performs a discrete Fourier transform of $H(x, y, i)$ for each column to extract a reference angular frequency $\widetilde{\omega}(x) = 2\omega_R$ that corresponds to the angular frequency of the incident-light polarisation plane (typically 20 to 30 Hz in my experiments), and a reference phase $\widetilde{\phi}(x)$. The dependence of $\widetilde{\omega}$ and $\widetilde{\phi}$ on x is due to the fact that the Fourier transforms are computed on a column-by-column basis rather than on the entire dataset to account for variations in the rotation speed of the R-$\lambda/2$ during the acquisition process. This procedure is justified by the observation that during the acquisition of each column the rotation speed does not change significantly.

Finally, the program finds the two orthogonal Fourier components of the PMT signal at $2\omega_R$ and the average value:

$$A^{\sin}_{2\omega}(x, y) = \frac{2}{N} \sum_{i=1}^{N} S(x, y, i) w(i) \sin\left(2i\widetilde{\omega}(x) T_L + \widetilde{\phi}(x)\right) \tag{2.10}$$

$$A_{2\omega}^{\cos}(x,y) = \frac{2}{N}\sum_{i=1}^{N} S(x,y,i)w(i)\cos\left(2i\widetilde{\omega}(x)T_L + \widetilde{\phi}(x)\right) \tag{2.11}$$

$$A_{dc}(x,y) = \frac{1}{N}\sum_{i=1}^{N} S(x,y,i), \tag{2.12}$$

where $w(i)$ is a Kaiser-Bessel window function, and calculates the magnitude $A_{2\omega}$ and the phase ϕ:

$$A_{2\omega}(x,y) = \sqrt{A_{2\omega}^{\sin}(x,y)^2 + A_{2\omega}^{\cos}(x,y)^2} \tag{2.13}$$

$$\phi(x,y) = \arctan_2\left(A_{2\omega}^{\sin}(x,y), A_{2\omega}^{\cos}(x,y)\right) - \widetilde{\phi}(x), \tag{2.14}$$

where the function $\arctan_2(a,b)$ is the two-argument arc-tangent function that returns the angle between the positive x-axis of a plane and the point given by the coordinates (a,b). To minimise the total acquisition time, this procedure is carried out during the acquisition of the next column of the image. $A_{dc}(x,y)$ depends on the density of chemical bonds of interest within the PSF volume. An image based on this function is therefore equivalent to an artefact-free CARS image acquired with the conventional techniques. The magnitude signal $A_{2\omega}(x,y)$ is a measure of how much the raw signal from the (x,y) pixel varies during a rotation of the polariser and therefore it represents the degree of in-plane anisotropy of the molecular-bond orientation within the PSF volume. The phase value $\phi(x,y)$ is a measure of the orientation of this anisotropy. The functions $A_{dc}(x,y)$, $A_{2\omega}(x,y)$ and $\phi(x,y)$ correspond to those defined in 2.1.4.

Other authors that studied the anisotropy in the lipid membranes with TPF microscopy [180] or in textile fibres with CARS [193] exploited a different approach based on the collection of several images, each with a slightly different rotation of the polarisation plane and subsequent pixel-by-pixel analysis. The acquisition speed of this method is comparable to that of the technique presented here, but with my implementation the visual feedback to the user is much faster as the image is refreshed column per column and also almost all the processing (except for the last column of the image) is performed in parallel with the acquisition.

2.2.3 Large-field polarisation-resolved laser scanning microscopy

Galvanometric scanning

The developed optical setup is specifically optimised to obtain high acquisition rates and to retain at the same time a sufficient SNR for PR CARS imaging. The approach described in Section 2.2.2 requires moving the galvanometric mirrors at high speed

to allow the collection of the signal from an entire line multiple times within each rotation of the polarisation plane, potentially causing imaging artefacts at the two ends of each scanning line – images "look smeared" – where the fast-scanning mirror has to decelerate and then accelerate in the new scanning direction. In order to reduce these artefacts, the acquisition was performed only in one motion direction (from $-x_0$ to x_0), where the mirror position was set to change linearly with time (from $-t_0$ to t_0), at constant velocity (v_0), and used a fourth-degree polynomial to describe the mirror set-position $x(t)$ versus time during the return phase:

$$x(t) = a \times t^4 + b \times t^3 + c \times t^2 + d \times t + e \tag{2.15}$$

For the set-position function to be as smooth as possible (thereby minimising the set/real position mismatch), the following conditions were imposed: the function continuity at the extremities: $x(t_0) = x_0$; $x(-t_0) = -x_0$, the velocity continuity at the end of the return phase: $\dot{x}(t_0) = v_0 = \frac{x_0}{t_0}$, zero acceleration at the end of the return phase: $\ddot{x}(t_0) = 0$, and zero velocity at the central temporal point of the return phase: $\dot{x}(0) = 0$. With those constraints, and setting $x(t = 0) = 0$, $x(t)$ becomes:

$$x(t) = -\frac{x_0}{4 \times t_0^4} \times t^4 + \frac{x_0}{t_0^3} \times t^3 - \frac{3 \times x_0}{2 \times t_0^2} \times t^2 + \frac{7 \times x_0}{4}, \tag{2.16}$$

where $2 \times x_0$ is the total deflection and $2 \times t_0$ the time needed for the mirror to cover it. This approach successfully suppresses the smearing artefacts while keeping overall a high scan speed, although changing the acquisition speed still produces a small but measurable spatial shift of the images, caused by the lag in the mirror real position versus the set one. In order to visualise the effects of this approach, the real position of the galvanometric mirror was acquired using the electric diagnostic output of the mirror driver and in Fig. 2.7 it is compared with the set one. Fig. 2.7C shows the mismatch between the set and the real position during the acquisition phase of the scan. If the polynomial function described above is used, then this mismatch is kept constant during the acquisition (causing the small spatial shift) and its magnitude depends on the scanning speed. On the contrary, if a simple, linear function is used, then a large variation in the mismatch value is present at the beginning of the acquisition phase, causing the smearing artefact in the image.

Polarisation distortions in large-field scanning

As noted above, the DMs are the major cause of polarisation distortions and this is particularly true when the light incidence angle on those mirrors varies during the scan. The DM used to collect the signal in the epi-direction must be positioned as

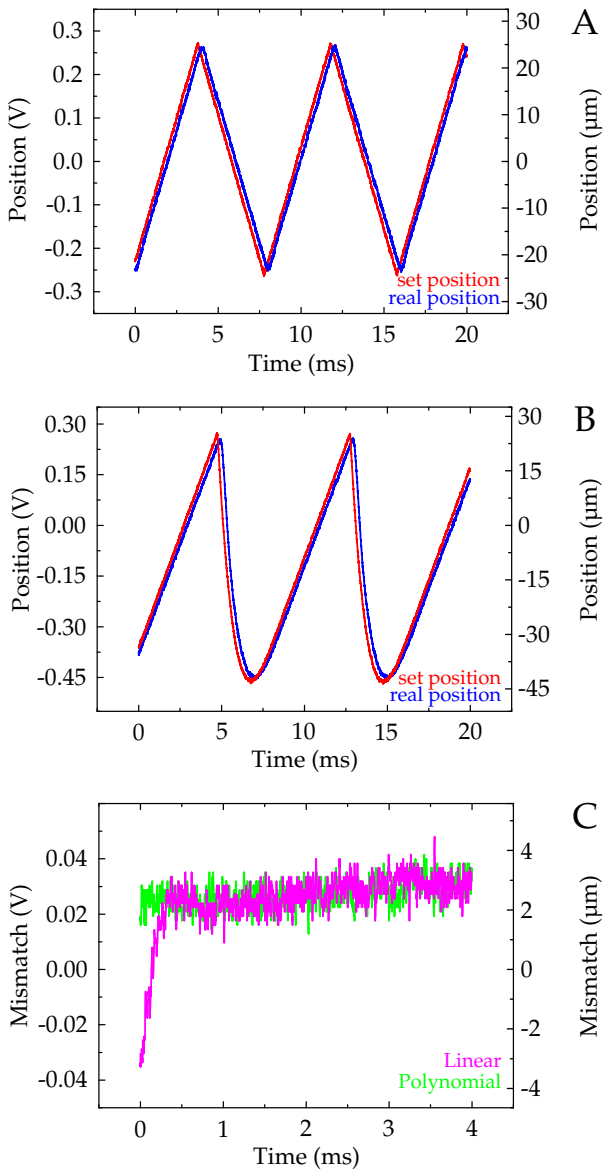

Figure 2.7: Set and real position of the fast-scanning galvanometric mirror when using a simple, linear set-position function (*A*) or the polynomial set-position function (*B*) described in Section 2.2.3. The mismatch between the set and the real position during the acquisition phase of the scansion in the two cases is shown in (*C*).

close as possible to the objective, in order to maximise collection efficiency. Conveniently, the DM may be placed between the tube lens and the scan lens. An additional lens, mounted between the DM and the PMT, images the objective pupil onto the PMT surface. If the objective rear aperture is in the focal plane of the tube lens, then it is possible to implement a 4-f configuration by placing the scan lens so that its focal plane and that of the tube lens coincide. In this case the incoming-beam axis is always parallel with respect to the optical axis in the region between the scan lens and the tube lens, irrespective of the position of the galvanometric mirrors. Therefore, its angle of incidence with respect to the DM is always constant.

However, if the objective rear aperture is not in the focal plane of the tube lens, as in the case of many commercial microscopes, including the one used for my thesis, then it is not possible to achieve this ideal situation. However, I show that this problem can be overcome by placing a compensation lens between the DM and the tube lens, as displayed in Fig. 2.6 (right), and positioning the scan lens at a focal-length distance from the galvanometric mirrors. In this way the incoming-beam axis always remains parallel with respect to the optical axis in the region between the two lenses and therefore through the DM, independently from the galvanometric-mirror positions.

In order for the beam to be collimated into the objective rear aperture, the distance between the compensation lens and the tube lens (h') and the distance (h) between the scan lens and the compensation lens are adjusted so that the focal plane of the virtual lens constituted by the latter two coincides with the focal plane of the tube lens.

$$f_t + BFL_{s,c} = h', \tag{2.17}$$

where: $BFL_{s,c} \equiv (f_s - h) \times f_c/(f_s + f_c - h)$ is the back focal length of this virtual lens, and f_s, f_c, f_t are the focal lengths of the scan, compensation, and tube lenses respectively. Finally, in order to have constant illumination of the pupil throughout the scanning range, the set of the three lenses has to image the scan mirrors onto the pupil of the objective, or – equivalently – that the latter lies on the focal plane of the virtual lens composed by the compensation and tube lenses:

$$BFL_{c,t} \equiv (f_c - h') \times f_t/(f_c + f_t - h') = d, \tag{2.18}$$

where d is the distance between the objective rear aperture and the tube lens.

Equations 2.17 and 2.18 show that, for a given scan lens and tube lens, several combinations of f_c, h' and h can be used, conveniently allowing the selection of the compensating lens from available stock lenses and consequently the determination of h and h'.

In my microscope the scan lens was constituted by a pair of achromatic lenses (AC254-200-B and AC254-150-B, with focal lengths of 20 cm and 15 cm respectively, Thorlabs, Newton, New Jersey, U.S.A.), selected by means of simulations with Oslo 66 to yield minimum aberrations. The lenses were placed with their most convex optical surfaces facing each other, with the 20 cm lens mounted closer to the mirrors. The effective focal length of this combination was calculated to be approximately 9.0 cm. In this microscope I had: $f_t = 16.5$ cm and $d = 12$ cm. Selecting a compensation lens with a focal length of 60 cm yielded: $h = 9.5$ cm and $h' = 16$ cm. Final adjustments to the lens positions in the real setup which correct to constant illumination of the pupil during the scan were performed by maximising the field of view while keeping the CARS imaging plane coincident with the naked-eye-observation plane.

To validate this approach, the residual polarisation distortions in my setup were quantified by acquiring a non-resonant large-scale RP-CARS image of a glass slide as explained in Section 2.1.3. I used the ratio $A_{2\omega}/A_{dc}$ as a measure of the residual polarisation distortions. The phase indicates the spatial orientations of the induced distortions. As displayed in Fig. 2.8, the magnitude of the distortions increases with the distance from the centre of the image. Nevertheless, its maximum – approx. 6%, observed at the periphery of the large-scale image – is negligible (~ 5 times smaller) with respect to the anisotropy values usually detected from the biological samples (e.g. myelin sheaths of mouse nerves) with similar approaches (as described in Section 3).

Without the compensation lens, it is still possible to remove the polarisation distortions in the centre of the image field but they increase up to 12.8% in the image periphery, as displayed in Figs. 2.8B and 2.8C.

While the use of a high-NA objective leads to the generation of polarisation components along the optical axis, this has a negligible effect on the orientation detection, because it does not induce a deformation of the polarisation response [213]. Moreover, for objectives with NA 0.85, such as the one used in this setup, the polarisation component along the optical axis is less than 10% of the transverse component [214] and it is therefore possible to neglect its effects. In addition, I have further addressed this issue by means of numerical simulations whose results are discussed in Section 4.3.

It should be noted that PR laser-scanning microscopy can also be performed by scanning the sample and keeping the incoming rays fixed in space. If, on the one hand, this configuration is very effective in minimising the polarisation distortions all over the field of view, on the other the acquisition is typically very slow because it requires moving the microscope stage. On the contrary, my approach allows for fast laser-scanning PR imaging over large spatial scales, opening up new possibilities for the applications of this microscopy.

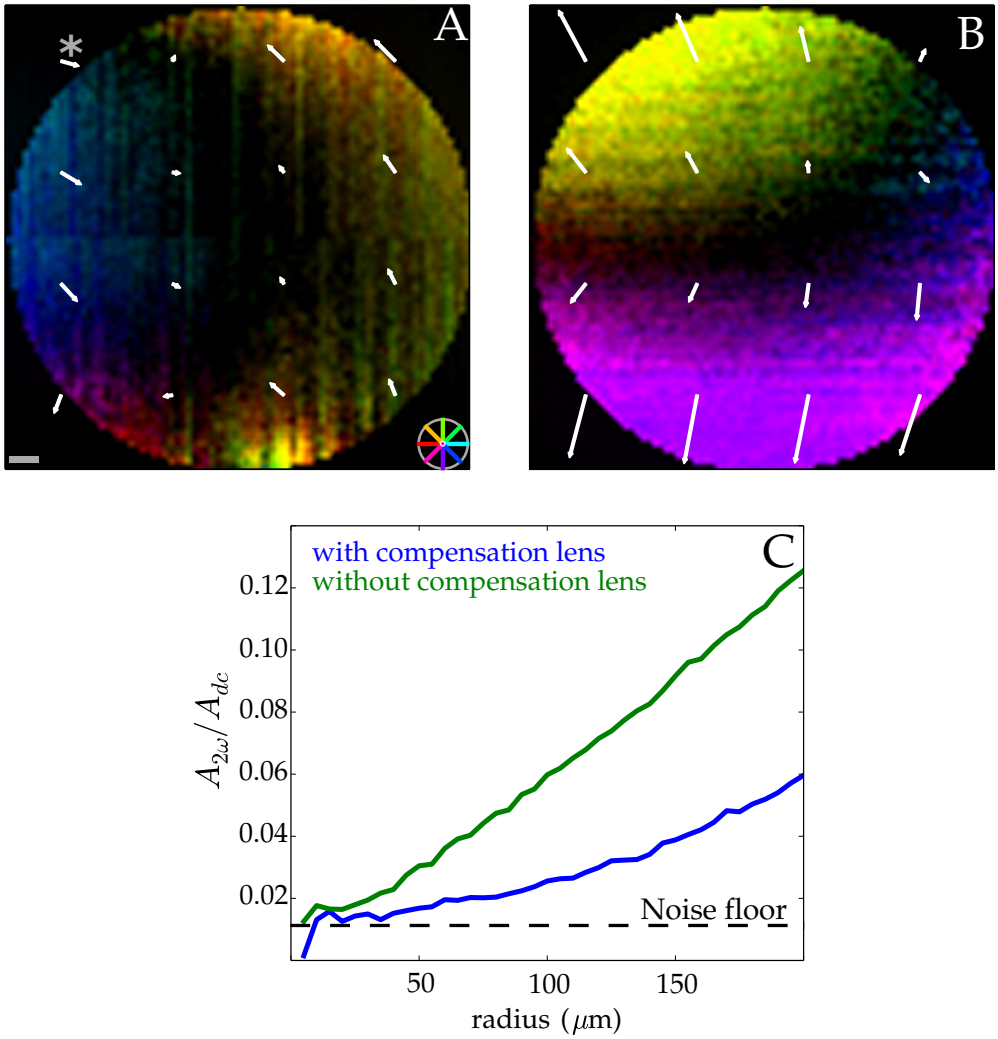

Figure 2.8: (*A*) and (*B*): Nonresonant RP-CARS images (2850 cm^{-1}) of the glass bottom of a WillCo-dish plate taken with (*A*) and without (*B*) the compensation lens. The images were built in the HSV ("Hue","Saturation","Value") colour space, mapping the ϕ values onto the 'hue' channel, as shown in the colour wheel in the bottom right corner of (*A*), and mapping the ratio between $A_{2\omega}$ and A_{dc} onto the 'value' channel, while keeping the saturation channel values at maximum. The average local hue is indicated by the direction of the white arrows, whereas the average local value is indicated by their length. Scale bar: 25 µm. The length of the arrow labelled with * corresponds to a ratio $A_{2\omega}/A_{dc}$ equal to 0.04. Acquisition time: 6 minutes for 100 × 100 pixels. (*C*): Plot of the ratio $A_{2\omega}/A_{dc}$ averaged over a circumference as a function of the radius of the latter. The circumference is centred in the middle of the scan area.

The preservation of the polarisation characteristics of the incident beams all over the field can also be useful in other CARS implementations, e.g. P-CARS, where linearly polarised pump-and-probe and Stokes beams at different angles, and polarised detection, are used in order to suppress the non-resonant background [116].

2.2.4 Experimental validation of the large-field scanning technique

As an experimental validation of the described methods, I report an RP-CARS large-scale (0.5 mm $\times$ 0.5 mm) image of a pair of mouse nerve rootlets at their point of emergence from the spinal cord [215]. The field of interest was identified by using bright-field microscopy (Fig. 2.9A) and then imaged by RP-CARS to visualise the CH_2-rich myelin of the nervous fibres (Fig. 2.9B). The measured average spatial orientation of the CH_2 bonds inside the PSF is shown in Fig. 2.9C.

In order to verify whether the polarisation-based information is correctly retrieved even in the peripheral parts of this large-scale image, the spatial orientation of individual myelin walls is compared with their average ϕ value. Since most of the CH_2 bonds inside myelin are oriented parallel with respect to the wall surface, in the absence of polarisation distortions the average ϕ value corresponds to the myelin wall orientation. Fig. 2.10 demonstrates that the average ϕ value coincides within the experimental errors with the spatial orientation of the fibre in the centre of the image (where the polarisation distortions were minimised by adjusting the compensating retarders) and that they are extremely consistent (the average mismatch is less than 7 degrees) even in the far peripheral areas of this large-field image, where the polarisation distortions are largest.

Biological sample preparation and observation

Unfixed spinal cord of a 23-month-old wild-type mouse (C57BL/6 strain, Harlan Italy, Correzzana, Italy) was used. The spinal cord was frozen at -80 °C immediately after the explant and kept at this temperature until the observation.

The thawed tissue was put in the central well of a Krebs-Henseleit-buffer (K3753 Sigma-Aldrich, St. Louis, Missouri, U.S.A.)-filled WillCo dish (GWSt-3512, WillCo Wells, Amsterdam, the Netherlands) and kept immobilised with a glass coverslip glued to the lateral polystyrene support of the dish. The tissue was finally imaged in the epi-direction through the thin (0.17 mm) glass bottom of the dish central well.

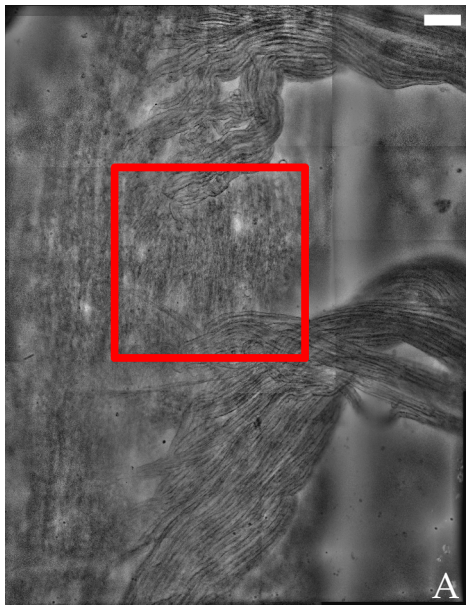

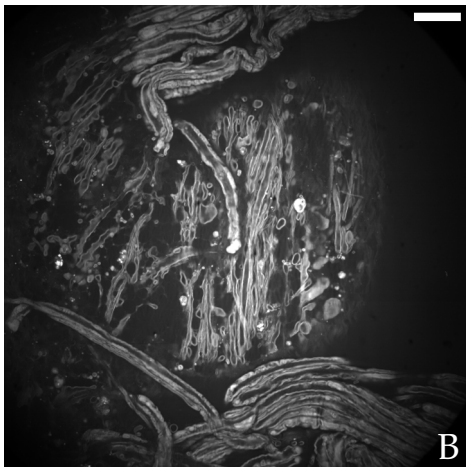

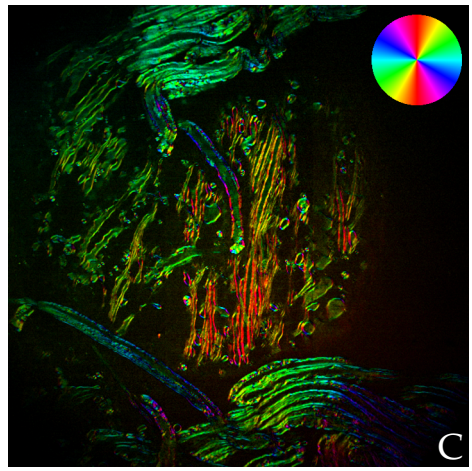

Figure 2.9: Large-scale RP-CARS image (2850 cm^{-1}, CH_2 bonds) of a couple of mouse-nerve rootlets at their point of emergence from the spinal cord. (*A*): Bright-field image. Scale bar: 100 µm. The image is a mosaic made by stitching 3×3 tiles acquired by moving the sample stage. (*B*): RP-CARS image of the region in red square in (*A*), created by mapping A_{dc} to grey-values. Scale bar: 50 µm. (*C*): RP-CARS image of the same region as in (*B*). This image is colour- and intensity-coded by using the HSV colour space as in Fig. 2.5D. The colour-coding scheme of the hue-mapped orientation is shown in the colour circle in the top right corner of the panel. (*B*) and (*C*) are mosaics made by automatic stitching 3×3 tiles acquired by scanning different field regions with the galvanometric mirrors.

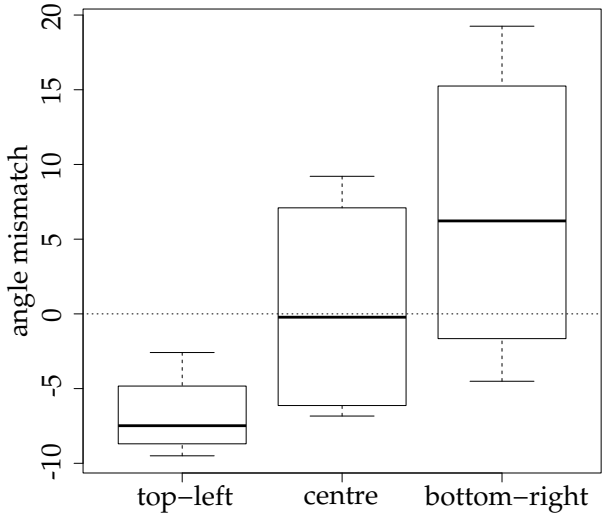

Figure 2.10: Box plot of the difference between the ϕ values of the CH_2 bonds inside the myelin walls and the spatial orientation angles of the respective myelin walls in diverse areas of the image field depicted in Fig. 2.9. The dotted line shows the zero difference point, i.e. where the data would lie in absence of polarisation distortions.

2.3 PULSE CHARACTERISATION

During my Ph.D. program I have contributed to the development (led by other researchers) and experimental implementation of a simple new method to completely determine the characteristics of the pump-and-probe pulse and the Stokes pulse in a coherent anti-Stokes Raman scattering microscope at sample level without additional autocorrelators.

This approach, described in great detail in Ref. [216], relies on the delay line, ubiquitous in CARS microscopes, to perform a convolution of the pump-and-probe and Stokes pulses as a function of their relative delay (δt) and is based on the detection of the photons emitted from an appropriate nonlinear sample. This method bears some similarity to the so-called Frequency-Resolved Optical Gating (FROG) [217], but the presented approach, thanks to the simplifying assumptions described above, does not necessitate complex iterative algorithms to analyse the collected spectra [218].

By characterising the intensities of the emitted non-resonant FWM and SFG signals as a function of δt, the pulses duration at the sample level can be straightforwardly measured, as demonstrated below. Additionally, by performing a spectral analysis, the GDD of each pulse can be directly determined. The only assumption behind this approach is that the nonlinear responses of the chosen medium are only

weakly dependent on the wavelength of the excitation photons, at least within the bandwidths of the pulses, which can be easily verified experimentally.

The retrieved information regarding the pulse duration and chirp can be exploited to optimise the spectral resolution in CARS spectroscopy and also the contrast in CARS imaging.

2.3.1 Theory

The electric field of a Fourier-limited Gaussian pulse having duration τ, amplitude $A^{1/2}$, and centred around an angular frequency ω, can be described as:

$$F_{\text{transform limited}}(t) = \sqrt{A}\exp\left(-2\frac{t^2}{\tau^2}\ln 2\right)\exp\left(-i\omega t\right). \tag{2.19}$$

After travelling through a dispersive medium, a laser pulse acquires a GDD, quantified here by a parameter a. Neglecting third-order dispersion terms and higher, the chirped pulse can be described as:

$$F(t) = \sqrt{A'}\exp\left(-2\frac{t^2}{\tau_{out}^2}\ln 2\right)\exp\left[-i\omega t + 8it^2 a\left(\frac{\ln 2}{\tau\tau_{out}}\right)^2\right], \tag{2.20}$$

where:

$$\tau_{out} = \sqrt{\tau^2 + \left(8\frac{a}{\tau}\ln 2\right)^2} \tag{2.21}$$

is the pulse duration at the output of the dispersive medium and A' the new amplitude.

In the following passage, I shall refer to the Stokes and pump-and-probe pulses of typical two-colour CARS implementations by using S and p subscripts in the relevant variables. The pulses travel through several dispersing elements in the setup, including, for example, the scan and tube lenses, the microscope objective and any additional glass element introduced to tune their chirp. In the following, a will refer to the overall GDD. The amplitudes of the sum-frequency-generation signal A_{SFG} and of the four-wave mixing one A_{FWM} can be written as:

$$\begin{aligned} A_{SFG}(t,\delta t) &= \sigma_{SFG}F_p(t+\delta t/2)F_S(t-\delta t/2) \\ A_{FWM}(t,\delta t) &= \sigma_{FWM}F_p(t+\delta t/2)F_S^*(t-\delta t/2)F_p(t+\delta t/2) \end{aligned} \tag{2.22}$$

where σ_{SFG} and σ_{FWM} describe the process efficiencies, and the "$*$" superscript indicates the complex conjugate of the field. Here positive time delays δt correspond to the pump beam arriving later than the Stokes beam, and I shall take into account

only the contribution to the FWM signal generated from the absorption of two pump photons and the stimulated emission of a Stokes one.

Second-harmonic generation (SHG) from the pump pulses and from the Stokes pulses will also be generated. Since these obviously do not depend on δt, they do not contain cross-correlation terms between the two different pulses and therefore will not be further considered in the following passage.

The squared moduli of the Fourier transforms of A_{SFG} and A_{FWM} provide their spectra:

$$\begin{aligned}
\tilde{I}_{SFG}(\omega,\delta t) &\propto \exp\left(-\frac{\begin{array}{r}16A^{(0)}_{SFG}\delta t^2 + 8A^{(1)}_{SFG}\delta t(\omega_p+\omega_S-\omega)+\\ + A^{(2)}_{SFG}(\omega_p+\omega_S-\omega)^2\end{array}}{4D_{SFG}}\right)\\
\tilde{I}_{FWM}(\omega,\delta t) &\propto \exp\left(-\frac{\begin{array}{r}32A^{(0)}_{FWM}\delta t^2 - 16A^{(1)}_{FWM}\delta t(2\omega_p-\omega_S-\omega)+\\ + A^{(2)}_{FWM}(2\omega_p-\omega_S-\omega)^2\end{array}}{4D_{FWM}}\right).
\end{aligned} \tag{2.23}$$

The explicit expressions of the coefficients in Eq. 2.23 are reported in Table 2.1.

From Eq. 2.23 it is straightforward to notice that, at fixed δt, the spectra are Gaussian curves with amplitudes (I_{SFG} and I_{FWM}) and centres ($\omega_{\text{centre},SFG}$ and $\omega_{\text{centre},FWM}$) depending on δt. The amplitudes of the Gaussian curves as a function of δt are:

$$\begin{aligned}
I_{SFG}(\delta t) &\propto \exp\left(-\frac{4\beta_p\beta_S\delta t^2}{\beta_p+\beta_S}\right)\\
I_{FWM}(\delta t) &\propto \exp\left(-\frac{8\beta_p\beta_S\delta t^2}{2\beta_p+\beta_S}\right),
\end{aligned} \tag{2.24}$$

where β_p and β_S are defined in Table 2.1. The full-widths at half maximum are:

$$\begin{aligned}
W^2_{SFG} &= \left(\frac{1}{\beta_p}+\frac{1}{\beta_S}\right)\ln 2\\
W^2_{FWM} &= \left(\frac{1}{2\beta_p}+\frac{1}{\beta_S}\right)\ln 2.
\end{aligned} \tag{2.25}$$

$A_{SFG}^{(0)}$	$\beta_p\alpha_S^2 + \alpha_p^2\beta_S + \beta_p\beta_S^2 + \beta_p^2\beta_S$
$A_{SFG}^{(1)}$	$\beta_p\alpha_S - \alpha_p\beta_S$
$A_{SFG}^{(2)}$	$\beta_p + \beta_S$
D_{SFG}	$(\alpha_p + \alpha_S)^2 + (\beta_p + \beta_S)^2$
$A_{FWM}^{(0)}$	$\beta_p\alpha_S^2 + 2\alpha_p^2\beta_S + \beta_p\beta_S^2 + 2\beta_p^2\beta_S$
$A_{FWM}^{(1)}$	$\beta_p\alpha_S + \alpha_p\beta_S$
$A_{FWM}^{(2)}$	$2\beta_p + \beta_S$
D_{FWM}	$(2\alpha_p - \alpha_S)^2 + (2\beta_p + \beta_S)^2$
α_i	$4a_i(\tau_i\tau_{out,i})^{-2}\ln^2(2)$
β_i	$\tau_{out,i}^{-2}\ln 2$

Table 2.1: Explicit expressions of the coefficients displayed in Eq. 2.23. i is defined as: $i \in (p, S)$.

The FWHMs can be straightforwardly determined experimentally by monitoring I_{SFG} and I_{FWM} while moving the delay line. Inverting Eq. 2.25 allows the calculation of the values of $\tau_{out,p}$ and $\tau_{out,S}$:

$$\begin{aligned} \tau_{out,p}^2 &= 2(W_{SFG}^2 - W_{FWM}^2) \\ \tau_{out,S}^2 &= 2W_{SFG}^2 - W_{FWM}^2. \end{aligned} \tag{2.26}$$

If the pulse characteristics at the laser output are known (e.g. because already measured or stated by the manufacturer), then the GDDs at sample level can be retrieved simply by inverting Eq. 2.21. It should be pointed out that, unlike FROG, this can be achieved by detecting the SFG and FWM signals with a point detector, without the need to spectrally resolve the signal. In the event that the durations were not known but the centre frequency of the SFG and FWM signals can be determined (e.g. by acquiring their spectra with a spectrometer), it would still be possible to

retrieve the values of the GDDs. To this end, it should be noted from Eq. 2.23 that the centre frequencies of the spectra shift linearly as a function of δt with rates (S):

$$\begin{aligned} S_{SFG} &\equiv \frac{\mathrm{d}\omega_{\mathrm{centre},SFG}}{\mathrm{d}\delta t} = 4\frac{\beta_p\alpha_S - \alpha_p\beta_S}{\beta_p + \beta_S} \\ S_{FWM} &\equiv \frac{\mathrm{d}\omega_{\mathrm{centre},FWM}}{\mathrm{d}\delta t} = -8\frac{\beta_p\alpha_S + \alpha_p\beta_S}{2\beta_p + \beta_S}. \end{aligned} \tag{2.27}$$

Inversion of Eq. 2.27, after measuring the rates and calculating the values of $\tau_{out,p}$ and $\tau_{out,S}$, yields the values of α_p and α_S:

$$\begin{aligned} a_p &= -\frac{W_{FWM}^2 S_{FWM} + W_{SFG}^2 S_{SFG}}{8\tau_{out,p}^2} \\ a_S &= \frac{W_{SFG}^2 S_{SFG} - W_{FWM}^2 S_{FWM}}{8\tau_{out,S}^2} \end{aligned} \tag{2.28}$$

and, straightforwardly, of τ_p, τ_S, a_p, and a_S:

$$\begin{aligned} \tau_p^2 &= \frac{\beta_p \ln 2}{\alpha_p^2 + \beta_p^2} \\ \tau_S^2 &= \frac{\beta_S \ln 2}{\alpha_S^2 + \beta_S^2} \\ a_p &= \frac{\alpha_p}{4(\alpha_p^2 + \beta_p^2)} \\ a_S &= \frac{\alpha_S}{4(\alpha_S^2 + \beta_S^2)}, \end{aligned} \tag{2.29}$$

yielding the complete characterisation of the pulses at the sample level.

2.3.2 Experimental optimisation of the spectral resolution

Finally, by exploiting the approach described in Section 2.3.1, the amount of GDD needed to achieve the optimal spectral resolution in my setup is determined by analysing the characteristics of the pulses starting from the original situation (i.e. in the absence of SF6 glasses). In the following passage I shall indicate with L_p (L_S) the length of the glass blocks placed in the pump (Stokes) path. The parameters calculated in the absence of SF6 glasses ($L_p = L_S = 0$), averaged over 20 repetitions of each experiment, are reported in Tab. 2.2. It is interesting to note that in the

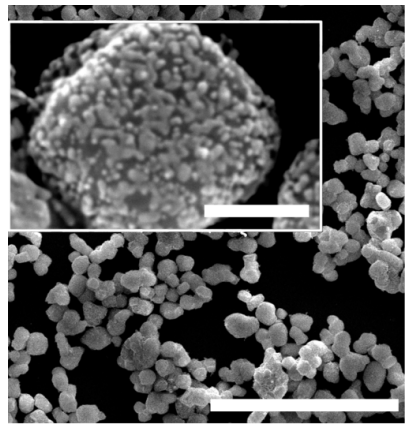

Figure 2.11: SEM image (made by another experimenter) of barium-titanate-core/gold-shell nanoparticles used for the experimental work described in Section 2.3.2 (scale bar: 5 μm). Inset: magnified view of an individual nanoparticle showing the decoration of the core with gold clusters (scale bar: 200 nm).

original condition, even if both pulses cross similar amounts of glass in the setup, they reach the sample with a difference in GDD $\sim$10000 fs^2. This is quite likely due to a setting of the OPO cavity introducing a negative chirp in the Stokes beam that compensates the positive one introduced by the additional optics.

As the non-linear material of choice for this measurement, barium-titanate-core/gold-shell nanoparticles (with an average diameter of 300 nm) were used, owing to their strong nonlinear optical properties. A Scanning Electron Microscopy (SEM) image (made by another experimenter) of these nanoparticles deposited on a microscope glass slide is shown in Fig. 2.11. These nanoparticles are described in Section 5.3, while their full synthesis and characterisation details are reported elsewhere [219, 220].

A combination of glass-block lengths was then determined, namely $L_p = 10$ cm and $L_S = 25$ cm, following the characterisation in the original configuration, in order to yield similar GDDs (30000 fs^2) for both pulses at the sample level. The parameters calculated in this configuration are also reported in Tab. 2.2. The characterisation of SFG and FWM yielded pulse durations consistent with the original configuration and also GDD values in agreement with those determined for $L_p = 0$ and $L_S = 0$, increased by the calculated GDDs introduced by the glass. The increase in spectral resolution with the latter choice of glass lengths was demonstrated by measuring the spectrum of liquid methanol in the C-H stretch region (shown in Fig. 2.12) and comparing it with the spectrum calculated using the pulse characteristics determined with this algorithm. The height of the Raman peaks and the amount of

	No glass	Optimal amount of glass
$\tau_{out,p}(fs)$	244 ± 6	545 ± 35
$\tau_{out,S}(fs)$	125 ± 20	810 ± 14
$\tau_p(fs)$	155 ± 5	150 ± 12
$\tau_S(fs)$	120 ± 10	113 ± 3
$a_p(fs^2)$	10500 ± 600	28600 ± 4000
$a_S(fs^2)$	1500 ± 300	32700 ± 1200

Table 2.2: Pulse parameters before and after the chirp optimisation. "No glass": measurements taken without SF6 glass on the beam paths. "Optimal amount of glass": measurements taken with 10 cm of SF6 glass in the pump beam path and 25 cm in the Stokes beam path. These amounts were chosen in order to obtain a comparable pulse chirp at the sample plane for both beams. τ_{out}: pulse length out of the dispersive medium. τ: pulse length at the sample plane. a: pulse chirp at the sample plane. p and S indicate the "pump" and "Stokes" beams, respectively.

non-resonant background were adjusted to yield the best fit to the data, while their positions were fixed at 2944 cm^{-1} and 2836 cm^{-1}, with widths of 34 and 21 cm^{-1} respectively, according to Ref. [221]. Fig. 2.12 also shows the calculated spectra corresponding to $L_p = 10$ cm and $L_S = 15$ cm and to $L_p = 0$ and $L_S = 0$. The spectrum calculated with the pulse parameters determined with the analysis presented here provides a very good match to the experimental data, further confirming the validity of this approach.

By analysing the methanol spectrum shown in Fig. 2.12, the spectral resolution of the setup is estimated to be about 50 cm^{-1}: sufficient to specifically target the CH_2 symmetric and antisymmetric stretch modes (at 2850 cm^{-1} and 2885 cm^{-1}) avoiding at the same time the CH_3 modes [222, 223].

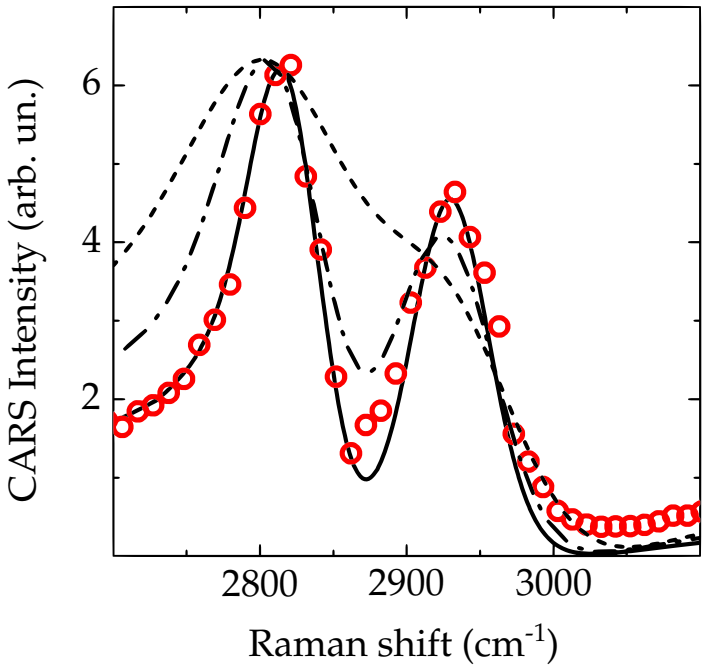

Figure 2.12: CARS spectra of liquid methanol. The experimental spectrum, measured with $L_{pump} = 10$ cm and $L_{Stokes} = 25$ cm is shown with red circles. The corresponding calculated spectrum is shown as a black solid line. Spectra calculated for $L_{pump} = 0$ cm and $LStokes = 0$ cm (dashed line) and $L_{pump} = 10$ cm and $L_{Stokes} = 15$ cm (dash-dotted line) are also reported for comparison.

3 OBSERVATIONS

In this chapter I shall describe several applications of the RP-CARS technique to the observation of biological samples that I performed during my Ph.D. course. In particular, I shall first show how RP-CARS could be used in the context of optical tractography of myelinated fibres. I shall then demonstrate how RP-CARS imaging can be exploited to assess the myelin health status in mouse sciatic nerves in a chemical model of myelin damage and in an animal model of Krabbe disease, an important human leukodystrophy. Finally, I shall report on the first observation of a positive correlation between myelin-wall varicosity and age in mouse sciatic nerves made possible by RP-CARS imaging.

3.1 VISUALISATION AND OPTICAL TRACTOGRAPHY OF MYELINATED FIBRES

3.1.1 Myelin visualisation

CARS microscopy is a powerful imaging method to observe myelin. Although this technique is limited in several applications by the presence of a non-resonant background [109], this is not the case with myelin imaging owing to its extremely high concentration of CH_2 bonds, comparable in the animal body only to adipose tissue or to some excretory glands, which ensures a large imaging contrast.

In order to demonstrate the potentiality of this technique in myelin imaging in terms of contrast and resolution, I acquired large-magnification images of myelinated axons (Schmidt-Lanterman incisures) from *ex-vivo* sciatic nerves explanted from WT mice, shown in Fig. 3.1. As discussed in Section 1.2.2, the sub-diffraction-limit-resolution capability of CARS microscopy allowed the capturing of images with very fine details, as visible in Figure. To highlight faithfully the achievable imaging contrast, the images are shown here without saturated pixel and with the largest dynamic range possible.

By exploiting an automated procedure to combine the large-field-of-view approach described in Section 2.2.3 with sample scanning, I was able to acquire extremely wide images of neural tissue with high resolution. Fig. 3.2 shows a transversal section of a spinal cord (3.9 mm $\times$ 2.85 mm) explanted from a rat in which Experimental

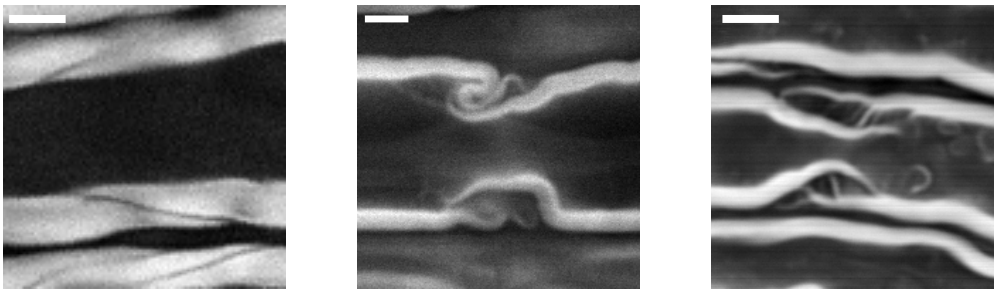

Figure 3.1: High resolution CARS images of Schmidt-Lanterman incisures in mouse sciatic nerves. The images are shown here without saturated pixel and with the largest dynamic range possible. Scale bar: 4 μm.

Autoimmune Encephalomyelitis (EAE), an animal model for human multiple sclerosis [224], was induced. The high-resolution of the image (pixel size: 375 nm × 375 nm) makes it possible to discriminate the individual myelinated axons. In this image it is possible to identify two areas of hypomyelination localised in the ventral region that can be interpreted as EAE lesions.

3.1.2 Optical tractography

RP-CARS can be used also as an optical method for myelinated-fibre tractography by exploiting the phase value (ϕ) described in Section 2.2.4. It will be recalled that ϕ is a pixel-based indicator of the average in-plane orientation of the CH_2 bonds and therefore also of the local orientation of the myelin wall, on average parallel to the targeted bonds.

In order to demonstrate the feasibility of this approach, myelinated nerve fibres in *ex-vivo* mouse (C57BL/6J strain, Jackson Laboratory) sciatic nerve were observed. After the surgery, the nerve explants were incubated in constantly oxygenated (95% O_2, 5% CO_2) Krebs-Henseleit buffer (K3753 Sigma-Aldrich) kept at 30 °C to prevent damage to the fibres. Fig. 3.3A displays the values of A_{dc}: individual myelinated axons can be easily identified. Fig. 3.3B shows the same region depicted in Fig. 3.3A coloured in the HSV space as in Fig. 2.5D. The colour of the myelin walls in the Figure changes smoothly according to their local direction, demonstrating that this method correctly identifies ordered structures and detects both the average orientation of the molecular bonds of interest and the local orientation of the myelinated fibre. All the RP-CARS Figures reported in this thesis were generated with a custom-made Python software application (Listing 1) reported in Appendix A.

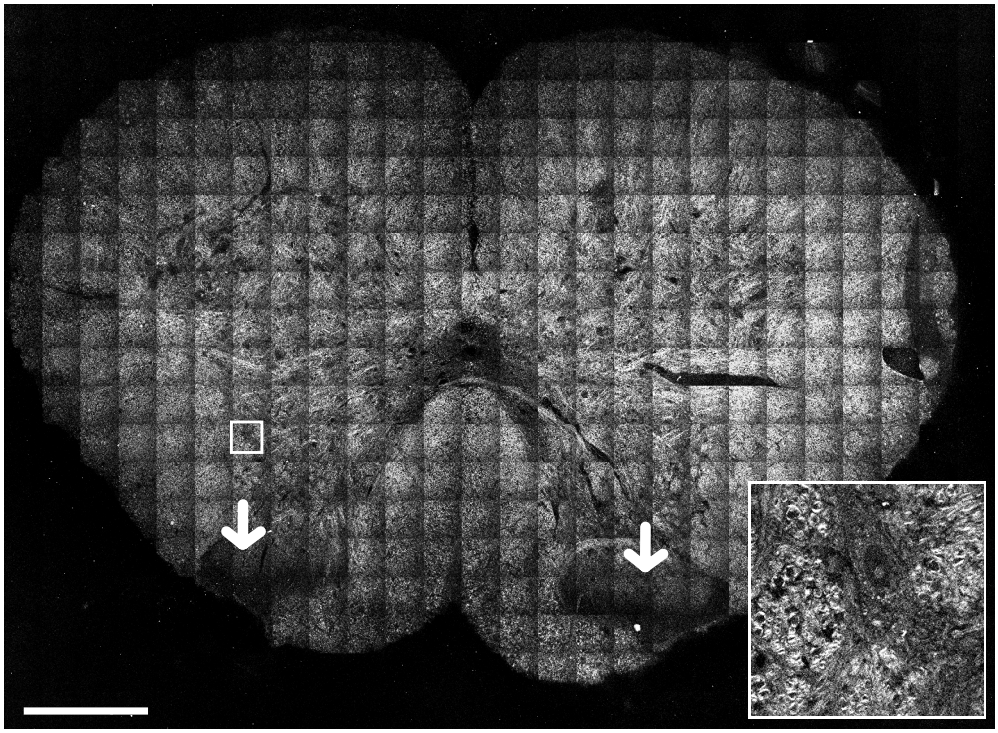

Figure 3.2: Large-scale (3.9 mm × 2.85 mm), high-resolution (pixel size: 375 nm × 375 nm) CARS image of a lumbar transversal section of an EAE rat spinal cord. The image composed of 26 × 19 tiles was acquired by moving the sample stage. A custom-made bidimensional Fourier filter was employed to suppress stitching artefacts. Inset: magnification of the area indicated by the white square. Scale bar: 450 μm. The areas indicated by the arrows can be interpreted as lesions induced by the EAE.

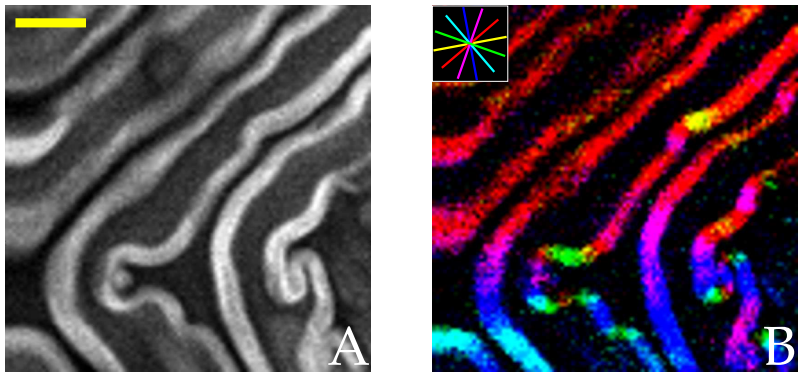

Figure 3.3: Small scale (30 μm × 30 μm, 100 × 100 points) RP-CARS image of a longitudinal section of myelinated nerve fibres in *ex-vivo* mouse sciatic nerve acquired in the epi-direction. Scale bar: 6 μm. (*A*): Grayscale image created with the A_{dc} signal. (*B*): This image is colour- and intensity-coded by using the HSV colour space as in Fig. 2.5D. Inset: colour-coding scheme of the hue-mapped orientation.

After successfully testing the orientation-retrieval method for small-scale and small-pixel size images, I verified if this approach could also be used for tractography in large-scale and large-pixel-size images by visualising a 100 μm-thick coronal slice of mouse (C57BL/6J strain, Jackson Laboratory) formaldehyde-fixed brain in the hyppocampal region (bregma: −1.2 mm). The images displayed in Fig. 3.4 are mosaics made by manually stitching 276 50 × 50-pixels tiles and then processing them with a bi-dimensional band-block Fourier filter (suppressing Fourier components on the vertical and horizontal coordinate axes with 1% tolerance, using ImageJ [225]) to remove the stitching artefacts. In such a large scale image, this method allows the rapid visualization of the in-plane direction of the myelinated nervous fibres. The results are fully consistent with the data in literature [226]: all the major fibre bundles that surround the hyppocampus are clearly recognisable (corpus callosum, cingulum, dorsal fornix, alveus, fimbria and stria medullaris) and visualised with the expected in-plane directions. An important difference between the image shown in Fig. 3.3 and this one is that in the former the pixel size is smaller than the myelin wall thickness, while in the latter a single pixel encompasses multiple myelin walls. Despite this noteworthy difference, RP-CARS is able to generate precise tractographic images seamlessly in the two conditions.

Based on this proof-of-principle, CARS-based tractography could develop into a technique complementary to MRI offering much higher spatial resolution and more straightforward orientation detection, though at present tested only *ex-vivo*. In fact, non-PR CARS was already employed to retrieve large-scale morphological data of nervous fibres [227] and to specifically validate MRI microstructure measure-

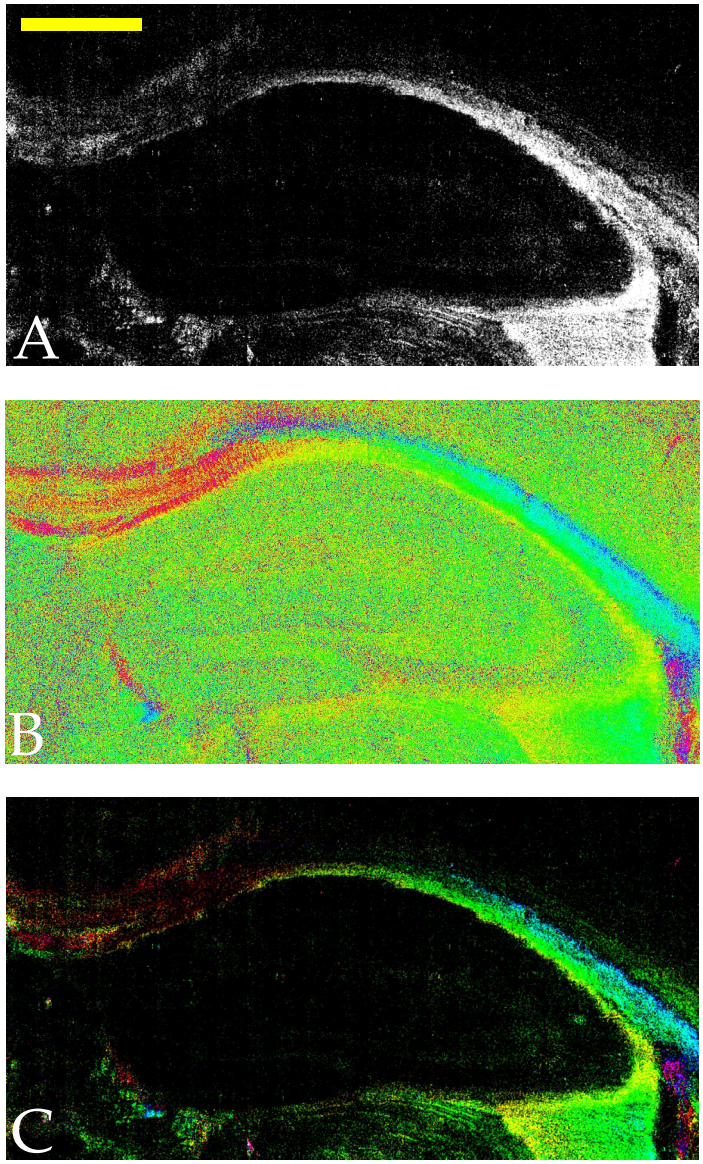

Figure 3.4: Large-scale (2.2 mm × 1.1 mm), high-resolution (pixel size: 2.4 µm × 2.4 µm) RP-CARS image of a coronal section of the mouse brain hyppocampus taken in trans-direction in about 1 hour. Scale bar: 400 µm. (*A*): Grayscale image created mapping $A_{2\omega}$ signal as intensity. (*B*): RGB image created mapping ϕ signal onto the visible colour spectrum. The areas that appear dark in (*A*) and in (*C*) (low $A_{2\omega}$ signal levels) here appear as randomly coloured due to the noise in ϕ. (*C*): The image is colour- and intensity-coded as in Fig. 2.5D.

ments [228]. The introduction of PR CARS imaging in this field of research would allow the optical retrieval of the large-scale fibre orientation without the need for computationally-intensive algorithms or time-consuming imaging at the single-fibre level.

3.2 OPTICAL READOUT OF MYELIN HEALTH IN A CHEMICAL–DAMAGE MODEL

3.2.1 Introduction

As discussed in Section 1, CARS imaging is a valuable tool to specifically evaluate the health condition of myelinated fibres. In Ref. [167] this task was accomplished by computing the g-ratio for each fibre in the CARS images. This indicator is the ratio between the inner and the outer diameter of the fibre, and it is a widely adopted image-based measure of myelin healthiness, typically determined by means of various imaging techniques, e.g. TEM. However, this approach has some drawbacks: tracing individual fibres is a very time-consuming process and the readout is an average over the circumference of the fibre. To overcome some of these limitations a new method was recently presented to assess myelin health based on 2D Fourier transform of CARS images [171]. However, this method just assesses the presence of directional features in the image and is not based on intrinsic molecular characteristics. Finally, as the readout is image-wide based, it is not suitable for single-fibre studies. On the contrary, the method that I developed, based on RP-CARS imaging as a tool to assess the myelin health status, relies on the readout of the intrinsic molecular architecture rather than on image-analysis algorithms. This implementation takes advantage of the already mentioned molecular order and spatial anisotropy that characterise acyl chains of healthy myelin [229] and stems from the observation that this order is lost in damaged myelin [167].

3.2.2 Theory

As shown in Eq. 1.2 in Section 1.2.1, the polarisability involved in a degenerate CARS process is proportional to the third-order susceptibility tensor χ_{ijkl}, where i, j, k, l run over the coordinates $\{x, y, z\}$.

Following Ref. [175], the third-order susceptibility of the linear acyl chains of the phospholipidic moiety of the myelin layers can be described as that of a system having cylindrical symmetry with respect to the chain axis (here the z axis), which

in the case of degenerate four-wave mixing has 21 non-zero terms, with only four of them being independent [230], as already discussed in Section 2.1.3:

$$\begin{aligned} c_{11} &= \chi_{xxxx} = \chi_{yyyy}, \\ c_{18} &= \chi_{xxyy} = \chi_{yxyx} = \chi_{yxxy} = \chi_{xyyx} = \chi_{xyxy} = \chi_{yyxx}, \\ c_{16} &= \chi_{xxzz} = \chi_{yyzz} = \chi_{zxzx} = \chi_{zxxz} = \chi_{xzzx} = \chi_{xzxz} = \chi_{zyzy} = \chi_{zyyz} = \chi_{yzzy} \\ &= \chi_{yzyz} = \chi_{zzxx} = \chi_{zzyy}, \\ c_{33} &= \chi_{zzzz}. \end{aligned} \tag{3.1}$$

When the acyl chain is rotated with respect to the laboratory reference systems, the new susceptibility tensor can be calculated as:

$$\chi_{IJKL} = C_{Ii} C_{Jj} C_{Kk} C_{Ll} \chi_{ijkl}, \tag{3.2}$$

where uppercase (lowercase) indices refer to the laboratory (molecule) reference system, and C_{Ii} is the direction cosine between axis I and i, expressed in terms of the x-conventional Euler angles φ, ϑ, ψ. It is clear to see that a rotation around the z-axis – e.g. $\varphi = \pi/4$ – leaves the susceptibility tensor unaltered, as is expected due to the rotational invariance of the system around the same axis, only if $c_{18} = c_{11}/3$. This leaves only three independent terms in the tensor.

The susceptibility of a "disordered" myelin system, i.e. a system in which the acyl chains are not perfectly aligned along the Z axis, can be calculated by integrating the susceptibility tensor over the angular distribution of the chains [195]. For the sake of simplicity, the susceptibility of the disordered system, χ_{IJKL}, is calculated by assuming that the distribution is uniform with respect to ϑ in the interval from zero to an angle ϑ_0 and zero elsewhere, where the ϑ_0 describes the amount of disorder, ranging from 0 (completely ordered system) to $\pi/2$ (completely disordered system):

$$X_{IJKL} = \frac{1}{2\pi\,(1 - \cos\vartheta_0)} \int_{-\pi}^{\pi} d\varphi \int_{0}^{\vartheta_0} d\vartheta \sin\vartheta C_{Ii} C_{Jj} C_{Kk} C_{Ll} \chi_{ijkl}. \tag{3.3}$$

Integration over ψ is not needed since the system is already uniformly distributed around the z axis. It is worth noting that this angular averaging preserves the sym-

metry of the susceptibility around the Z axis. Therefore, X_{IJKL}, similarly to χ_{ijkl}, has only 21 non-zero terms with only three of them being independent:

$$\begin{aligned}
\tilde{c}_{11} &= c_{11} - q_1 t + \left(\frac{q_0}{2} + \frac{q_1}{3}\right) t^2 - \frac{3q_0}{8} t^3 \left(1 + \frac{t}{5}\right), \\
\tilde{c}_{16} &= c_{16} + \frac{1}{2}\left(q_0 + \frac{q_1}{3}\right) t - \frac{1}{6}\left(5q_0 + \frac{q_1}{3}\right) t^2 + \frac{q_0}{2} t^3 - \frac{q_0}{10} t^4, \\
\tilde{c}_{33} &= c_{33} - 2(q_0 - q_1)t + 2\left(q_0 - \frac{q_1}{3}\right) t^2 - q_0 t^3 + \frac{q_0}{5} t^4,
\end{aligned} \tag{3.4}$$

where $q_0 = c_{33} + c_{11} - 6c_{16}$, $q_1 = c_{11} - 3c_{16}$, and $t = 1 - \cos\vartheta_0$. Quite obviously, the limit of perfectly ordered system, $t \to 0$, yields $X = \chi$.

As shown in Section 2.1.3, in the case of interest here of linearly polarised, rotating pump-and-probe beam and circularly polarised Stokes beam, both propagating perpendicularly to the Z axis, the generated CARS signal contains a dc component (A_{dc}), a component ($A_{2\omega}$) oscillating at 2ω, and a component ($A_{4\omega}$) oscillating at 4ω:

$$\begin{aligned}
A_{dc} &= 3\tilde{c}_{11}^2 + 2\tilde{c}_{11}\tilde{c}_{16} + 14\tilde{c}_{16}^2 + 2\tilde{c}_{33}\tilde{c}_{16} + 3\tilde{c}_{33}^2, \\
A_{2\omega} &= 4\left(\tilde{c}_{11}^2 - \tilde{c}_{33}^2\right), \\
A_{4\omega} &= \tilde{c}_{11}^2 - 2\tilde{c}_{11}\tilde{c}_{16} - 6\tilde{c}_{16}^2 - 2\tilde{c}_{33}\tilde{c}_{16} + \tilde{c}_{33}^2.
\end{aligned} \tag{3.5}$$

A further component at 6ω would be present if a rotating linearly-polarised Stokes beam were used instead of a circularly polarised one, which would give access to a more detailed description of the orientation distribution function [195]. Anyway such description is beyond the scope of this thesis: I shall show that the first two components, A_{dc} and $A_{2\omega}$, are fully sufficient to characterise the myelin health status in the present demyelinating model. For this reason also rotating the Stokes-beam (linear) polarisation would be an unnecessary technical complication, as discussed in Section 2.1.2.

Within the limits of a perfectly ordered system, $t \to 0$, the equations above reduce to those reported in Section 2.1.3, while some algebraic manipulations confirm that for $t \to 1$, i.e. for a completely randomised system, $A_{2\omega} = A_{4\omega} = 0$. This behaviour is shown in Fig. 3.5A, which shows the inverse tangent of $A_{2\omega}/A_{dc}$ (top graph) and the values of A_{dc}, $A_{2\omega}$, and $A_{4\omega}$ as a function of t (bottom graph), calculated by taking the values of the components of χ from Ref. [175]. The squared modulus of the third-order polarisability ($|P|^2$) of the system when excited with linearly polarised pump-and-probe photons and circularly polarised Stokes photons is shown in Fig. 3.5B as a function of the angle η between the polarisation plane of the pump-and-probe beam and the X-Y plane. In particular, $|P|^2$ for a completely disordered system

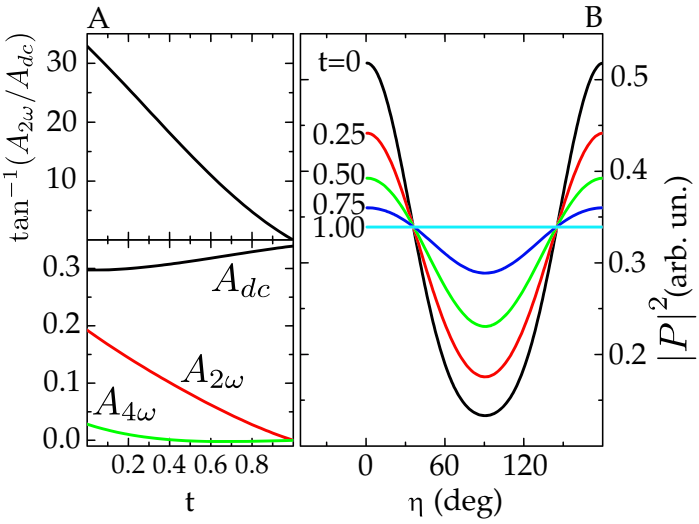

Figure 3.5: (*A*) Top graph: inverse tangent of $A_{dc}/A_{2\omega}$ as a function of the disorder parameter t. Bottom graph: dc and ac amplitudes (in arbitrary units) of the squared modulus of the third-order polarisability ($|P|^2$) of the system when excited with linearly polarised pump-and-probe photons and circularly polarised Stokes photons as a function of t. (*B*): $|P|^2$ at different values of the disorder parameter as a function of the angle η between the polarisation plane of the pump-and-probe beam and the X-Y plane.

($t = 1$) has no dependence on the pump-beam polarisation orientation. Whereas $|P|^2$ in an ordered system ($t < 1$) is highest when the pump beam polarisation orientation is parallel with respect to the molecular-bond dipole and lowest when it is perpendicular to it, with the modulation amplitude increasing with decreasing t.

It is apparent from Fig. 3.5A that the disorder parameter t is closely related to the inverse tangent of $A_{dc}/A_{2\omega}$, which is a quantity – expressed in degrees in the Figure – that can be directly measured with the RP-CARS setup:

$$\alpha = \tan^{-1}\left(\frac{A_{2\omega}}{A_{dc}}\right) \tag{3.6}$$

Notably, the disorder parameter is a ratiometric quantity, allowing the removal of contributions from difficult-to-measure quantities, such as the laser power delivered to the sample, the collection efficiency of the optics, and the sensitivity of the PMTs. To this end it is very convenient to express the relation between A_{dc} and $A_{2\omega}$ as an angle (α) rather than, e.g., with their ratio, as the former is much less sensitive to noise with respect to the latter, especially in regions of the image where the density of CH_2 bonds is low (small A_{dc}).

3.2.3 Results

In order to obtain controlled and measurable myelin damage, explanted sciatic mouse nerves were acutely exposed to lyso-PtdCho, a well-known demyelinating agent [167, 231]. Lyso-PtdCho exerts its action via a calcium-dependent pathway [167] and induces a swelling and a disruption of the myelin architecture, from the outside to the inside of each fibre (partially at the expense of the fibre lumen) as depicted in the inset of Fig. 3.6. It was recognized early on, by using TEM [231], that the main effect of lyso-PtdCho was to disorganise the juxtaposition of the concentric myelin layers, thereby making them less compact and less symmetrically ordered around the fibre main axis. However, the important role played in this process by the lytic enzymes calpains and phospholipase A_2 (PLA2) was acknowledged only recently [167].

It is reasonable to assume that, during the lyso-PtdCho-induced demyelinating process, PLA2 hydrolyses the myelin phospholipids into lysophospholipids and fatty acids. The increase in molecular spatial degrees of freedom caused by the PLA2-catalysed cleavage of the second acyl bond in the glycerol moiety (or the removal of the fatty acid from the membrane) translates in my model simply into an increase of t. It is quite likely that these are not the only biochemical processes occurring in this experimental model and therefore my theoretical model cannot be expected to yield quantitative results (partly because the numerical values of the susceptibility-tensor elements are not universal and they might change during the process), yet it is tempting to quantify the amount of damage in the myelin layers with the parameter α.

In order to compare α to a reference health indicator, for each nerve fibre I computed the g-ratio (schematised in the inset of Fig. 3.6), at present the best image-based index of myelin damage known in the literature [167, 232–234]. The g-ratio for healthy myelin fibre is usually about 0.6-0.7. In my demyelination model the g-ratio decreases as a function of time as the damage progresses. It should be noted that other authors [167] report that the exposure to lyso-PtdCho induces an increase (rather than a decrease) of the g-ratio. This apparent discrepancy occurs because Cheng *et al*. [167] take into account only the undamaged myelin in the calculation of the g-ratio, while I include the entire myelin sheath, i.e. both the healthy and the swollen parts. I decided to compute the g-ratio in this way, even though higher g-ratio values are consistently associated with myelin damage in the literature, because I observed that the myelin compact region completely disappears while the nervous fibre alteration process is manifestly still ongoing.

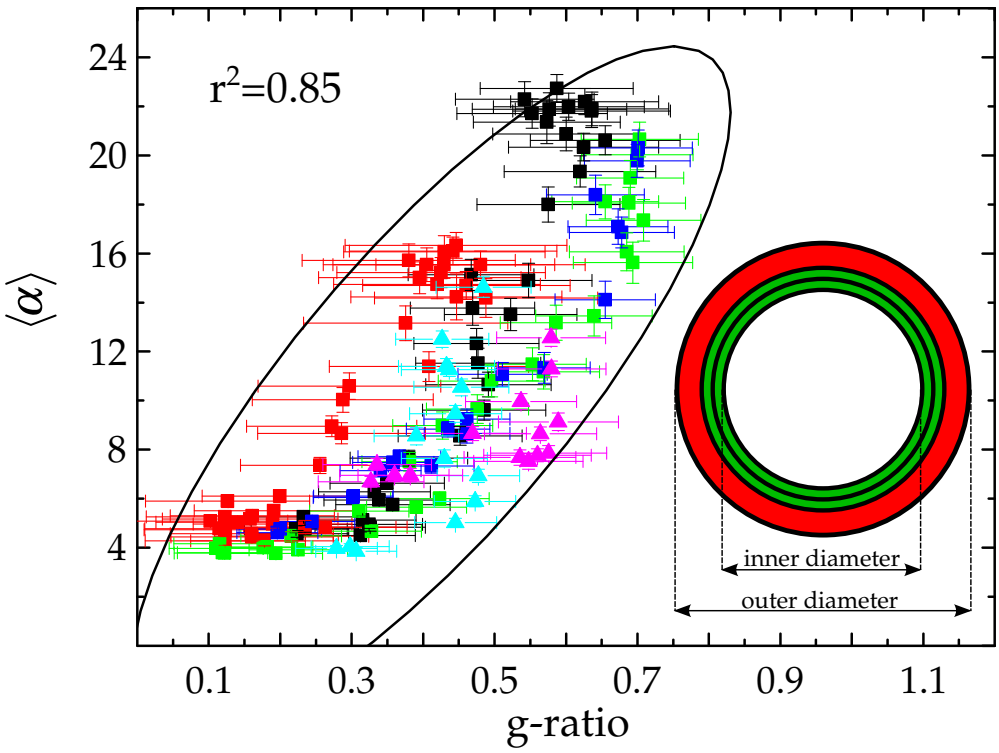

Figure 3.6: Correlation plot between the g-ratio and the effective angle $\langle\alpha\rangle$. Different colours denote different nervous fibres, while different shapes (squares, triangles) denote experiments on different nerves (different mice). The ellipse describes the 95% confidence interval. The correlation coefficient (r^2) is 0.85 and the p-value is <0.001 (Spearman's rank correlation coefficient). Inset: In the lyso-PtdCho damage model the chemical demyelinating agent induces myelin damage (in red) and swelling from the outside to the inside of the fibre. The swelling induces both a reduction of the internal lumen and a growth of the global nerve fibre diameter. Therefore, since the inner diameter is reduced and the outer diameter is enlarged, the ratio between the two (g-ratio) is greatly reduced.

Since the g-ratio is a fibre-based indicator rather than a pixel-based one, I defined an effective angle alpha, $\langle \alpha \rangle$ as:

$$\langle \alpha \rangle = \tan^{-1} \left(\frac{\sum_i A_{2\omega,i}}{\sum_i A_{dc,i}} \right) \tag{3.7}$$

where the index i runs over all the pixels pertaining to the (manually selected) myelin walls.

Consistently with the theoretical model and with the observations reported in [167], $\langle \alpha \rangle$ is found to decrease with time. Notably, I observed a remarkably strong correlation (correlation coefficient: 0.85, p-value<0.001, Spearman's rank correlation coefficient) between the g-ratio values and $\langle \alpha \rangle$, as shown in Fig. 3.6, demonstrating that this technique is well suited to quantifying alterations in myelin sheaths with a fully label-free approach.

In the plot shown in Fig. 3.6, $\langle \alpha \rangle$ saturates at approximately 4 degrees at low g-ratios, corresponding to an $A_{2\omega}/A_{dc}$ ratio of about 7%. The same value is also found by analysing myelin-free image areas, such as the fibre lumen. However, if $\langle \alpha \rangle$ is computed by substituting the scalar sum at the numerator of Eq. 3.7 with a vector summation $\left| \sum_i \overrightarrow{A}_{2\omega,i} \right|$ (i.e. also taking into account the ϕ value of each pixel and computing the magnitude of the resulting vector), the $A_{2\omega}/A_{dc}$ background value drops down to 3%. This value is consistent with the effect caused by the residual distortion of the polarisations present in the incoming beams, as discussed in the Section 2.1.3. Using a scalar mean function is reasonable with sufficiently high $A_{2\omega}$ values but could lead to a slight overestimation of α in regions of low $A_{2\omega}$, where a vector mean function is more appropriate, yet the latter would fail when computed over fibres that are curved in the imaging plane. Following these considerations, I estimate that other effects that could yield polarisation distortions, such as myelin birefringence [196], are negligible in this experimental configuration, consistently with the fact that the imaging was not performed very deeply within the nerve (<40 μm) and that the signal was collected in the epi direction.

Since the presented algorithm is pixel based, it is also possible to colour-map the images with the α value (as shown in Fig. 3.7), yielding a real-time, pixel-based indication of the myelin health status during the acquisitions and to have a very intuitive representation of the on-going damage. On the contrary, using the g-ratio as a measure of the myelin health status requires time-consuming post-acquisition analysis steps, i.e. manually tracing all the fibres.

The pixel-based α value ranges from a minimum of 0 in the ideal case to a sample-specific maximum (21 in this experiment). The sample-specificity of the maximum

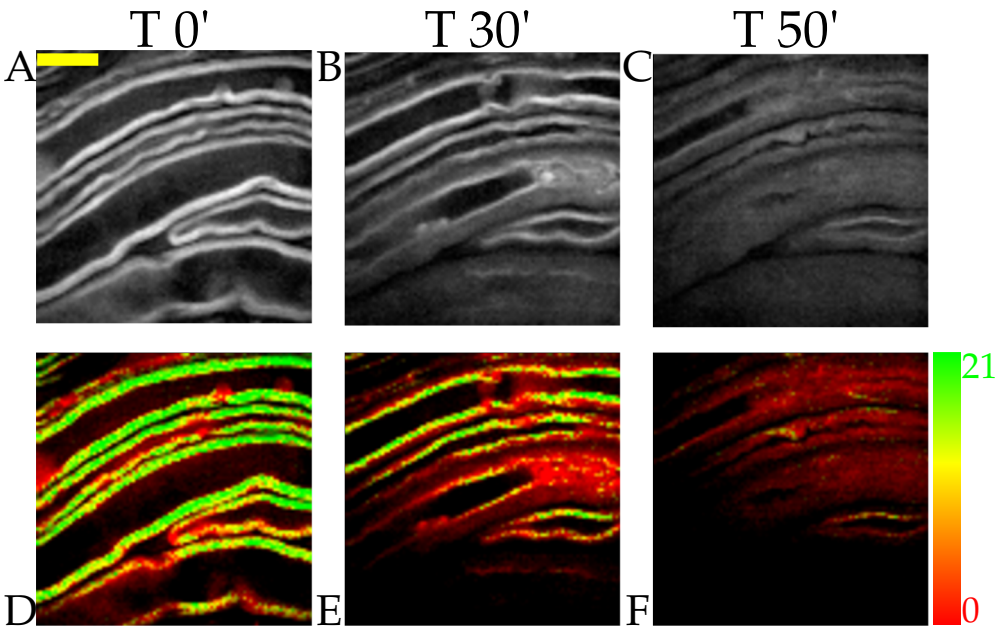

Figure 3.7: Explanted-sciatic-nerve myelinated fibres imaged by RP-CARS. Top row (*A*, *B*, *C*) panels: grayscale images of the A_{dc} signal. Bottom row (*D*, *E*, *F*) panels: colour maps of α. In the HSV colour representation, the hue ranges from red to yellow to green at increasing values of α, as depicted in the colour bar at the bottom-right, while the value is proportional to A_{dc} and the saturation is kept at maximum. Columns represent acquisitions taken immediately after the exposition to lyso-PtdCho (first column), after 30 minutes (second column), and after 50 minutes (third column). Scale bar: 10 μm.

value is a consequence of the sample-related variability of the myelin composition and therefore of the value of the susceptibility tensor. However, as discussed before in this Section, even though it is mandatory to take into account a sample-specific maximum value for α in order to perform comparative studies (similarly to what is commonly done with the g-ratio), the qualitative behaviour of α as function the sample molecular disorder is not expected to change.

It should be noted that there are several factors that can fictitiously reduce α: photomultiplier dark current and CARS non-resonant background can increase the measured value of A_{dc} therefore leading to an underestimation of α. However, this does not significantly affect the images since it is relevant only in pixels associated with small A_{dc} and $A_{2\omega}$ values or, in other words, areas that are coloured in black. It should also be noted that the present method assumes that the symmetry axis of the acyl-chain distribution lies in the imaging plane within the point-spread function. An out-of-plane component of the axis leads to a reduction of the measured value of α. Indeed, in the extreme case when the symmetry axis is perpendicular to the imaging plane (e.g. when the imaging plane is tangent to the myelin wall), this method would erroneously yield $\alpha = 0$. This is visible for example in the lower-left corner of Fig. 3.7D, where the imaging plane is almost tangent to the myelin sheath. Myelinated fibres with a very small radius also lead to a fictitiously reduced angle. These cases are easily recognisable by eye and, therefore, excludable from the analysis.

In conclusion, by correlating the measured anisotropy with the g-ratio, I demonstrated that this technique is well suited to visualizing local alteration in myelin sheaths: the α value can be measured and visualised in real-time on a pixel-by-pixel basis. Furthermore, it does not require three-dimensional acquisitions and complex post-acquisition image analysis.

Biological sample preparation

Adult (aged from P47 to P120) wild type mice (C57BL/6J strain, Jackson Laboratory) were euthanised with cervical dislocation according to the ethical guidelines of the Italian (DL 116/1992) and European Community (86/609/EEC) laws. After death, the sciatic nerves were rapidly surgically explanted and then incubated in constantly oxygenated (95% O_2, 5% CO_2) Krebs-Henseleit buffer (K3753 Sigma-Aldrich) kept at 38 °C to prevent damages to the fibres. The explanted nerves were put in WillCo dishes (GWSt-3522, WillCo Wells) and kept immobilised with a custom-made electrophysiology-type anchor.

Lyso-ptdcho (L4129 Sigma-Aldrich L-α-Lysophosphatidylcholine from egg yolk, >99%) was first dissolved in 38 °C Krebs-Henseleit buffer at a concentration of 100 mg/ml and sonicated for 10 minutes. Lyso-ptdcho solution was added to the

WillCo dish containing the nerves (exposure time: 0-1 h) at the final concentration of 10 mg/ml.

3.3 OPTICAL READOUT OF MYELIN HEALTH IN A GENETIC MODEL OF A LEUKODYSTROPHY

3.3.1 Introduction

Krabbe Disease (KD), also called globoid cell leukodystrophy, is a rare autosomal-recessive sphingolipidosis caused by the inactivation of the galactocerebrosidase (GALC) enzyme [235, 236], with an incidence of one case in 100,000 births. GALC is a lysosomal enzyme implicated in the catabolism of galactolipids, including galactosylceramide and psychosine (PSY), also called galactosyl-sphingosine. Its inactivation causes a cytotoxic increase in the cellular levels of PSY that is thought [237] to be at the origin of the tissue-level effects, even though the precise molecular mechanisms behind its cytotoxicity are still currently under discussion [238–248]. The increase in PSY concentration in the CNS and in the PNS leads to Schwann cell and oligodendrocyte death, causing progressive demyelination associated to reactive astrocytosis [244], microgliosis [249] and neurodegeneration [250]. The onset is often early infantile [235] and, even though several promising treatments at the pre-clinical stage have been proposed in recent years [251–253], a cure for the human disease is still lacking: KD is often fatal in the first years of life [254].

An excellent genetic model of the human KD is represented by the twitcher (TWI) mouse. It is an enzymatically authentic model of KD, since it is derived from a recessive spontaneous nonsense mutation of the GALC gene, and it closely resembles the histological, biochemical and morphological characteristics of human KD [255]. For several reasons, including the ease of access and manipulation, the sciatic nerve is a frequently used sample to study the effect of the disease on the PNS of the TWI mouse [239, 241, 250, 253, 256–258].

Microscopy techniques such as TEM [241, 255], immunofluorescence [241, 247, 248, 251–253] and confocal microscopy [241, 248, 251–253] have been used extensively to study the TWI mouse and they have provided important insights into the understating of the pathogenetic process and in the ideation of possible treatments. After having already shown in Section 3.2 that the degree of anisotropy of the CH_2 bonds in myelin sheaths (quantified with α) presents a significant correlation with their health status in a chemical model of demyelination, in the following Section I shall report the use of RP-CARS to visualise molecular spatial order anomalies in the genetic animal model of a leukodystrophy: the TWI mouse [259].

3.3.2 Results

Qualitative analysis

TWI-mouse phenotype is characterized by rapid myelin degeneration after the symptomatic onset of the disease (P20). This is clearly seen in the Fig. 3.8 which depicts a large-field-of-view CARS image of a sciatic nerve of WT mouse compared to that of a TWI mouse. In the TWI image the myelinated fibres appear sparser: this is because the pump and Stokes beams combination is chosen to target the CH_2 bonds and, in this condition, the demyelinated (or unmyelinated) fibres are invisible, lacking a sufficiently high CH_2 bonds concentration. Moreover, numerous alterations in the myelin-wall morphology are clearly visible.

Higher resolution and magnification sciatic-nerve images are depicted in Fig. 3.9. These images are representative of WT, presymptomatic TWI and symptomatic TWI conditions. The hue in these images is constructed by colour-mapping the pixel-based α value (described in Section 3.2.2). As displayed in this Figure, there is little difference between the WT and the TWI presymptomatic conditions (green colour), while it can be clearly seen that most of the myelinated fibres present ample portions of damaged myelin walls (yellow colour and tortuous appearance) in the TWI symptomatic condition. Unexpectedly, it is occasionally possible to observe long sections of myelin walls with almost normal morphological appearance in the symptomatic TWI condition images (indicated with white arrows in Fig. 3.9C-D), even in the late period after onset (P25). It is worth noting that, despite their almost normal morphology, the α values of these fibres present a large variability. I have found it to vary from the value found in WT or presymptomatic TWI ($\alpha \approx 15$, Fig. 3.9C) to very low values, comparable to other fibres in the same nerve presenting evident morphology alterations (Fig. 3.9D).

Quantitative analysis

For each z-stack I computed the A value by averaging the α values of the pixels associated with myelin, as described at the end of this Section; this value was constructed to be a global label-free optical indicator of the myelin health imaged in the stack. I then averaged the A values to obtain a single value for each animal and the results are shown in Fig. 3.10. It is evident that before the onset age the A values of the TWI mice are constant, while after the onset they decrease in a linear manner ($p = 0.0005$, General Linear Model). In comparison, the A values of the WT mice remain constant over the whole age range (model p-value = 0.0012, adjusted $R^2 = 0.7264$).

In addition, the average A value of presymptomatic TWI mice was found to be slightly higher ($\Delta\alpha \approx 3$) than that of the WT mice ($p = 0.03$, Student t-test). This last result should be treated with caution, due to the small number of presymptomatic

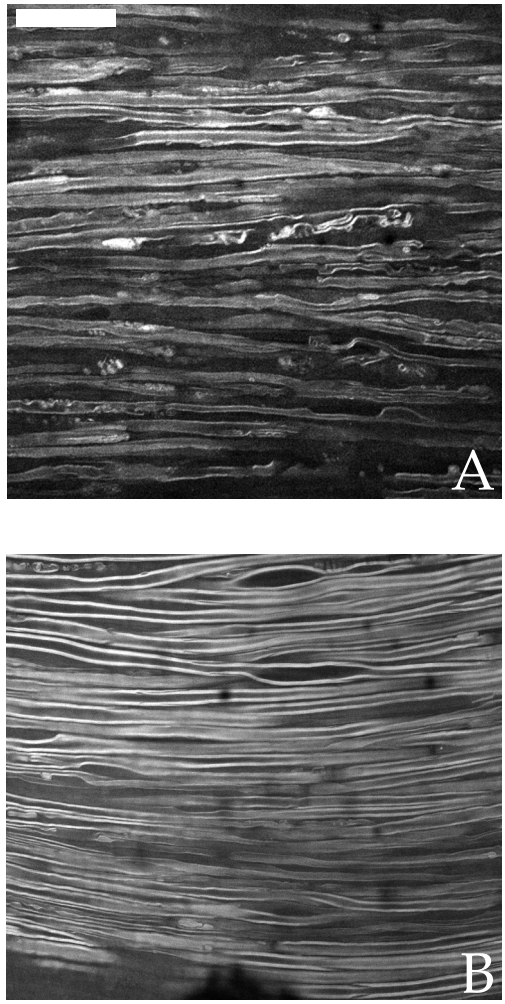

Figure 3.8: CARS images (2850 cm^{-1}, CH_2 bonds) of sciatic nerve optical longitudinal sections from a TWI P21 mouse (*A*) and of a WT P27 mouse (*B*). Scale bar: 40 μm.

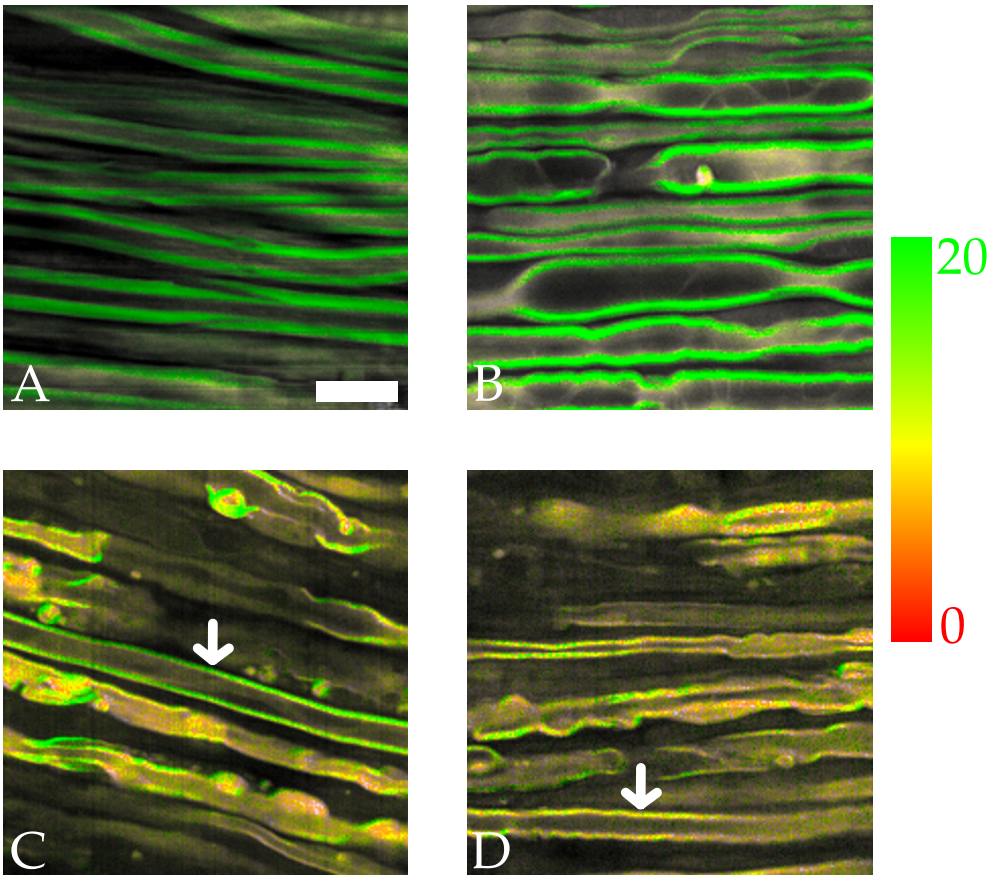

Figure 3.9: RP-CARS images (2850 cm^{-1}, CH_2 bonds) of sciatic-nerve optical longitudinal sections from a WT P27 mouse (*A*), a TWI P20 (pre-symptomatic) mouse (*B*) and TWI P23 and P25 (symptomatic) mice (*C*, *D*). Scale bar: 10 µm. The white arrows indicate sections of morphologically-normal myelin walls. The images were constructed in the HSV (Hue, Saturation, Value) colour space by mapping the value of α onto the hue (from red, $\alpha = 0$, to green, $\alpha \geq 20$, as displayed in the colour bar on the right), the $A_{2\omega}$ signal onto the saturation and the A_{dc} signal onto the value.

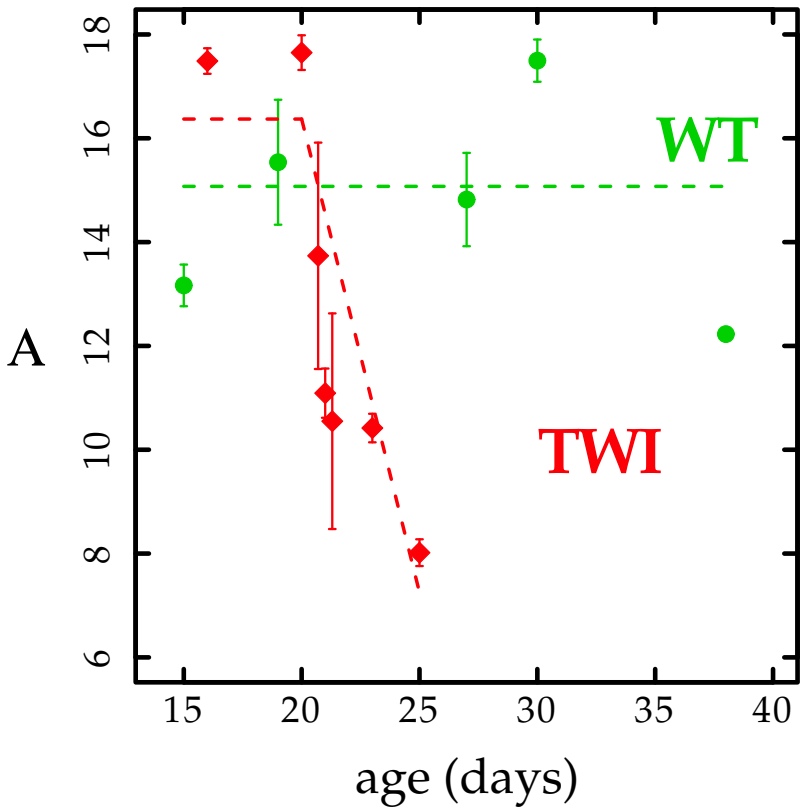

Figure 3.10: Graph of the average A values of WT (green, circles) and TWI (red, diamonds) mice as a function of the age. The dashed lines indicate the predicted values by the statistical model (general linear model). The p-value and the adjusted R^2 value of the statistical model were found to be 0.0012 and 0.7264 respectively. The error bars indicate the standard error of the A averages. X-axis jitter was applied to the P21 observations in order to improve the visualisation.

TWI mice, but it is noteworthy since it could suggest important implications about the structure of myelin in TWI mice before the onset of motor symptoms, as is explained Section 3.3.3.

The average A_{dc} signal intensity in symptomatic TWI mice is generally lower than the WT and presymptomatic TWI mice. In principle a comparison of samples with different intensities might lead to bias in the measured modulations. In order to rule out this possibility, I computed the correlation plot between A_{dc} and α, shown in Fig. 3.11. I chose three z-stacks form WT mice and I manually optimised the threshold on A_{dc} for each individual slice. Great care was taken in order to select only the myelin-wall sections that lie in the optimal focal plane (i.e. only the myelin section in which the acyl chains are coplanar with the focal plane). I then computed the average A_{dc} ($\tilde{A}_{dc}$) and the average α value ($\tilde{\alpha}$) for each thresholded slice. In this way the difference in CARS intensity presumably stems only from the different scattering effect due to the different depth of the focal plane. As the Figure shows, a factor-of-3 change in $\tilde{A}_{dc}$ only produces a difference in $\tilde{\alpha}$ of around 15%. In addition, the (Pearson product-moment) correlation coefficient ($R^2 = 0.25$) between $\tilde{A}_{dc}$ and $\tilde{\alpha}$ was non-statistically significant ($p > 0.05$). I went on to study the effect of the optical scattering on the retrieved α value exploiting numerical simulations and the results are discussed in Section 4.3.

There could be several reasons behind the alteration of the A values, such as a homogeneous shift in the values of α; the emergence of a new population of α values or a change in the shape of the α population distribution. In order to investigate these different hypotheses, I proceeded to study the populations of α values in addition to the already shown averages. To this end I computed the histogram of representative (automatically thresholded) z-stacks in the three different conditions: WT, TWI presymptomatic and TWI symptomatic, shown in Fig. 3.12. It is evident that in the TWI symptomatic condition the histogram is unimodal with a peak between $\alpha = 5$ and $\alpha = 10$. Dissimilarly, in the WT and in the TWI presymptomatic conditions, the histogram appears to be bimodal. The first peak (in a position similar to that of the TWI symptomatic condition) is accompanied by a second peak placed around $\alpha = 20$. The unusual shapes of these histograms could explain why the choice of different thresholds produces only a rather homogeneous shift in the A values (as reported in Section 3.3.2).

In addition, Fig. 3.12 also shows the virtual reconstructions of the myelin walls in the optical transverse plane. From these images it is clear that the α population centred between 5 and 10 corresponds to both the myelin-wall portions that are parallel to the focal plane (in which the CH_2 bonds are coplanar with the focal plane) and, in the case of the TWI symptomatic condition, to the damaged myelin (irrespective of its orientation). As shown in Ref. [207], the (healthy) myelin-wall portions parallel to the focal plane give rise to low measured α values because the

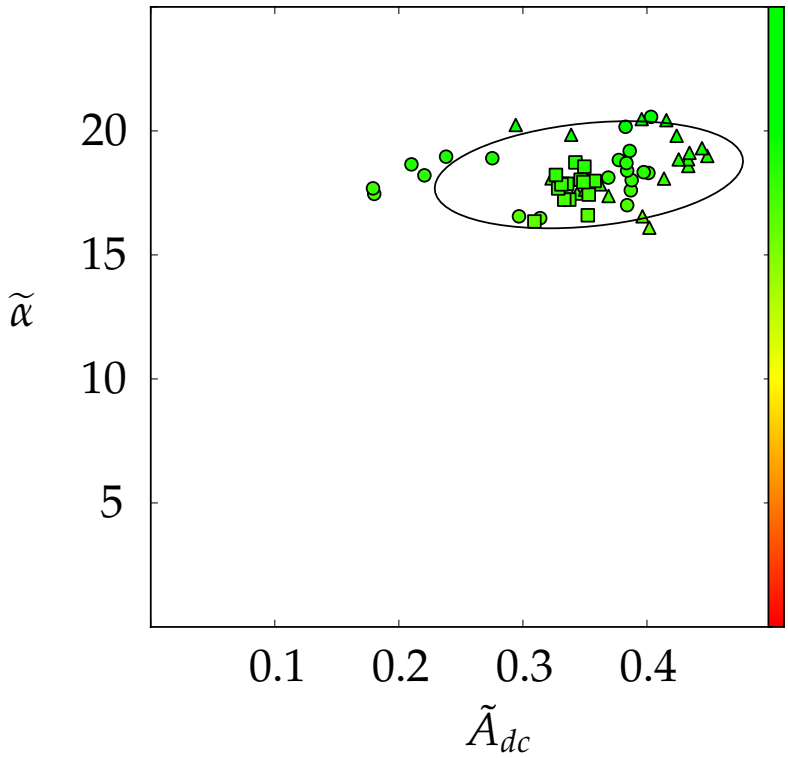

Figure 3.11: Correlation plot between the average alpha value ($\widetilde{\alpha}$) of manually thresholded slices and their average A_{dc} value ($\tilde{A}_{dc}$). Each point represents a slice of a (WT mouse) z-stack (i.e. at different depths inside the tissue) and different shapes denote different z-stacks. The points are colour-coded according to the colour bar shown on the right and consistently with Fig. 3.9. The ellipse shows the confidence interval at twice the standard deviation. The (Pearson product-moment) correlation coefficient ($R^2 = 0.25$) between $\widetilde{\alpha}$ and $\tilde{A}_{dc}$ is not statistically significant ($p > 0.05$).

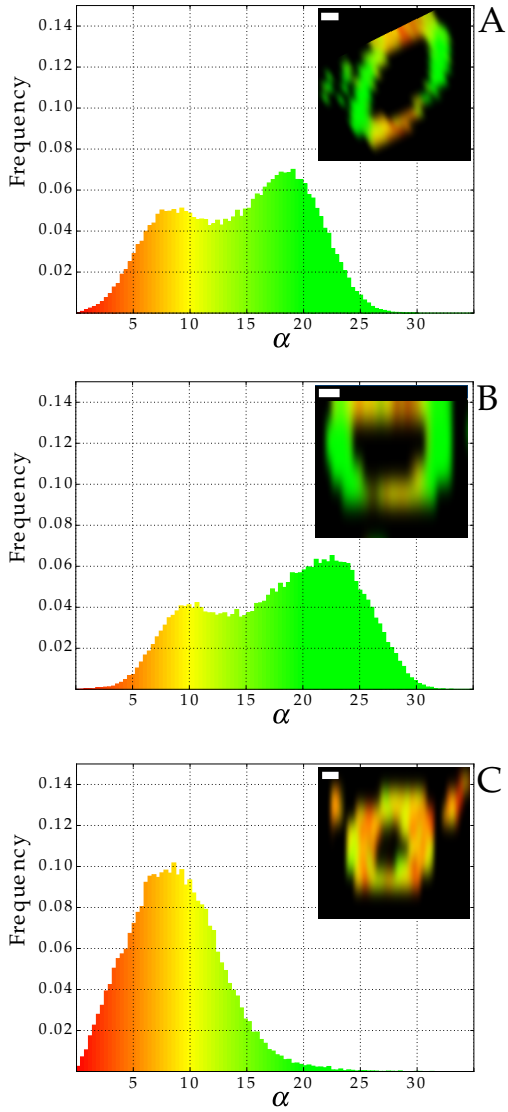

Figure 3.12: Normalised frequency histograms of the α values in a z-stack representative of the WT condition (*A*), of the presymptomatic TWI condition (*B*) and of the symptomatic TWI condition (*C*). Insets: virtual reconstructions of the myelin walls in the optical transverse plane, constructed from the z-stacks corresponding to the same respective histogram. The images are constructed as in Fig. 3.9. The only difference is that the areas below the threshold (automatically chosen as described in Section 3.3.2) and the areas corresponding to non-acquired volumes are displayed in black. Scale bar: 1 µm.

in-plane orientation of their CH_2 bonds is isotropic, similarly to what happens in damaged-myelin (regardless, in the latter case, of the section plane orientation).

Moreover, this observation implies that, even though some of the myelin-wall portions parallel to the focal plane are indeed included in the analysis by my automatic thresholding method (together with the orthogonal portions), this does not alter the final results of the comparison between TWI and WT. In fact, including the parallel myelin portions in the average has the effect of decreasing the WT (and presymptomatic TWI) average while the symptomatic TWI average is unaffected, and therefore tends only to decrease the significance of the observed difference.

TEM imaging

The ultrastructural characterization of (P30 $\pm$ 2) TWI sciatic nerves was performed by Dr. Valentina Cappello (Center for Nanotechnology Innovation @NEST, Istituto Italiano di Tecnologia, Piazza San Silvestro 12, I-56127 Pisa, Italy). In agreement with CARS data, it showed disorganisation of the myelin sheath architecture. As shown in Fig. 3.13, it is possible to observe within the sheath several points of discontinuity between subsequent windings. This effect is more evident in the periphery of the sheath, both in the inner and in the outer side.

The final result of this alteration is highlighted by an increase in the myelin-sheath thickness in comparison with control samples belonging to WT littermates, in agreement with the data already reported in the literature [241]. Exploiting TEM imaging, it was already shown that TWI mice are characterised by a larger g-ratio than WT mice[241, 260]. It should be noted that this difference is in agreement with the decreased α value that I observed, since the two quantities are correlated [167, 207].

Biological sample preparation

Twitcher heterozygous C57Bl/6J (B6.CE-Galc^{twi}/J) and WT (C57Bl/6J) mice (Jackson Laboratory, Bar Harbor, Maine, U.S.A.) were generously donated by Dr. A. Biffi (San Raffaele Telethon Institute for Gene Therapy, Milan, Italy) and maintained under standard housing conditions. Twitcher heterozygous mice (Galc$^{twi/+}$) were used as breeder pairs to generate homozygous (Galc$^{twi/twi}$) TWI mice. Five WT and seven (four males and three females) homozygous TWI mice (aged from P15 to P38) were euthanised with cervical dislocation according to the ethical guidelines of the Italian (DLGS 26/2014) and European Community (2010/63/EU) laws. After death, the sciatic nerves were rapidly surgically explanted. Genomic DNA was extracted from the clipped tails of mice by Proteinase K lysis buffer as previously described [261] and the genetic status of each mouse was determined by Dr. I. Tonazzini (NEST, Scuola

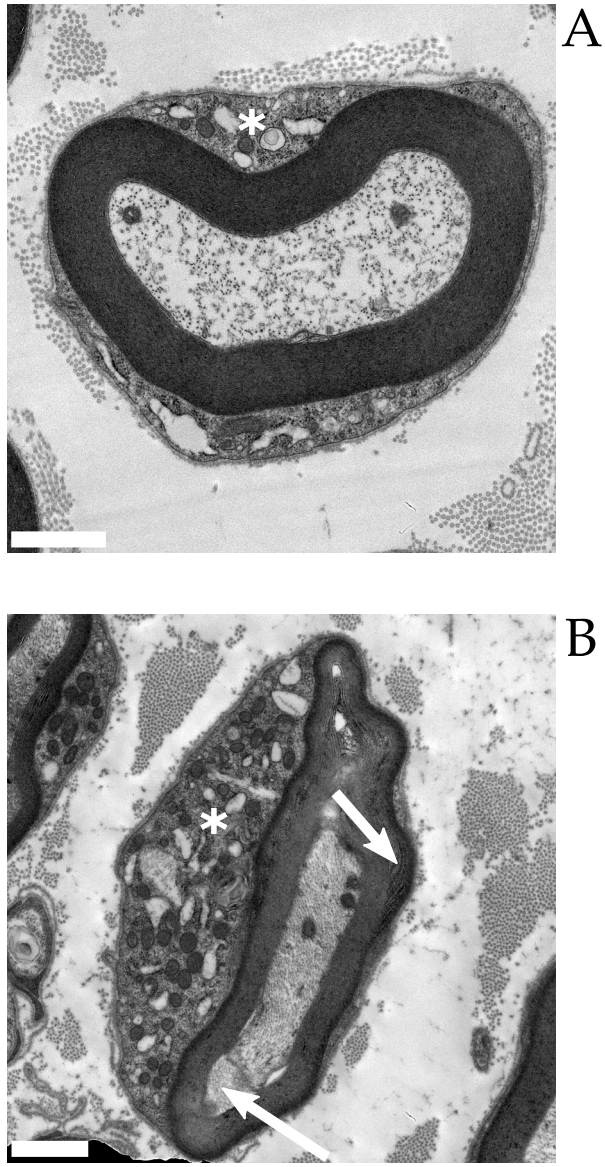

Figure 3.13: Representative TEM images of Schwann-cell wrappings in the sciatic nerve of P30 WT (*A*) and TWI (*B*) mice. The asterisk (*) indicates the Schwann cells. The degeneration of cellular organelles (mainly mitochondria that appear vacuolated) in the cytosol of the Schwann cell in (*B*) indicates the forthcoming death of the myelinating cell. The two arrows in (*B*) indicate the deregulation of the staking in the outer as well in the inner portions of the myelin sheath. Scale bar: 1 μm.

Normale Superiore and Istituto Nanoscienze-CNR, Pisa , Italy) from the genome analysis of the twitcher mutation, as reported in Ref. [262].

The explanted nerves were put in WillCo dishes (GWSt-3522; WillCo Wells, Amsterdam, The Netherlands) filled with Krebs-Henseleit buffer (K3753; Sigma-Aldrich, Saint Luis, Missouri, U.S.A.) and kept immobilized with an electrophysiology-type anchor (SHD-40; Warner Instruments, Hamden, Connecticut, U.S.A.). 3.5 z-stacks were acquired on average for each nerve.

Data and statistical analysis

A custom-made software application (Listing 1 in Appendix A) written in Python (Python Software Foundation, Beaverton, Oregon, U.S.A.) is used to compute the pixel-based α value in post-processing as described in Section 3.2.2.

A second custom-made Python software application (reported as Listing 2 in Appendix A) computes the average A value for each z-stack acquisition in the following way: first the optical slice along the z-axis with the highest average A_{dc} value is identified. Then the isodata algorithm [263] is applied to this slice in order to find the A_{dc} threshold value. After that, all the pixels in the z-stack with A_{dc} values higher than the threshold are selected and the average of their α values is taken as the A value of the z-stack. I used the highest threshold value that satisfies the Ridler-Calvard equation but, as a control, I also checked that different choices, for example using the lowest valid threshold value, do not lead to significant differences in the statistical analysis. Just a rather homogeneous shift in the A values was observed when different thresholding methods were chosen.

All the statistical computations were performed with R software (R Foundation, Vienna, Austria [264]). TWI mice P20 or younger were considered as (motor) presymptomatic phenotype, in accordance with the literature [255]. The A values derived from the z-stacks acquired from the same nerve were averaged and they were assigned a weight equal to the inverse of their standard error. The averaged A values (and their weight) were used as the dependant variable in a General Linear Model [265] while the genotype ($Galc^{twi/twi}$ or $Galc^{+/+}$) and the interaction between the genotype, the phenotype (symptomatic or presymptomatic) and the age (relative to the onset) were used as independent variables. Finally, the Student t-test was used to compare the averaged A values between presymptomatic and symptomatic TWI mice.

3.3.3 Discussion

The results reported in the previous Section show that RP-CARS is able to extract in real time information about structural arrangements in a fresh biological structure

(myelin) over sub-μm spatial scales. Moreover, the combination of RP-CARS and TEM observations gives useful insights into the degeneration of myelin during the post-onset period: these data suggest that the myelin degeneration involves, at least in the initial state, the contemporaneous appearance of numerous nanometric-sized (sub-optical resolution) structural alterations in the same myelin wall segment. I would like to stress that the label-free nature of the CARS imaging makes it possible to visualise the sample without the manipulations associated with labelling processes commonly needed for fluorescence imaging, or with the tissue fixation and staining procedures required by TEM imaging, significantly minimising the possibility of unwanted artefacts in the myelin microstructure.

There are in principle some confounding factors that should be taken into account. In this regard, even though it was shown that CARS absolute molecular-orientation measures are indeed partially altered by the presence of a structured non-resonant background [197], I would like to stress that this does not influence comparative measurements, such as the ones presented in Fig. 3.10, since the non-resonant fraction of the CARS signal is of similar magnitude among the different acquisitions (TWI versus WT). In addition, the influence of the myelin birefringence (together with other effects that could yield polarisation distortions) on RP-CARS measures was already described in Section 3.2.3 and was found to be negligible, partly thanks to the fact that the imaging was performed in the epi-direction and not at a great depth within the nerve (< 30 μm). Moreover, the last two conditions, together with the non-analysed polarisation detection employed in this setup, also make the effect of scattering on my PR measurements negligible [266]. Finally, it should be pointed out that the observed discrepancies between TWI and WT mice could be due to different kinds of sub-PSF disorganisations, such as nanoscopic-sized intra sheath disorder or morphological changes of the myelin wall (e.g. invaginations or extrusions of the surface occurring on sub-micrometric spatial scales), since the RP-CARS technique does not allow for distinguishing among them.

A quite unexpected result was the sporadic observation (even in the late period after the onset) of normally appearing myelin walls associated with variable α values. Normally appearing myelin walls in TWI mice of similar ages had already been observed [257] by means of TEM imaging and interpreted as remyelinated fibres. In the pursuit of a cure, the comprehension of the mechanisms behind the survival or the remyelination of those rare myelin walls while the nervous fibres around them are already completely demyelinised would be of great clinical interest.

In addition, it is possible to state that the myelin structure is probably altered at the nanoscopic level even before the clinical onset of the symptoms, when its microscopic morphological appearance seems otherwise normal. A possible explanation for this observation is the reduced expression of proteins, such as Myelin Basic Protein (MBP), one of the most abundant proteins in myelin, in the juvenile

period of TWI mice, as described in Ref. [258]. One of the functions of MBP consists of promoting the adhesion of the cytosolic surfaces of compact myelin [267], and therefore its reduction can be expected to lead to a general reduction of the intrinsic molecular order. However – to the best of my knowledge – there are no reported observations of decreased myelin interlamellar adhesion either in the CNS [268] or in the PNS [257] of TWI mice of similar ages. On the other hand, the CH_2 bonds of the proteins are usually much less ordered with respect to those of the lipid-moiety of the myelin and this could be particularly true for intrinsically disordered proteins such as MBP [267], i.e. those lacking an ordered three-dimensional structure. It could be hypothesized therefore that the reduction in the number of disordered protein-related CH_2 bonds leads to the observed global increase in the order of the myelin CH_2 bonds and this effect would overcompensate the possible presence of microstructural effects of the MBP deficit.

Although KD is usually diagnosed in a non-invasive manner, it is worth highlighting that nerve biopsies are still required for the diagnosis of several other neuropathies, as discussed in 1.3.2. I speculate that the promising result presented here could open up new possibilities in the future for the development of less-invasive methods aimed at human neuropathies diagnosis.

In conclusion, I exploited RP-CARS to demonstrate a post-onset progressive decrease in the spatial orientation order of the CH_2 bonds inside the myelin walls of TWI-mice sciatic-nerve fibres. This is the first time that this promising microscopy technique has been applied to a genetic-pathology model and my observations prove the experimental validity of this microscopy technique. Finally, I believe that the obtained results might be of great interest for a deeper understanding of the pathogenic mechanisms underlying human Krabbe disease.

3.4 EFFECTS OF AGEING ON THE MYELINATED FIBRES

3.4.1 Introduction

Concomitantly with the increase in the average lifespan experienced in the last few decades, an increase in the incidence of neurological disorders was observed and this trend is expected to continue in the near future [269]. Nonetheless, the study of PNS senescence disorders is a research field that is still rather neglected with respect to its CNS counterpart, despite the fact that the incidence of peripheral neuropathies is up to 15% in people over the age of 40, while around 2% in the general population [270, 271]. Additionally, over 65 years of age the incidence of PNS diseases is higher and their progression is faster [272–275].

The most common causes for acquired peripheral neuropathies are: toxic-drug exposure, trauma and systemic illnesses. In spite of this it is possible to hypothesise that age-related PNS changes can trigger progressive nerve degeneration in otherwise healthy aged people. Among the possible suggested mechanisms behind this condition, there are: reduced physiologic turnover of PNS components, increased susceptibility to local nerve entrapment, poor nerve circulation and reduced regeneration from subclinical damage [276, 277]. In order to test this hypothesis, several studies have been conducted both in animals and in humans but the results are still far from being conclusive [276, 278–284].

In addition, even though rodents are frequently used as a model to study the PNS ageing [276, 280–284], there is not yet a general consensus about the progression rate of the nerve damage, nor definitive evidence of possible differences among animal species [285]. In the following passage I shall describe the exploitation of the RP-CARS technique to study the effects of ageing on sciatic-nerve myelinated fibres in the same cohort of WT mice examined longitudinally at different time points.

3.4.2 Results and Discussion

I exploited the capability of RP-CARS microscopy to visualise the myelin sheaths in mouse sciatic nerves (Fig. 3.14A) and to determine their local in-plane orientation (ϕ) with sub-micrometric resolution (as described in Section 3.1.2). Colour-mapping the ϕ values makes it possible to appreciate subtle differences in the local orientation of the nerve fibres. This is depicted in Fig. 3.14 which shows two representative cases, i.e. the youngest (3.14B) and oldest (3.14C) mice that I studied. The "banded" appearance of the myelin walls of the older mouse, to be compared to the uniformity of the colour of the younger animal, implies frequent variation of the local orientation of the myelin sheaths. By exploiting the data-analysis pipeline described at the end of this Section, I was able to quantify this variation over a chosen spatial scale with the average resultant length β (an index of angular dispersion which is equal to one minus the angular variance). As depicted in Fig. 3.14D, I found that β, calculated over a spatial scale of 15 μm, displays a significant ($p < 0.05$) decrease as a function of the animal age (Spearman correlation coefficient: -0.9), i.e. an increase in the spatial disorder of the sheath local orientation.

The analysis of RP-CARS data also showed that the myelin A values, as described in Section 3.3.2, do not show a significant correlation with mouse age (p-value>0.05, computed exploiting the same statistical procedure used for the resultant length β).

In conclusion, the RP-CARS data showed a decrease of the resultant length β with ageing in the myelin sheath orientations on a micrometric spatial scale in the sciatic nerve. This observation can be interpreted as the onset of an unexpected "varicos-

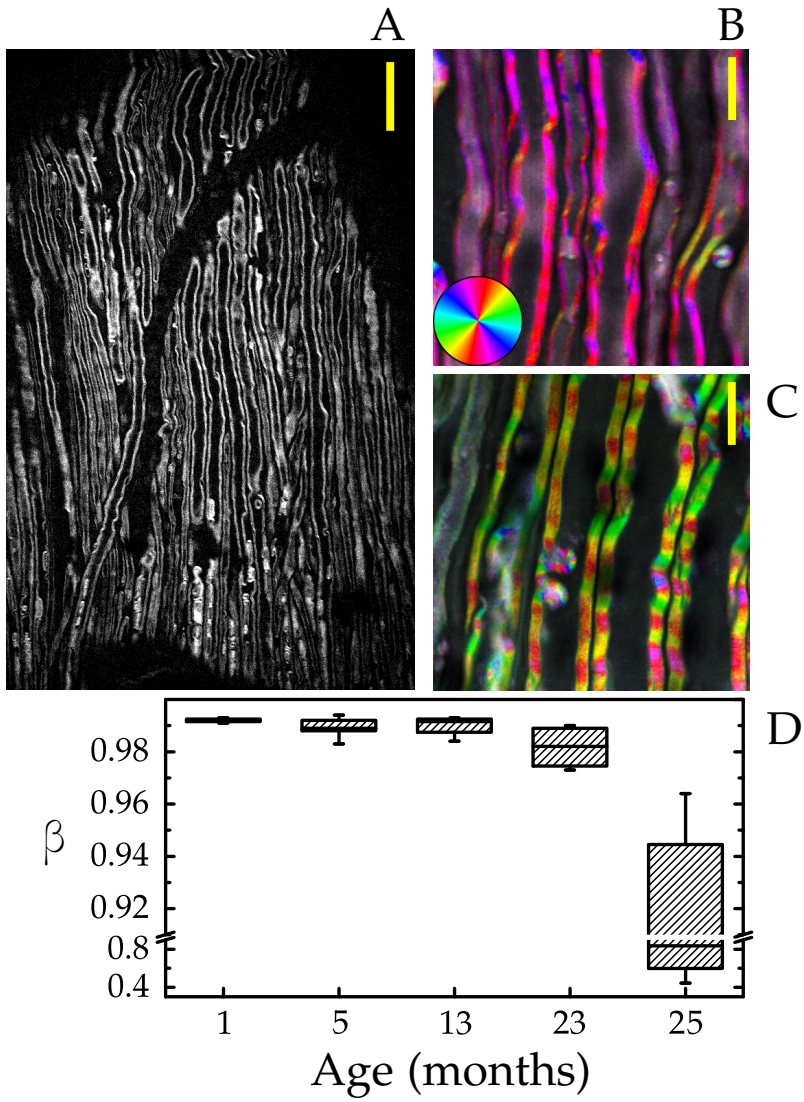

Figure 3.14: RP-CARS analysis of ageing sciatic nerves. (*A*): Representative large-scale CARS image (CH_2 bonds) of a longitudinal optical section of sciatic nerve from a 1-month old mouse. Scale bar: 40 μm. (*B*): Colour-coded RP-CARS image of a 1-month-old-mouse sciatic nerve. The image was constructed in the HSV colour space, by mapping the ϕ signal onto the Hue channel, the $A_{2\omega}$ signal onto the Saturation channel and the A_{dc} signal onto the Value channel. Colours indicate different average orientations of the CH_2 bonds, as depicted in the colour wheel. Scale bar: 10 μm. (*C*): Colour-coded RP-CARS image of a 25-month-old-mouse sciatic nerve. Colours and scale bar as in Panel (*B*). (*D*): Analysis of the average resultant length (β) as a function of mouse age.

ity" in the myelinated nervous fibres in older animals. I argue that this observed varicosity could be one of the causes, along with possible subtle abnormalities in the myelin composition and/or in the axon ionic channel expression and modulation, at the basis of the decrease, measured by collaborators [286], in the caudal and digital nerve conduction velocity for corresponding-age mice.

Biological sample preparation and data analysis

Unfixed sciatic nerves of WT mice (C57BL/6) were frozen at $-80\,^{\circ}\mathrm{C}$ immediately after the explant and kept at this temperature until the observation. The thawed tissue was put in the central well of a PBS-filled WillCo dish (GWSt-3512, WillCo Wells) and kept immobilised with a custom-made electrophysiology-type anchor. I observed a total of 5 nerves, belonging to animals aged 1, 5, 13, 23 and 25 months. From each nerve I acquired 4-to-5 z-stacks in different positions along the nerve.

Custom-made Python software (Python Software Foundation, Beaverton, Oregon, U.S.A.) was used to analyse the RP-CARS data. The program is reported as Listing 3 in Appendix A. The software first selects the image areas corresponding to myelin using a threshold value and then refines this selection by closing the binary mask [287]. The threshold value is chosen to be the 90^{th} percentile of the A_{dc} signal, computed individually from each z-stack. This percentile value was found to be the most appropriate for the thresholding procedure after manual inspection of the generated masks for all the z-stacks, but I verified that consistent changes of the percentile value do not significantly change the final results.

The software divides each masked image of each z-stack into squared sub-images corresponding to $15\ \mu\mathrm{m} \times 15\ \mu\mathrm{m}$ in size. This particular size was chosen because I found that over this spatial scale the fibre-orientation features are well defined. However I verified that varying the size up to $\pm 50\%$ does not significantly change the final results. For each sub-image the software computes the resultant length β for the ϕ values of the (N) thresholded pixels, commonly defined as:

$$\beta = \left| \frac{1}{N} \sum_{j=1}^{N} e^{i\phi_j} \right|^2 , \tag{3.8}$$

i.e. one minus the angular variance [288]. Finally, the software computes for each z-stack the weighted mean of the resultant lengths from all its sub-images, using the number of masked pixels present in each sub-image as weight.

All the statistical computations were performed with R software (R Foundation, Vienna, Austria [264]). The stack-based resultant lengths were averaged to obtain animal-based values and then these values were correlated with the animal age using the Spearman's rank correlation coefficient.

4 SIMULATIONS

In this chapter I shall set out the results that I obtained during my six-month stay at the University of California-Irvine. In particular, I modified a pre-existing custom-made simulation software application to adapt it to RP-CARS-imaging simulation. By exploiting this numerical simulation approach, I shall show that the α value is indeed a ratiometric and quantitative indicator and that it is only minimally affected by optical scattering and by implementation-specific settings, despite large variations induced in the absolute value of the CARS signal.

4.1 INTRODUCTION

During my six-month stay at the University of California-Irvine I worked on the development of a simulation software application to study the effects of the presence of light-scattering particles on PR CARS imaging. In this chapter I shall report on the main results concerning in particular RP-CARS imaging.

My work started by my modifying a pre-existing custom-made simulation software application written in the C++ programming language. The aim of this software is to simulate the distorting effects of one or more scattering particles on the detected CARS signal. A previous version of this software, including only linear-optics effects, was presented in a recent publication [289]. The method presented in this article is based on the Huygens-Fresnel (HF) principle and it is named HF Wave-based Electric Field Superposition (HF-WEFS) and is graphically represented in Fig. 4.1. In this approach, the objective-lens surface is modelled as a spherical surface with a radius corresponding to the focal length and a size defined by the NA. The incoming light is modelled as a plane wave that is coerced into a converging spherical wave by the lens. According to the HF principle, the focused wave is represented by a series of spherical waves generated by a grid of equally spaced point sources resting on the lens spherical surface. Each of these HF spherical waves is approximated by the software as a summation of HF plane wavelets propagating outward from each source with the same initial amplitude and phase [290, 291]. The software then exploits a ray-tracing algorithm to select only the plane wavelets that are effectively directed toward the detector (after passing through a condenser lens)

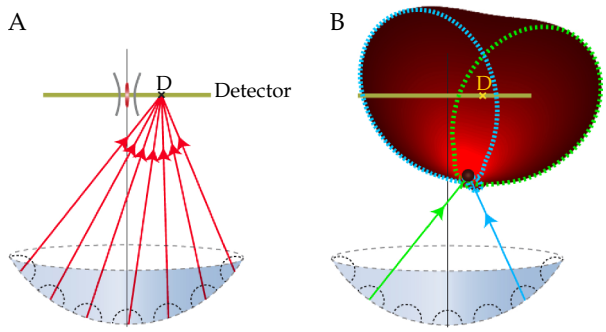

Figure 4.1: HF plane wavelets in nonscattering *(A)* and scattering *(B)* media. The spherical surface produces a series of forward-propagating HF spherical waves shown as dashed semicircles. In non-scattering media, each HF plane wavelet provides a partial electrical field at point D. In media containing scatterers, an HF plane wavelet incident upon a particle produces a complete 3D scattered field. The contribution from each scattered field provides a partial scattered electrical field at D. Dashed lines show the boundaries of the scattered field (blue and green). The superposition of the scattered fields gives the total scattered field. Only two HF plane wavelets are shown in *(B)* for clarity. Figure and legend text reproduced with permission from: J. C. Ranasinghesagara, C. K. Hayakawa, M. A. Davis, A. K. Dunn, E. O. Potma and V. Venugopalan, "Rapid computation of the amplitude and phase of tightly focused optical fields distorted by scattering particles," *Journal of the Optical Society of America A*, vol. 31, pp. 1520-1530, 2014 [289]. Copyright the Optical Society of America.

or towards the simulated scattering particle. Scattering particles are treated as spherical objects having a different refractive index with respect to the medium, and the scattering computations are carried out according to the Lorenz-Mie theory [292]. After this step, the ray-tracing algorithm again selects the plane wavelets directed towards the detector or towards a second scattering particle and, in the second case, the operation is repeated. Finally, the software computes the electrical field at the detector plane created by the interaction of all the plane wavelets that reached it.

As detailed in Ref. [289], the HF-WEFS method is several orders of magnitude faster than the finite-difference time-domain method [293] (considered the gold-standard numerical method for solving Maxwell's equations), while preserving at the same time the wave properties of the tightly focused incident beams and providing accurate focal-field predictions in the presence of single or multiple spherical scattering particles.

4.2 CODE DEVELOPMENT

Starting from the situation described in Section 4.1 and in Ref. [289], which was limited to linear optics, the authors modified the software in order to simulate the

CARS optical process. Moreover, on my arrival I collaborated with the authors in the implementation of a light-polarisation control system in the simulation algorithm. Then I autonomously implemented a sample-definition system in order to address heterogeneous optical samples (i.e. with 3D spatially-varying third-order susceptibility tensors). In continuity with the focus of my Ph.D. work, I decided to simulate myelinated nervous fibres and to study the optical effects of the presence of a spherical scattering particle placed between the fibre and the objective, as depicted in Fig. 4.2A. In this kind of simulation different sample voxels must be associated with different tensors according to the local composition of the sample and the tensors must be rotated depending on the orientation of the molecules in each voxel. This is depicted in Fig. 4.2B, which shows a schematic of a transverse section of a simulated myelinated fibre. The myelin-associated third-order susceptibility tensors must be rotated by the angle Θ, relative to the nervous fibre centre, in order to take into account the different orientation of the acyl chains (always perpendicular to the fibre surface).

Finally, I wrote a Python wrapping script that sequentially calls the simulation binary program with different input parameters making it possible to simulate an entire 3D imaging acquisition from the original code that can calculate the signal from only one sample point. A simulated line scan across the myelin wall along the x-axis, as defined in Figs. 4.2A and 4.2B, is obtained by repetitively running the simulation while sequentially translating the simulated optical sample given as input as schematically shown in Fig. 4.2C.

I simulated both a large-diameter myelinated fibre (described in Fig. 4.3A) and a small-diameter one (described in Fig. 4.3B). The fibre sizes, shown in the Figure, were chosen to match those of fibres commonly found in rodent large peripheral nerves and brain white-matter tracts [294, 295]. The third-order-susceptibility tensor was set according to the values that I measured in fresh sciatic-nerve myelinated fibres, reported in Section 2.1.4.

Finally, the size (1 μm) and the refractive index (1.49) of the scattering particle were set according to those of the lipid droplets observed inside the neurons [296], while the refractive index of the medium was set to 1.333. The simulated focal plane was set to coincide with the equatorial longitudinal plane of the nervous fibre and the scattering particle was placed centred with respect to the myelin wall thickness and below the fibre (3.8 μm below the focal plane in the first case and 1.5 μm below in the second case), being almost in contact with the myelin wall, as depicted in Fig. 4.3.

All the settings in the simulation were chosen to reflect the real CARS setup described in Section 2.2. In particular: the NAs of the objective and of the condenser were set to 0.85 and 0.55, respectively; the working distance of the objective was set to 1.1 mm and the simulated incoming light beams were configured as a 810 nm

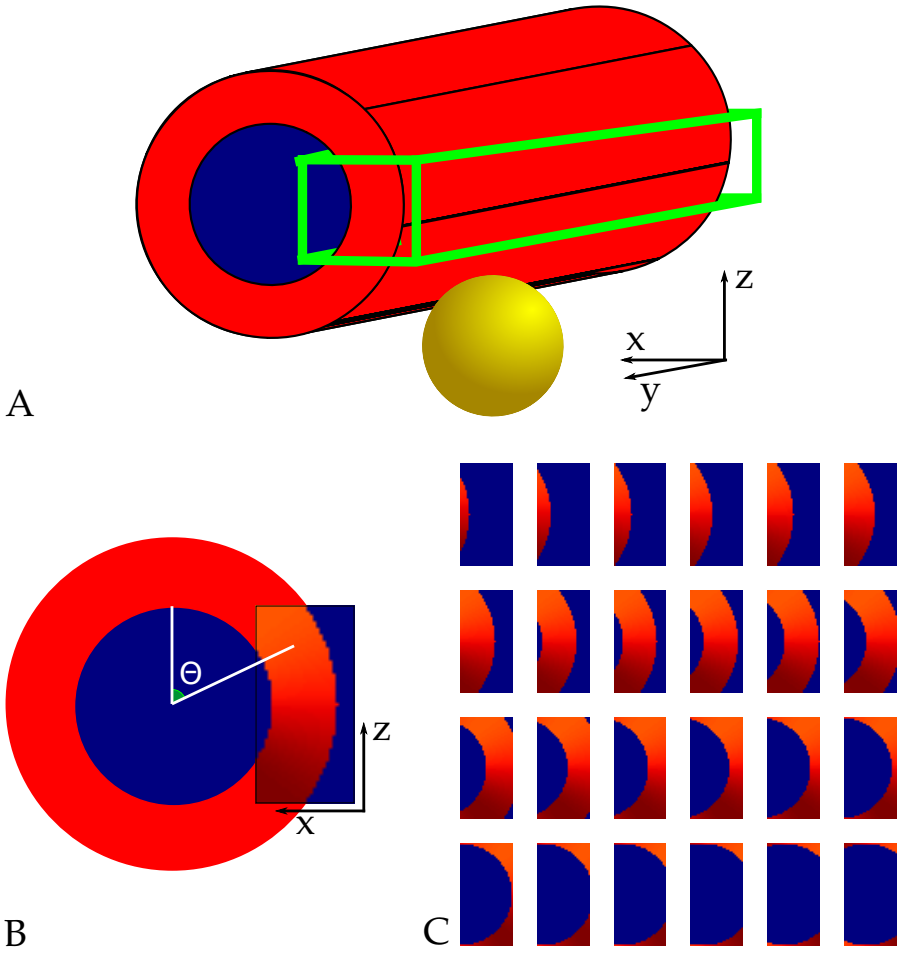

Figure 4.2: Schematics of the simulated samples. *A*: Graphical representation of the myelin wall (in red), the scattering particle (in gold), the fibre lumen (in blue) and the simulated imaging volume (green box). This colour scheme will also be used in the following images. The fibre axis is oriented along the y-axis. *B*: The simulated myelin voxels are associated with a third-order susceptibility tensor that is spatially oriented according to the angle Θ, as shown in the Figure. The black-bordered box highlights a transverse section (onto the xz-plane) of the simulated imaging volume. *C*: Series of transverse sections (onto the xz-plane) of the simulated imaging volume. The panels in the series are arranged along the x-axis of the simulated sample: from the border of the fibre toward its centre, this is equivalent of scanning a transversal line across the fibre myelin wall. The myelin-wall size is specified in Fig. 4.3A.

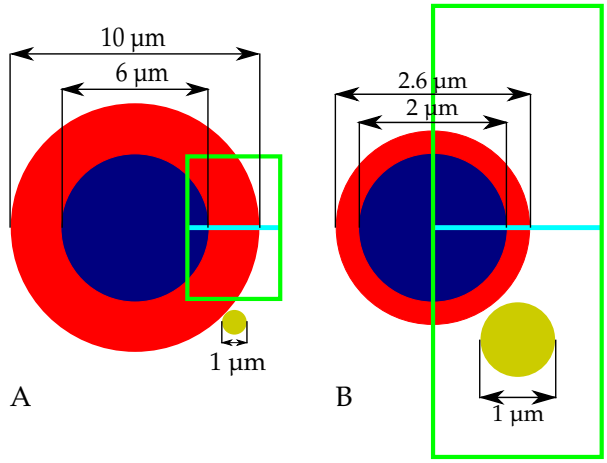

Figure 4.3: Sizes of the simulated myelinated fibres and the scattering particle. I simulated both a large-diameter fibre (*A*), frequently observed in large peripheral nerves, and a small-diameter fibre (*B*), often observed in the brain white matter tracts. The colour scheme is the same as in Fig. 4.2. The size of the simulated imaging volumes (green boxes) and the relative positions of all the represented objects are depicted in exact scale. The imaging planes (corresponding to the fibre equatorial planes) are shown in cyan.

linearly-polarised pump beam (with a rotating polarisation plane) and a 1060 nm circularly-polarised Stokes beam. However, all the simulations were also replicated for consistency using a linearly-polarised Stokes beam.

4.3 RESULTS

I first studied the optical effects of the scattering particle on the RP-CARS imaging of the large-diameter fibre. As shown in Fig. 4.4, the presence of the scattering particle induces a significant decrease in the CARS signal intensity (more than 5%), both when using a pump beam polarised along the CH_2 bonds (on the imaging plane) and when using a perpendicular polarisation. Interestingly, the induced alteration in α was found to be around 5 times smaller (around 1%) and therefore negligible. This result is in agreement with the experimental measurements described in Section 3.3.2 and depicted in Fig. 3.11, showing that the optical scattering (due to different depths of the focal plane inside the tissue) has a negligible effect on the computed α value.

It is worth noting that, while the maximum attenuation of the CARS signal is coincident with the vertical projection (along the z-axis, as defined in Fig. 4.2A) of

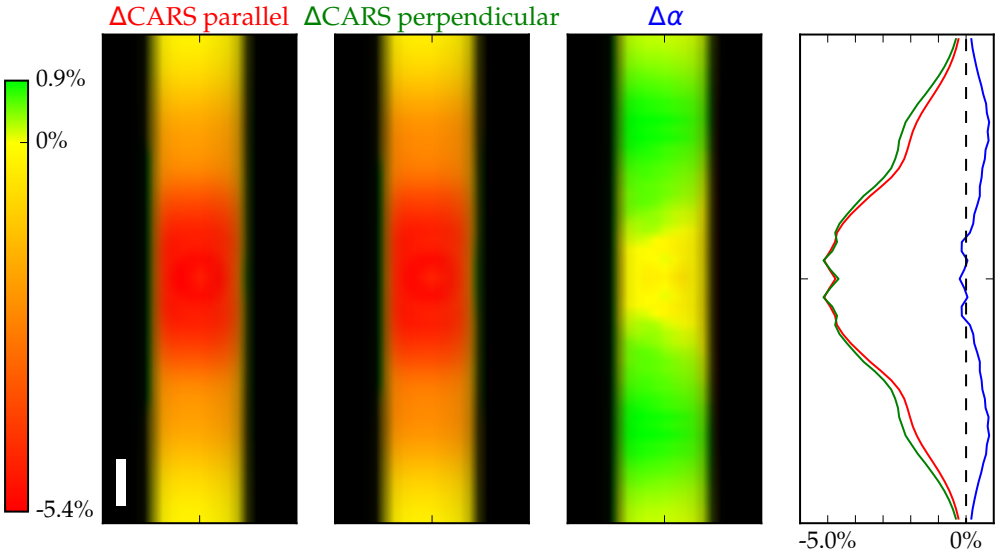

Figure 4.4: Simulated imaging of the large-diameter myelinated fibre described in Fig. 4.3A. This Figure represents a simulated optical section along the equatorial xy-plane of a single myelin wall with a simulated scattering particle placed 3.8 μm below the imaging plane and centred with respect to the image (as show in Fig. 4.3A). The first and the second panels on the left depict the percentage variation of the CARS signal intensity (with respect to the situation where no scattering particle is present) when using parallel- or perpendicular- polarised pump beam, respectively (while keeping the Stokes beam circularly polarised). The third panel similarly depicts the percentage variation of the α value. The colour scale is shown on the left (from red, set to the displayed minimum value, to green, set to the displayed maximum value, keeping yellow at 0) while the pixel intensity is a function of the simulated A_{dc} signal. Scale bar: 1 μm. The rightmost panel shows profiles along the central line of the myelin wall (along the y-axis) of the quantities depicted in the first three panels, as explained by the title colours.

the scattering particle position, in the same position the α value experiences almost no distortion. On the contrary, the effect on the α value is maximum at the sides of the vertical projection of the scattering particle position. This observation is in agreement with what was previously reported for linear optics in Ref. [289] regarding the distorting effect of spherical scattering particles. In the cited article it is shown that, when the scattering particle position is off from the optical axis, the scattered field is oblique. In this situation the constructive interference between the incident and scattered fields produces strong alterations of the beam-intensity profile in the focal plane.

I then repeated the simulation on the small-diameter fibre. The results are displayed in Fig. 4.5. In this case the attenuation of the CARS signal is even more pronounced, being more than 20% for both polarisations. Nonetheless, the alteration of the α value is 4 times smaller: around 6%.

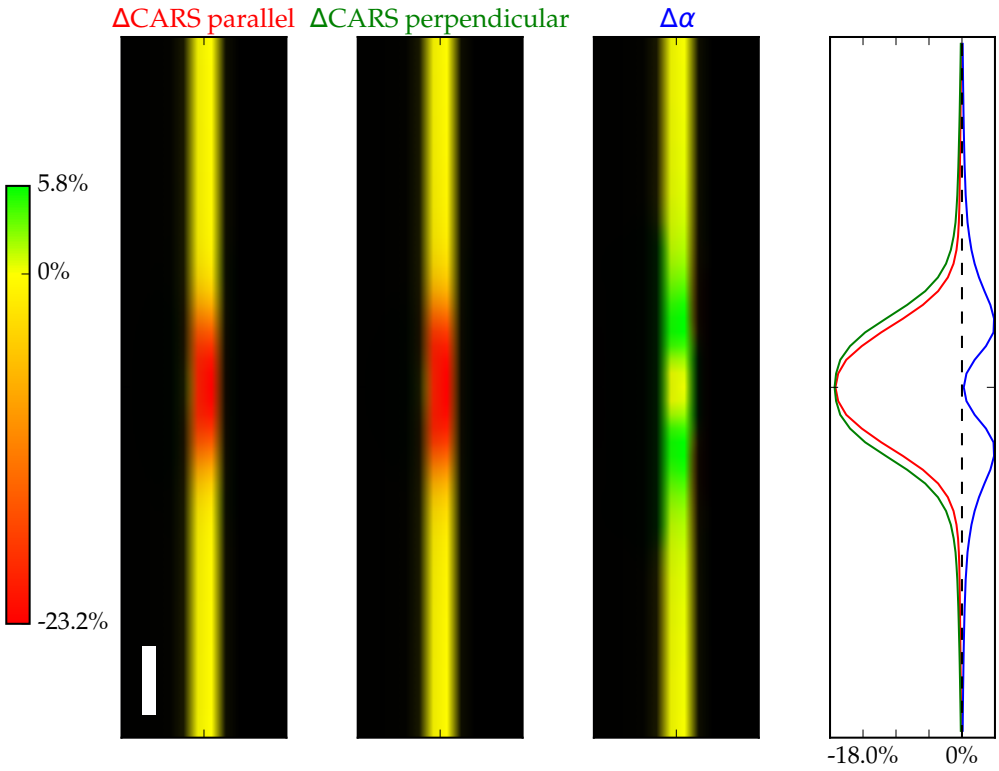

Figure 4.5: This Figure is constructed as Fig. 4.4 but it refers to the small-diameter myelinated fibre described in Fig. 4.3B. This Figure represents a section along the equatorial xy-plane of a single myelin wall with a simulated scattering particle placed 1.5 μm below the imaging plane and centred with respect to the image (as show in Fig. 4.3B). Scale bar: 1 μm.

In this case, too, the effects on the CARS signals and on the α value display the same spatial pattern as in the case of the large-diameter fibre. In addition, it is worth noting that, in both the cases, while the CARS signal intensity is decreased, the α value instead slightly increases. This means that the A_{dc} signal decreases slightly more than the $A_{2\omega}$ signal.

In order to check the consistency of the results, I verified that using a smaller scattering particle (0.5 μm diameter) placed in the same position below the small-diameter fibre induces smaller distorting effects on the CARS intensity and on the α value, as expected.

The simulations performed on the large-diameter fibre and on the small-diameter fibre were repeated using a linearly-polarised Stokes beam (kept parallel to the rotating linearly-polarised pump beam), instead of a circularly-polarised one. From

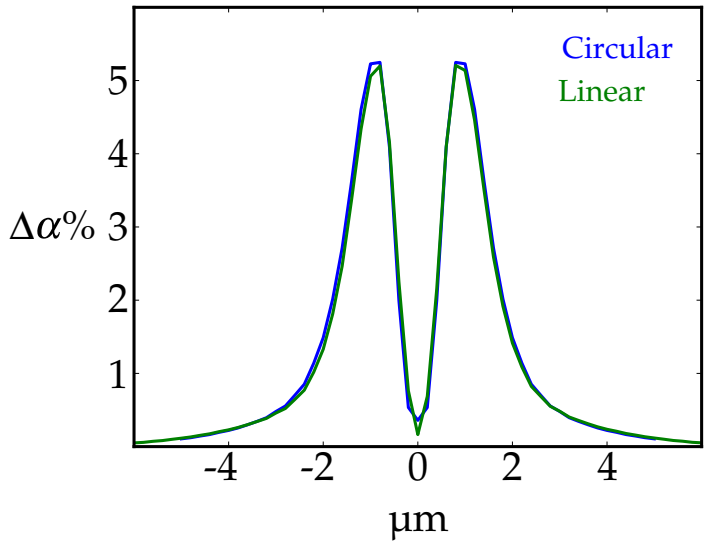

Figure 4.6: Comparison of the distorting effects induced by the presence of the scattering particle on the α value (expressed as percentage difference with respect to the situation where no particle is present) when linear or circular polarisation is employed for the Stokes beam (while keeping the pump beam linearly polarised). I simulated the sample described in Fig. 4.3B and represented in Fig. 4.5. The graph shows the average signal along the whole thickness of the myelin wall (i.e. along the x-axis, as defined in Fig. 4.2) as a function of the distance along the y-axis from the projection of the scattering particle position.

the experimental point-of-view, this approach leads to larger detected signal and therefore it could be, in principle, more robust against noise. However, a drawback is constituted by a number of technical difficulties in the practical implementation of a pair of linearly-polarised beams with different wavelengths whose polarisation planes rotate perfectly in phase, as discussed in Section 2.1.2. Nonetheless, these simulations investigate the possibility of implementing a different version of the RP-CARS technique and were performed to study the robustness of this variant against the scattering effects. The obtained results, translated into relative measures (i.e. ΔCARS% and $\Delta\alpha$%), are very similar to the first ones, as shown in Fig. 4.6. This Figure shows the percentage variation in the computed α value induced by the presence of the scattering particle on the small-diameter fibre (described in Fig. 4.3B and displayed in Fig. 4.5) when linear or circular polarisation is employed for the Stokes beam. Unlike the last panel on the right of Fig. 4.5, here the difference is averaged over the myelin wall thickness (i.e. along the x-axis, as defined in Fig. 4.2).

In principle, the use of a high-NA objective may enhance polarisation inaccuracies, making the RP-CARS method less effective. I have already discussed this issue in Section 2.2.3, pointing out several qualitative reasons why this effect should be

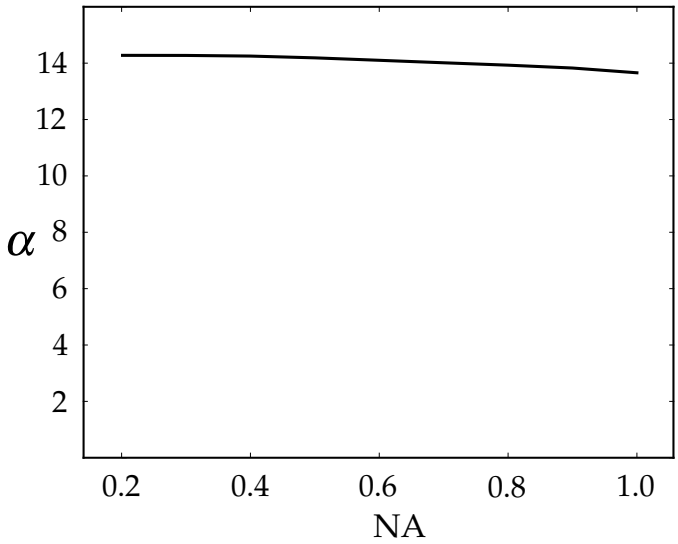

Figure 4.7: Effect of the objective NA (defined in air) on the computed α value. I simulated a full volume of myelin whose acyl chains were oriented coplanar with respect to the focal plane.

considered negligible. To quantify this effect, I performed a simulation to study the effect of the objective NA on the computed α value. The results are shown in Fig. 4.7. In this case, in order to rule out possible effects induced by the size of the optical excitation volume, the chosen simulated sample was a uniform volume of myelin whose acyl chains were oriented coplanar with respect to the focal plane. As the Figure shows, the effect of the objective NA (defined in air) on the retrieved α value was very small, since a factor-of-5 change in the NA only produced a difference in the α value of around the 4.4%.

4.4 CONCLUSIONS

In conclusion, by exploiting a numerical-simulation approach, I showed that the α value is a robust ratiometric and quantitative indicator, since it is only minimally affected by the optical scattering and by implementation-specific settings such as the objective NA and the polarisation configuration. This remains true despite the large variations induced in the absolute value of the CARS signal. Finally, the presented results are additional proof of the power and the versatility of the HF-WEFS simulation principle.

5 OTHER APPLICATIONS

CARS-microscopy setups, thanks to their intrinsic multimodal nature, are extremely effective in observing the interactions of nanostructures with biological materials. In this chapter I shall report on the investigation of these interactions; in particular, I have demonstrated the internalisation of different kinds of non-centrosymmetric nanoparticles (boron-nitride nanotubes, barium-titanate nanoparticles and barium-titanate-core/gold-shell nanoparticles) by cultured cells taking advantage of their non-linear optical properties leading to emission of SFG/SHG signals. Also, I exploited my multimodal microscope to assess the presence of barium-titanate nanoparticles within a 3D-printed Ormocomp structure in view of the realization of active osteogenic scaffolds.

5.1 INTERNALISATION OF BORON NITRIDE NANOTUBES

Boron nitride nanotubes (BNNTs) are tubular nanostructures with sub-micrometre diameters and micrometre lengths. They are composed of seamless cylindrical rolls of hexagonal-phase boron-nitride sheets [297, 298].

Their peculiar properties, including exceptional stiffness, good chemical stability and high thermal conductivity [299], make them ideal candidates for a broad range of applications [300]. BNNTs have received much interest in recent years, partly for their exploitation in nanomedicine as tools for drug delivery [301] and as intracellular nano-transductors [302]. Nevertheless, the biocompatibility of these structures is still being debated, with some authors reporting BNNTs as safe nanomaterials [301–308] and others pointing out their toxicity, in particular of ultrapure and long (~10 nm) BNNTs [309]. An inspection of the cited articles suggested that the differences in toxicity could stem from the aspect ratio of the tubes: as for other fibrous material, higher-aspect-ratio BNNTs seemed to be associated to a decreased biocompatibility.

In order to test this hypothesis, the BNNTs described in Ref. [309] were shortened down to 1.5 nm with a homogenization/sonication treatment that allows for their dispersion in gum-Arabic aqueous solutions [310]. The obtained BNNTs were thereafter tested on two human cell lines: neuroblastoma cells (SH-SY5Y) and human umbilical vein endothelial cells (HUVECs), with several independent biocompatibil-

ity assays and exploiting both biochemical and imaging methods. This work showed no toxic effects in the same concentration range that was tested in Ref. [309], thus confirming the biosafety of BNNTs and highlighting again that nanoparticle aspect ratio plays a key role in the biocompatibility evaluation.

I contributed to this work by assessing the cellular uptake of the nanotubes by the SH-SY5Y cells. To this end, I exploited the multimodality of the CARS setup: I was able to obtain three-dimensional images of the cells by taking advantage of the CARS signal emitted by their CH_2 bonds. At the same time, the non-centrosymmetric structure of BNNTs that leads to strong SHG and SFG signals (in addition to FWM emission) allowed me to image and locate them within cells.

Figure 5.1 depicts a result of the cellular internalisation assessment: it shows a single slice from a z-stack acquisition, along a side projection, of cultured cells incubated for 24 h with 20 μg/ml of BNNTs. A visual inspection of the Figure confirms the presence of BNNTs inside the cells. Figure 5.1, as well as the other figures shown in this Chapter, is constructed in the Red, Green, Blue (RGB) colour space, where the CARS/FWM signal (emitted around 650 nm) and the SFG signal (emitted around 460 nm) are mapped onto the green channel and the red channel respectively, whereas the blue channel is set to zero.

5.2 INTERNALISATION OF BARIUM–TITANATE NANOPARTICLES

Barium Titanate Nanoparticles (BTNPs) belong to a class of ferroelectric materials showing high piezoelectricity [311]. They demonstrate high cytocompatibility [202], excellent properties as nonlinear imaging probes [312] (an example of their multimodal spectrum is shown in Fig. 2.2) and the ability to deliver doxorubicin in cancer cells by improving drug uptake [313]. Moreover, BTNPs were proven to enhance the osteogenic differentiation of mesenchymal stem cells (MSCs), as demonstrated by an increment of hydroxyapatite deposition [314].

The ability of MSCs to differentiate into osteoblasts is well known, but the osteogenic potential of MSCs decreases with the prolonged culture duration necessary to obtain an appropriate number of cells for clinical applications [315]. For this reason, there is great interest in methods able to foster osteogenesis in MSCs and also to this end several nanomaterials were proposed as possible solutions [316–318].

Physical cues can also influence cell differentiation [319] and proliferation [320]. Among these, gravity is required for the correct development of land-based organisms, and in particular for the skeleton, for the muscles, and for the nervous systems [321]. Bone growth is particularly affected by altered gravity conditions: evidence re-

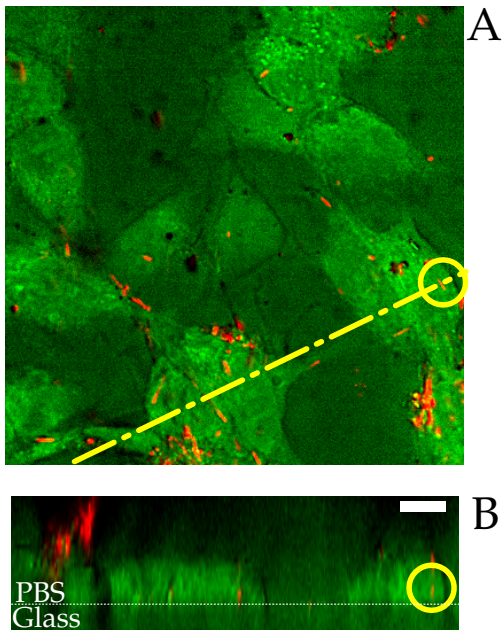

Figure 5.1: Multimodal image of SH-SY5Y cells treated for 24 h with 20 µg/ml BNNTs. Green: CARS signal from CH_2 bonds and FWM signal from the sample (including BNNTs), red: SFG signal from BNNTs. (*A*): Optical section in the cells plane. The dark spots are the shadows of BNNTs below or above the imaging plane. (*B*): Virtual section along the dashed yellow line indicated in (*A*) and perpendicular to the focal plane. The WillCo-dish glass surface is indicated by a white dotted line. The yellow circle highlights the same single BNNT in (*A*) and (*B*). Scale bar: 10 µm.

garding bone regeneration suggests that hyper-gravity exposure – conversely with regard to micro-gravity, which negatively affects osteogenesis – may enhance the osteogenic potential of osteoblast precursors [322].

Based on these premises, we investigated the combined effects of hyper-gravity and BTNPs on the osteogenic differentiation of rat MSCs and the hyper-gravity effects on nanoparticle internalisation [203]. To obtain the hyper-gravity condition, a large-diameter centrifuge was used in the presence of a BTNP-doped culture medium. Cell morphology and nanoparticle internalisation were analysed with imaging methods, while cell differentiation was evaluated with molecular-biology methods. Following a 20-g treatment, alterations in cytoskeleton conformation, cellular shape and morphology were found, as well as a significant increment of osteoblastic marker expression both at gene and protein levels together with a substantial increment of nanoparticle uptake. Taken together, these findings suggest a synergistic effect of hyper-gravity and BTNPs in the enhancement of the osteogenic differentiation of MSCs. This result holds promise for the design of new approaches in bone-tissue engineering, as well as for *in-vitro* drug-delivery strategies where an increment of nanocarrier internalisation could result in a higher drug uptake by the cells.

I contributed to this work by visualising the cellular uptake of the BTNPs by the MSCs cells exposed to different experimental conditions. Results of multimodal imaging on proliferating and differentiating cells internalising BTNPs at 1-g and 20-g are reported in Fig. 5.2. The image is constructed by mapping SFG (from BTNPs) and CARS/FWM signals as Fig. 5.1. Figure 5.2A depicts images representative of the four experimental conditions, highlighting a perinuclear cytoplasmic accumulation of BTNPs. A quantitative evaluation of BTNP uptake (Fig. 5.2B), performed by another experimenter in terms of percentage of the cytoplasmic area occupied by the BTNPs, revealed a strong enhancement of BTNP internalisation in cells that underwent hyper-gravity stimulation ($p<0.05$), both in differentiation ($6.8 \pm 0.8\%$ at 20-g, $3.6 \pm 0.3\%$ at 1-g) and in proliferation ($2.7 \pm 0.3\%$ at 20-g, $1.4 \pm 0.1\%$ at 1-g) conditions (Kruskal-Wallis test with Nemenyi-Damico-Wolfe-Dunn post-hoc tests). The generally higher internalisation in differentiation conditions was simply due to a longer BTNP incubation time ($3 + 48$ hours for differentiation samples versus 3 hours for proliferation samples).

In addition, I have exploited these nanoparticles to measure the PSF of the microscope, estimated to be about one third of the micron in the imaging plane.

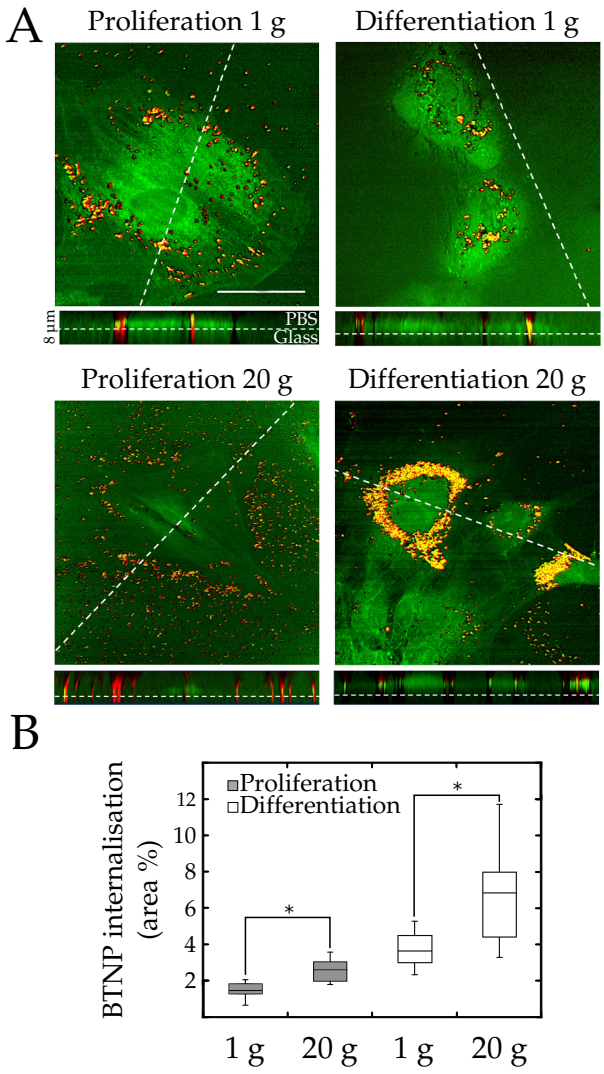

Figure 5.2: (*A*): Multimodal images showing BTNP internalisation inside the cells. The CARS/FWM signal from the CH_2 bonds and from the BTNPs is mapped on the green channel while the SFG signal from the BTNPs is mapped on the red channel. The bottom panels show transverse sections along the dashed lines shown in the top panels. The glass/solution interfaces are indicated by the dashed lines. The displayed images are representative of the experimental conditions: cell proliferation versus osteogenic differentiation and normal gravity ("1 g") versus hyper-gravity stimulation ("20 g"). Scale bar: 50 µm. (*B*): Box-plot quantification of BTNP internalisation as percentage of the area occupied by the BTNPs in the four different experimental conditions. The statistically significant differences ($p<0.05$) are marked with an asterisk (*).

5.3 INTERNALISATION OF BARIUM–TITANATE–CORE/GOLD–SHELL NANOPARTICLES

Nanoshells are spherical nanoparticles consisting of a dielectric core covered by a thin metallic shell. The core/shell approach allows for the tuning of the plasmon band [323] throughout the visible and into the infrared region of the electromagnetic spectrum [324–326], simply by changing the thickness of the shell, while offering huge flexibility in terms of a variety of physical, chemical and optical characteristics by appropriately choosing the core material.

These nanoparticles are exploited as contrast agents whose optical properties can be tuned across a broad range of wavelengths in comparison to conventional molecular contrast agents [327, 328]. Moreover, they are biocompatible and non-photobleaching [329], and have been employed in various imaging modalities [329, 330]. The enhanced optical absorption at the plasmon wavelength makes core/shell structures ideal nanoscale heat sources. To this end, they are currently being studied at the preclinical level for cancer photothermal therapy *in-vitro* [331, 332] and *in-vivo* [333, 334] and as absorbers for tissue welding [335, 336].

Cancer hyperthermia therapy entails heating the neoplastic tissue to a temperature of 42 °C - 47 °C for some tens of minutes [337], leading to irreversible damage for the cancerous cells, which may undergo either necrotic or apoptotic death [338–341]. In fact, there is mounting evidence of the clinical potential of hyperthermia therapy when employed with conventional cancer therapy methods to achieve more effective results [340]. Finally, a recent evolution of hyperthermia therapy has emerged, named photothermal therapy. Here, the exogenous photothermal agents absorb the incident laser energy and act as nanoscale heaters in order to achieve selective destruction of cancer cells in a noninvasive, high-precision fashion. From proof-of-concept studies [333, 342–345], this approach is rapidly moving towards clinical application [346].

Following this line, Farrokhtakin and collaborators reported the synthesis of barium titanate core-gold shell nanoparticles ($BaTiO_3$@goldshells) in a recent article [220] and subsequently we demonstrated their potential in cancer photothermal therapy [219]. An SEM image of $BaTiO_3$@goldshells is shown in Fig. 2.11. The motivation for selecting barium titanate as the core of the nanoshells stems from recent results on the application of piezoelectric materials in biology [302], in order to study further the potential resulting from merging piezoelectric and plasmonic properties.

In this article we explored the effect of increasing concentrations of $BaTiO_3$@goldshells (0-100 μg/ml) on human neuroblastoma SH-SY5Y cells, testing their internalisation by cells and their intrinsic toxicity, aiming at validating the hyperthermic functionality of the particles through near-infrared laser-induced thermoablation ex-

periments. No significant changes were observed in cell viability up to nanoparticle concentrations of 50 μg/ml, demonstrating a reasonable cytocompatibility of the nanoparticles. Experiments upon stimulation with a near infrared laser revealed the ability of the $BaTiO_3$@goldshells to destroy human neuroblastoma cells, by acting as effective heat-inducing agents. On the basis of these findings, $BaTiO_3$@goldshells were seen to be suitable for photothermal treatment, and these results represent a promising first step towards subsequent investigations into their applicability in clinical practice.

I contributed to this work by visualising the cellular uptake of the $BaTiO_3$@goldshells by the SH-SY5Y cells exploiting the SFG emission from the nanoparticles.

5.4 IMAGING OF NANOCOMPOSITE SCAFFOLD

I also exploited the multimodal setup to visualise a nanocomposite piezoelectric structure build by two-photon polymerization of commercially-available Ormocomp doped with piezoelectric BTNPs (already described in Section 5.2).

Two-photon lithography is a disruptive technology that allows the fabrication of complex 3D nanostructured scaffolds, owing to the mechanism of two-photon absorption and polymerisation of dedicated photoresists [347]. Obtained 3D structures can be exploited as scaffolds for the investigation of cell/substrate biophysical interactions, for the promotion of a specific cell phenotype and for the modification of biomedical-device surfaces [348, 349].

The availability of several materials that can be exploited as photoresists for two-photon lithography allows control of a wide range of physical/chemical properties of the material (e.g. stiffness, porosity, roughness, biodegradability), which can be further tuned by doping the resists with appropriate nanomaterials, thus obtaining "smart" features not achievable by the use of the corresponding bulk material [350]. In the case of piezoelectric-nanomaterial doping, different cell types (including neurons [351], neural stem cells [352] and fibroblasts [353]) have been successfully stimulated by electric fields generated by piezoelectric nanoparticles/nanofibers upon exposure to ultrasounds [354].

In this context, Marino and collaborators have recently developed bioinspired 3D structures with a structure resembling that of spongy-bone trabeculae, named "Osteo-Prints". They demonstrated that these scaffolds are able to promote the osteogenic differentiation of SaOS-2 osteoblast-like cells (human osteosarcoma-derived cell line) through topographical stimulation [355]. More specifically, the enhanced osteogenesis was proven to be induced by the presence of the 3D biomimetic niches able to affect the cellular (and nuclear) shape and fostering cell commitment toward

osteogenesis. While for this work the authors exploited two-photon lithography to polymerise Ormocomp, in a more recent publication [204] we described the use the same technique to build Osteo-Prints made of Ormocomp doped with piezoelectric BTNPs, thus creating a novel piezoelectric nanocomposite material aimed at an increased enhancement of the osteogenic differentiation of SaOS-2 cells.

We used both imaging and spectroscopic methods to study the obtained structures. Moreover, preliminary *in-vitro* testing was performed, demonstrating that both the topographical and the piezoelectric cues of these scaffolds, together with mechanical stimulation provided by ultrasounds, are able to enhance the osteogenic differentiation of human SaOS-2 bone-like cells. These findings open new interesting perspectives in the field of regenerative medicine and bone-tissue engineering: as an example, the possibility to functionalise the surface of biomedical devices with biomimetic piezoelectric structures can potentially foster the osseointegration of the implants, by combining ultrasound-driven piezoelectric stimulation with a bioinspired topography.

My contribution to this work consisted of the visualisation of the nanoparticle distribution inside 3D structures by means of multimodal microscopy, taking advantage of the peculiar nonlinear optical properties of the BTNPs, already described in Section 5.2. These structures were fabricated as a test of the nanocomposite photoresist, and built by two-photon lithography.

I observed structures polymerised both without BTNPs (plain Ormocomp, Fig. 5.3A) and with 10 wt% BTNPs (Fig. 5.3B). These images are also constructed by mapping SFG (from BTNPs) and CARS/FWM signals as Fig. 5.1. The presence of the nanoparticles inside the structure was confirmed both by z-stack acquisitions (the virtual transverse section is visible at the bottom of Fig. 5.3B) and by the observation of SHG and SFG peaks in the spectrum of the light emitted by the structure internal volume (Fig. 5.3D). In the case of undoped structures, no SHG and SFG peaks were present in the spectra (Fig. 5.3C).

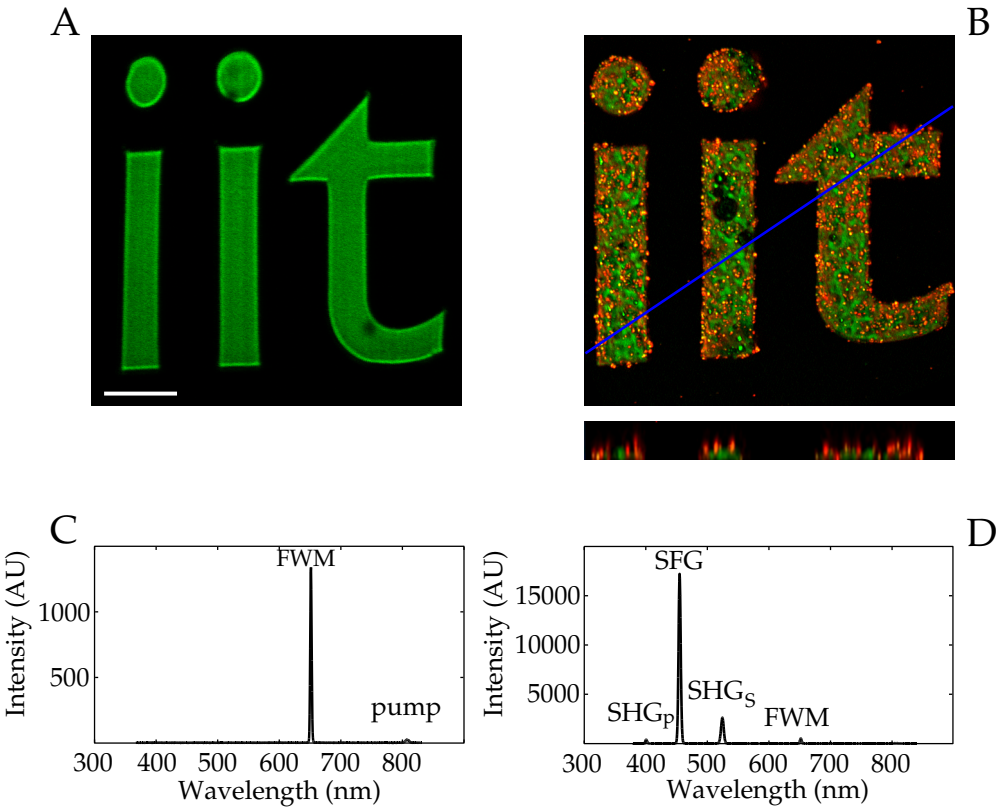

Figure 5.3: Multimodal imaging of the control structure (*A*), done with plain Ormocomp, and of the nanocomposite structure (*B*), done with Ormocomp doped with BTNPs. The FWM signal from the Ormocomp and the BTNPs is mapped on the green channel while the SFG signal from the BTNPs is mapped on the red channel. A virtual transverse section (made along the blue line) is shown at the bottom of (*B*). Scale bar: 100 μm. The emission spectra acquired from the control structure and from the nanocomposite structure are reported in (*C*) and (*D*), respectively.

6 CONCLUSIONS AND FUTURE DEVELOPMENTS

In this chapter I shall draw the conclusions of my work and propose some possible future developments of this field of research. In previous chapters I have shown the efficacy of RP-CARS as a research tool for the study of myelin molecular architecture; here I shall discuss its application to other relevant biological questions and point out the issues to address in order to foster its adoption as a clinical tool.

6.1 CONCLUSIONS

At the beginning of my Ph.D. course, I built a CARS microscopy setup in order to take advantage of polarisation-dependent selection rules to detect the local microscopic orientation of the chemical bonds under investigation: I named this new imaging modality RP-CARS microscopy. For this purpose, I dedicated particular attention to several technical aspects: the generation of the incoming beams, optimisation of the acquisition process, movements of the scanning mirrors, minimisation of the polarisation distortion and spectral focusing. With this state-of-the-art microscope I was able to visualize, in real-time and over a large area, the spatial anisotropy of the CH_2 bonds with sub-microscopic resolution and their in-plane average local orientation.

This label-free setup was expressly developed for the observation of myelin, since the methods currently employed for its visualisation require tissue staining (unlike CARS) and therefore their application in particular (e.g. clinical) settings is far from ideal. Moreover, the myelin molecular structure displays important symmetry characteristics that make it an extremely interesting sample for PR microscopical investigations.

After having validated the RP-CARS methodology with different samples of nervous tissue (brain slices and peripheral nerves), I used it to study an *ex-vivo* chemical-model of myelin damage. By exposing an explanted mouse sciatic nerve to a demyelinating agent, I demonstrated that with this technique it is possible to assess the myelin health status by measuring the intrinsic molecular architecture, relying on the fact that healthy myelin is characterised by a high degree of molecular order.

I then proceeded to apply this technique to the study of a murine genetic model of a human leukodystrophy: Krabbe disease. Thanks to RP-CARS I demonstrated a post-onset progressive decrease in the spatial orientation order of the CH_2 bonds inside the myelin walls of the afflicted mice sciatic nerve fibres. This result demonstrates that this label-free approach, potentially compatible with *in-vivo* settings, could be used to monitor the disease progression or its response to experimental treatments.

In addition, I exploited the RP-CARS technique to quantify the variability in the myelin sheath orientations of the mouse sciatic nerve on a micrometric spatial scale. I observed an increase in this variability with ageing and this observation can be interpreted as the onset of a "varicosity" in the myelinated nervous fibres in older animals.

In order to analyse the large amount of data collected by RP-CARS imaging, I developed a custom-made data analysis pipeline expressly devoted to the extraction of information from the complex multi-dimensional RP-CARS stacks.

Finally, I employed a numerical approach based on HF decomposition of focused beams to study the distortion effects induced by the scattering particles on the PR acquisitions. In particular, I first modified an existing research software application in order to simulate the RP-CARS technique and then I used it to demonstrate that this microscopy method is very robust against scattering, specifically in the case of myelin sheaths imaging.

Apart from the research activity concerning the neurobiological samples, I also exploited the multimodal imaging capacity of the setup to demonstrate the internalisation of several different kinds of nanoparticles by cultured cells and the nanopatterned nature of a structure built with two-photon lithography.

6.2 FUTURE DEVELOPMENTS

RP-CARS has reliably proven to be an extremely useful tool in scientific research, and I therefore expect its use in the investigation of the submicroscopic molecular structure of myelin to increase in the next few years. During my Ph.D. course I observed the PNS of TWI mouse: an interesting and still unanswered question is whether the same observed differences can also be confirmed in the CNS. Another interesting question concerns the observation that the baseline value of α displays a sample-specificity [207]. Although it is well known that the myelin composition varies with different parts of the body [144], with ageing [282] and with different species [142], the sample variability among conspecific age-matched individuals is not yet fully understood. For example, it would be interesting to test whether the

different genetic backgrounds of conspecific animals can be related to differences in the α baseline value since this variability could potentially affect the progression of myelin-associated pathological states. Moreover, it would also be of great interest to apply this technique to other myelin pathologies, such as multiple sclerosis, or to apply it to the study of different structures (other than myelin) of the animal or even the plant body, where an extensive symmetrical molecular structure exists.

It should be pointed out, however, that the experimental implementation of this technique still presents some technical difficulties and this can potentially hamper its wide adoption as a routine technique for biological research. In this regard it must be recognised that additional work is still needed in order to provide an easy-to-use setup implementation for the non-expert user.

Apart from the scientific applications, this technique possesses a breakthrough potential in clinical diagnostics. CARS multimodal microscopy is an extremely effective imaging method for human skin histopathology [356]: it was recently demonstrated that it is capable of providing a discriminative capacity similar to that of traditional staining-based clinical microscopy methods. However, unlike conventional hystopatology, CARS-based approaches can be performed without biopsy explant, since they do not need the staining procedure. Moreover, a CARS tomograph was recently developed explicitly for imaging in clinical environments [357, 358]. To this end, it was designed to be operated without the specific technical expertise associated with optical research laboratories. Nonetheless, these implementations are not experiencing the significant and rapid adoption in clinical settings that they deserve. In my opinion, the reason behind this might be that the currently used techniques are extremely well-tested and cost-effective: the reduced invasiveness and the lesser patient discomfort promised by this new technology are not able to justify this switchover, particularly when the costs associated with its introduction are taken into account. This is especially true in the case of skin-biopsy procedures, which are unlikely to cause long-term health problems. In particular, when biopsies are used for cancer diagnostics and patient life potentially depends on accurate and timely results, the employed methods must be conservative and privilege diagnosis effectiveness over other potential benefits.

In my opinion there is, however, another clinical field where CARS, and RP-CARS in particular, can be more easily adopted: nerve biopsies. As already discussed in Section 1.3.2, nerve biopsies are still required as a diagnostic method for particular (and not very frequent) cases of neuropathies, but they are nonetheless associated with potential long-term health problems [166]. In this contest, CARS and RP-CARS could be valuable tools, being able to visualize the myelinated nerve fibres *in-vivo* and to assess their health without damaging the nerve.

It should be pointed out that an optical access is still needed and therefore the nerve must be exposed prior to its visualisation. This can be considered as an initial

step in the application of this technology, because it would still have several benefits with respect to traditional methods (first of all the nerve would not need to be dissected). Nonetheless, to assure clinical adoption the associated benefits must be overwhelming and therefore an endoscopic approach will be needed in order to overcome the necessity of the nerve exposition. Indeed, there are already several proposed implementations of CARS endoscopy [359, 360], but, to the best of my knowledge, there are still no proposed PR CARS endoscopic techniques. An endoscopic implementation of RP-CARS would make it possible to completely supersede the current methods for assessing the health of peripheral nerves, bringing indisputable benefits for the patients.

A CODE

This Appendix contains the listings of the Python code used for the image processing and analysis.

Listing 1: Custom-made Python software application used to load the raw microscopy data and save them as tiff files.

```
#!/usr/bin/python

"""Load the raw microscopy data and save them as tiff files"""

#This program loads the raw microscopy data (ASCII .dat files)
#and same them as images (tiff files).
#Some images are generated for storing purposes and therefore
#the original information is completely preserved at the expenses of
#the readability, others are instead generated expressly
#to be visually appealing and conseguently some
#of the original information is loss.

#loading the necessary modules
import glob, sys, colorsys, tifffile,os
import numpy as np

#if saturation_max is true, then the colour saturation in the
#output images is set to maximum, otherwise it is a function
#of A2w (valid only with RP-CARS acquisitions)
saturation_max=True

#clipping settings as percentiles
#(they cause loss of information while increasing the visual appeal)
sat_value_up=1
sat_value_down=5
sat_sat_up=5
sat_sat_down=1
alpha_max=20
alpha_min=0
```

```
#input sanitisation, define the input folder parameter
cartella_input=os.path.abspath(sys.argv[1])+'/'
#if the output folder parameter is not specified,
#then use the input folder for output too
try:
  cartella_output=os.path.abspath(sys.argv[2])+'/'
except IndexError:
  cartella_output=cartella_input

#load the Adc files list
lista_file_dc=glob.glob(cartella_input+"*dc.dat")
numero_file=len(lista_file_dc)

#recognise if the input folder represents an RP-CARS acquisition
#or a traditional CARS acquisition and load the file lists accordingly
if numero_file==0:
  rp=False #traditional CARS acquisition
  lista_file_0=glob.glob(cartella_input+"*0.dat")
  lista_file_1=glob.glob(cartella_input+"*1.dat")
  lista_file_0.sort()
  lista_file_1.sort()
  numero_file=len(lista_file_0)
  shape=(np.loadtxt(lista_file_0[0])).shape
else:
  rp=True #RP-CARS acquisition
  lista_file_r2=glob.glob(cartella_input+"*R2w.dat")
  lista_file_p2=glob.glob(cartella_input+"*P2w.dat")
  lista_file_dc.sort()
  lista_file_r2.sort()
  lista_file_p2.sort()
  shape=(np.loadtxt(lista_file_dc[0])).shape

#this creates some dummy arrays
uni=np.ones((shape[0],shape[1],numero_file))
zeri=np.zeros((shape[0],shape[1],numero_file))
dc=zeri.copy()
dc0=zeri.copy()
dc1=zeri.copy()
r2=zeri.copy()
p2=zeri.copy()

if rp: #load input data if RP-CARS acquisition
  for file_index in range(numero_file):
```

```
    dc[...,file_index]=np.rot90(np.loadtxt(lista_file_dc[file_index]))
    r2[...,file_index]=np.rot90(np.loadtxt(lista_file_r2[file_index]))
    p2[...,file_index]=np.rot90(np.loadtxt(lista_file_p2[file_index])*np.pi/180)
else: #load input data if traditional CARS acquisition
  for file_index in range(numero_file):
    dc0[...,file_index]=np.rot90(np.loadtxt(lista_file_0[file_index]))
    dc1[...,file_index]=np.rot90(np.loadtxt(lista_file_1[file_index]))

#this function performs the clipping of the input signal (segnale)
#according to the parameters: "sat_up" and "sat_down"
def clipping(segnale,sat_up,sat_down):
  mag=np.array(segnale).copy()
  mag_max=np.percentile(mag,100-sat_up)
  mag_min=np.percentile(mag,sat_down)
  mag[mag>mag_max]=mag_max
  mag[mag<mag_min]=mag_min
  if (mag_max-mag_min)!=0:
    mag=(mag-mag_min)/(mag_max-mag_min)
  else: #the function gives a meaningful
        #output even if the input saturation parameters are equal
    if mag_max!=0:
      mag=np.ones(mag.shape)
  return mag

#this function takes in input three stacks: hue, saturation, value
#defining the image in HSV colour space; and give in output
#an RGB stack of images clipped according the parameters
def fai_immagine(hue, saturation, value):
  w2_mag=clipping(value,sat_value_up,sat_value_down)
  w2_sat=clipping(saturation,sat_sat_up,sat_sat_down)
  w2_ang=np.array(hue).copy()
  w2_ang=(w2_ang+np.pi)/(2*np.pi)
  w2_img=np.array(255*np.array(hsv_to_rgb_vett(w2_ang,w2_sat,w2_mag)), 'uint8')
  immagine=np.swapaxes(w2_img,0,-1)
  return immagine

#this function takes in input a data stack and gives in output a
#stack of grayscale images without loss of information
def immagine_grigi(canale):
  interi=canale.astype('float32')
  img_grigi=np.swapaxes(np.flipud(np.rot90(interi)),0,-1)
  return img_grigi
```

```
hsv_to_rgb_vett=np.vectorize(colorsys.hsv_to_rgb)

if rp: #excetuted if RP-CARS acquisition
  if saturation_max:
    saturation=uni.copy() #colour saturation set to maximum
  else:
    saturation=r2#colour saturation as a function of A2w

  #this part creates the RGB alpha-value image stack
  alpha=np.arctan(r2/dc)*180/np.pi
  alpha_mod=np.copy(alpha)
  alpha_mod[alpha>alpha_max]=alpha_max
  alpha_mod[alpha<alpha_min]=alpha_min
  alpha_norm=(alpha_mod-alpha_min)/(3*(alpha_max-alpha_min))
  dc_norm=clipping(dc,sat_value_up,sat_value_down)
  r2_norm=clipping(saturation,sat_sat_up,sat_sat_down)
  semaforo=np.array(255*np.array(hsv_to_rgb_vett(alpha_norm,r2_norm, dc_norm)), '
      uint8')
  immagine_semaforo=np.swapaxes(semaforo,0,-1)

  immagine_w2=fai_immagine(p2, saturation, dc) #this line creates
                                               #the RGB phase image stack
  immagine_r2=immagine_grigi(r2) #grayscale image stack of A2w
  immagine_dc=immagine_grigi(dc) #grayscale image stack of Adc
  immagine_alpha=immagine_grigi(alpha) #grayscale image stack of alpha-value

  #the following lines save the created images
  tifffile.imsave(cartella_output+os.path.basename(os.path.normpath(
      cartella_input))+'img_semaforo.tiff', immagine_semaforo)
  tifffile.imsave(cartella_output+os.path.basename(os.path.normpath(
      cartella_input))+'img_w2.tiff', immagine_w2)
  tifffile.imsave(cartella_output+os.path.basename(os.path.normpath(
      cartella_input))+'img_r2.tiff', immagine_r2)
  tifffile.imsave(cartella_output+os.path.basename(os.path.normpath(
      cartella_input))+'img_dc.tiff', immagine_dc)
  tifffile.imsave(cartella_output+os.path.basename(os.path.normpath(
      cartella_input))+'alpha.tiff', immagine_alpha)
else: #excetuted if traditional CARS acquisition
  immagine_0=immagine_grigi(dc0) #this line creates a grayscale
                                 #image stack of PMT channel 0
  immagine_1=immagine_grigi(dc1) #this line creates a grayscale
                                 #image stack of PMT channel 1
  immagine_media=immagine_grigi((dc1+dc0)/2) #average image stack
```

```
                                                #of the two channels
155   #the following lines save the created images
      tifffile.imsave(cartella_output+os.path.basename(os.path.normpath(
          cartella_input))+'img_dc0.tiff', immagine_0)
157   tifffile.imsave(cartella_output+os.path.basename(os.path.normpath(
          cartella_input))+'img_dc1.tiff', immagine_1)
      tifffile.imsave(cartella_output+os.path.basename(os.path.normpath(
          cartella_input))+'img_dc_media.tiff', immagine_media)
```

Listing 2: Custom-made Python software application used to compute the average α value for each z-stack (A).

```
      #!/usr/bin/python
2
      """Find the average alpha value of a z-stack"""
4
      #This program loads the Adc and alpha values previously
6     #stored in tiff files (1 channel and 3 spatial dimensions)
      #and computes the average alpha value for each z-stack;
8     #optionally it also generates diagnostic stacks for the
      #purpose to manually inspecting the chosen thresholds.
10    #Its only input is the master directory that is recursively
      #scanned to find the z-stacks located in its sub-directories.
12    #Each sub-directory must contain only 1 Adc and 1 alpha zstacks
      #pertaining to the same acquisition. Zstacks pertaining to
14    #different acquisitions must be stored in different sub-directories.

16    #loading the necessary modules
      from thresholding import threshold_isodata
18    import tifffile as tif
      import numpy as np
20    import numpy.ma as ma
      import glob,sys,os
22
      #set True to generate diagnostic stacks to
24    #manually inspect the chosen thresholds
      show_mask=True
26
      #input sanitisation, define the input folder parameter
28    cartella_input=os.path.abspath(sys.argv[1])+'/'

30    #This function takes in input a zstacks-containing sub-directory
      #and returns in output the average alpha value.
```

```
#The function first identifies the optical slice
#along the z-axis with the highest average Adc value.
#Then the isodata algorithm is applied to this
#slice in order to find the Adc threshold value.
#After that, all the pixels in the z-stack
#with Adc value higher than the threshold are selected
#and the average of their alpha values
#is taken as the average alpha value of the z-stack.

def estrai_alpha(cartella_in):
  nome_file_dc=glob.glob(cartella_in+"*dc.tiff")
  nome_file_alpha=glob.glob(cartella_in+"*alpha.tiff")
  stack_dc=tif.imread(nome_file_dc[0])
  media_slice= np.mean(stack_dc.reshape(stack_dc.shape[0],-1),axis=1)
  slice_max_index=np.where(media_slice==media_slice.max())
  slice_max=stack_dc[slice_max_index[0],...]
  soglia=threshold_isodata(slice_max,return_all=True)[-1]
  maschera=np.where(stack_dc>soglia, False, True)
  dc_mask=ma.array(stack_dc, mask = maschera)
  alpha=tif.imread(nome_file_alpha[0])
  alpha_mask=ma.array(alpha, mask = maschera)
  alpha_medio=alpha_mask.mean()
  return alpha_medio,dc_mask

#This function takes in input the Adc masked numpy array and
#returns in output a numpy array representing an rgb image.
#Its purpose is to give the user the possibility to manually
#ispecting the automatically generated masks.

def fai_immagine(img):
  img2=img[...,np.newaxis]
  rgb=ma.concatenate((img2,img2,img2),-1)
  masch=ma.getmaskarray(rgb)
  data=ma.getdata(rgb)
  rgb_norm=(data-data.min())/(data.max()-data.min())
  rgb_int=np.array(255*rgb_norm, dtype='uint8')
  rosso=255*np.ones((rgb_int.shape[:-1]))
  rossastro=rgb_int.copy()
  rossastro[...,0]=rosso
  img_rgb=np.where(masch==True,rossastro,rgb_int)
  return img_rgb

#opening of the output file
```

```
file_res=open(cartella_input+'risultati_alpha.txt','w')
file_res.write('experiment_name\talpha\n')

#if show_mask is True, then create the diagnostic output directory
if show_mask and not os.path.exists(cartella_input+'maschere/'):
    os.makedirs(cartella_input+'maschere/')

#this for cycle recursively scans the master directory
#to find the z-stacks located in its sub-directories.
#Then it calls the function "estrai_alpha"
#(and, optionally, also "fai_immagine")
#to generate the requested program outputs.

for root, dirs, files in os.walk(cartella_input):
  root+='/'
  for nome_file in files:
    if nome_file.find('dc.tiff')>-1:
      alpha,mascherato=estrai_alpha(root)
      percorso=root.split('/')
      exp=percorso[-3]
      acquisiz=percorso[-2]
      nome_exp=exp+'_'+acquisiz
      file_res.write(nome_exp+'\t'+str(alpha)+'\n')
      if show_mask:
        img_maschera=fai_immagine(mascherato)
        tif.imsave(cartella_input+'maschere/'+exp+'_'+acquisiz+'_.tif',
            img_maschera)
      break

#closing the out file and ending the program
file_res.close()
```

Listing 3: Custom-made Python software application used to compute the resultant length (β) of the ϕ values on different spatial scales.

```
#!/usr/bin/python

"""Compute the average resultant length of a phase stack"""

#This program loads the raw microscopy data (ASCII .dat files)
#and computes the resultant length
#(i.e. an index of angular dispersion which is
#equal to one minus the angular variance)
```

```
#of the phase values on different spatial scales.
#Before the computation, the phase values are
#masked basing on a percentile value of their
#corresponding Adc values and the resultant length
#is averaged using the number of over-threshold
#pixels as weight

#loading the necessary modules
import numpy as np
import tifffile as tiff
import sys,glob,os,colorsys,re
import numpy.ma as ma
from scipy import ndimage

#input sanitisation and definition the input and output folder parameters
cartella_input=os.path.abspath(sys.argv[1])+'/'
cartella_output=os.path.abspath(sys.argv[2])+'/'

soglia_dc=90 #setting the threshold to the 90th percentile
#if "taglia" is set as true, then the input data are
#cropped to facilitate the analysis
taglia=True
#if "show_mask" is set as True, then  diagnostic stacks
#are generated to manually inspect the chosen threshold
show_mask=True

#loading and sorting the input Adc, phase and info stacks
lista_file_dc=glob.glob(cartella_input+"*dc.dat")
lista_file_p2=glob.glob(cartella_input+"*P2w.dat")
lista_file_info=glob.glob(cartella_input+"*info.dat")
lista_file_dc.sort()
lista_file_p2.sort()
lista_file_info.sort()
numero_file=len(lista_file_dc)

#retrieving the imaging field size in microns
#previusly stored in the info files
file_info_nome=lista_file_info[0]
file_info = open(file_info_nome, 'r')
linee= [line.split(',') for line in file_info.readlines()]
campo=float(linee[2][4])-float(re.findall('-?\d+\.\d*',linee[2][3])[0])

#an exception is rised if the image dimensions are not equal
```

```
shape=(np.loadtxt(lista_file_dc[0])).shape
if shape[0]!=shape[1]:
  raise Exception("Image dimensions not equal")
else:
  size=shape[0]
pixel_size=campo/size #compute the pixel size

#creating dummy stacks
dc=np.zeros((numero_file,shape[0],shape[1]))
p2=np.zeros((numero_file,shape[0],shape[1]))

#loading raw data as numpy arrays
for file_index in range(numero_file):
  dc[file_index,...]=np.loadtxt(lista_file_dc[file_index])
  p2[file_index,...]=np.loadtxt(lista_file_p2[file_index])*np.pi/180

#if "taglia" is true, then the input data are cropped
#to facilitate the analysis
if taglia:
  if size==200:
    num_pixel=180
  elif size==100:
    num_pixel=90
  taglio=(size-num_pixel)/2
  dc=dc[:,taglio:size-taglio,taglio:size-taglio]
  p2=p2[:,taglio:size-taglio,taglio:size-taglio]
  size=num_pixel

#this function divides the input stack ("matrice")
#in "num_div" squares (subimages) for each slice and
#it reconstructs a new stack with them
def quadratini(matrice,num_div):
  n_slice=matrice.shape[0]
  a=np.array(np.split(matrice,num_div,1))
  b=np.array(np.split(a,num_div,3))
  c=b.reshape((num_div*num_div*n_slice,-1))
  return c

#this function computes the resultant length
#(i.e. an index of angular dispersion which is
#equal to one minus the angular variance)
#of each subimage and then it averages them
#using the number of over-threshold pixels
```

```
#in each subimage as weight
def var_intra(matrice):
  v_quadrati=(np.sqrt(np.square(np.cos(matrice).sum(axis=1))
             +np.square(np.sin(matrice).sum(axis=1))))/matrice.count(axis=1)
  pesi=matrice.count(axis=1)/float(matrice.count())
  var_media=(v_quadrati*pesi).sum()
  return var_media

#the chosen threshold is applied translating it
#from percentile to raw value
dc_min=np.percentile(dc,soglia_dc)
soglia=np.zeros(dc.shape,dtype=np.bool)
soglia[dc<dc_min]=True
#closing of the binary mask
for soglia_index in range(numero_file):
  soglia[soglia_index,...] = ndimage.binary_dilation(soglia[soglia_index,...])
  soglia[soglia_index,...] = ndimage.binary_erosion(soglia[soglia_index,...],
                             structure=np.ones((3,3)),border_value=1)

#creating the output arrays
varianza_x=[]
varianza_y_intra=[]

#this cycle finds all the divisors of the
#image size in pixels. Then it divides the phase stack
#in subimages whose size in pixels is equal to the divisors.
#Finally it computes the weighted
#resultant length for the stack divided in sub-images.
for index_lato in range(1,size+1):
  if size % index_lato != 0:
    continue
  divisioni=size / index_lato
  soglia_quadrati=quadratini(soglia,divisioni)
  p2_quadrati=quadratini(p2,divisioni)
  #applying the mask to the phase data
  matrice_ma=ma.array(p2_quadrati, mask=soglia_quadrati)
  varianza_y_intra.append(var_intra(matrice_ma))
  varianza_x.append(index_lato*pixel_size)

#save the output results
nome_file=cartella_output+os.path.basename(os.path.normpath(cartella_input))
np.savetxt(nome_file+'_'+str(soglia_dc)+
           '.txt',np.array([varianza_x,varianza_y_intra]))
```

```
#This function takes in input the a masked numpy array and
#returns in output a numpy array representing an rgb image.
#Its purpose is to give the user the possibility to manually
#ispecting the automatically generated masks.
def fai_immagine(img):
  img2=img[...,np.newaxis]
  rgb=ma.concatenate((img2,img2,img2),-1)
  masch=ma.getmaskarray(rgb)
  data=ma.getdata(rgb)
  rgb_norm=(data-data.min())/(data.max()-data.min())
  rgb_int=np.array(255*rgb_norm, dtype='uint8')
  rosso=255*np.ones((rgb_int.shape[:-1]))
  rossastro=rgb_int.copy()
  rossastro[...,0]=rosso
  img_rgb=np.where(masch==True,rossastro,rgb_int)
  return img_rgb

#if show_mask is True, then create the diagnostic output stacks
if show_mask:
  mascherato=ma.array(dc, mask=soglia)
  img_maschera=fai_immagine(mascherato)
  tiff.imsave(cartella_output+os.path.basename(os.path.normpath(cartella_input))
              +'img.tiff', img_maschera)
```

LIST OF PUBLICATIONS

- A. Canta, A. Chiorazzi, V. A. Carozzi, C. Meregalli, N. Oggioni, M. Bossi, V. Rodriguez-Menendez, F. Avezza, L. Crippa, R. Lombardi, **G. de Vito**, V. Piazza, G. Cavaletti & P. Marmiroli · *Neurobiology of Aging* · Age-related changes in the function and the structure of the peripheral sensory pathway in mice (2016) 45:136–148

- V. Piazza, **G. de Vito**, E. Farrokhtakin, G. Ciofani & V. Mattoli · *PLOS ONE* · Femtosecond laser pulse characterization and optimization for CARS microscopy (2016) 11:e0156371

- A. Marino, J. Barsotti, **G. de Vito**, C. Filippeschi, B. Mazzolai, V. Piazza, M. Labardi, V. Mattoli & G. Ciofani · *ACS applied materials & interfaces* · Two-Photon Lithography of 3D Nanocomposite Piezoelectric Scaffolds for Cell Stimulation (2015) 7:25574–25579

- **G. de Vito**, A. Canta, P. Marmiroli & V. Piazza · *Journal of Microscopy* · A large-field polarisation-resolved laser scanning microscope: applications to CARS imaging (2015) 260:194–199

- A. Rocca, A. Marino, V. Rocca, S. Moscato, **G. de Vito**, V. Piazza, B. Mazzolai, V. Mattoli, T.J. Ngo-Anh & G. Ciofani · *International Journal of Nanomedicine* · Barium titanate nanoparticles and hypergravity stimulation improve differentiation of mesenchymal stem cells into osteoblasts (2015) 7:19–24

- **G. de Vito**, I. Tonazzini, M. Cecchini & V. Piazza · *Optics express* · RP-CARS: label-free optical readout of the myelin intrinsic healthiness (2014) 22:13733–13743

- **G. de Vito** & V. Piazza · *Optical Data Processing and Storage* · Fast signal analysis in Rotating-Polarization CARS microscopy (2014) 1:1–5

- G. Ciofani, S. Del Turco, A. Rocca, **G. de Vito**, V. Cappello, M. Yamaguchi, X. Li, B. Mazzolai, G. Basta, M. Gemmi, V. Piazza, D. Golberg & V. Mattoli · *Nanomedicine* · Cytocompatibility evaluation of gum Arabic-coated ultra-pure boron nitride nanotubes on human cells (2014) 9:773–788

- E. FarrokhTakin, G. Ciofani, G.L. Puleo, **G. de Vito**, C. Filippeschi, B. Mazzolai, V. Piazza & V. Mattoli · *International Journal of Nanomedicine* · Barium titanate core–gold shell nanoparticles for hyperthermia treatments (2013) 8:2319–2331

- **G. de Vito**, A. Bifone & V. Piazza · *Optics express* · Rotating-polarization CARS microscopy: combining chemical and molecular orientation sensitivity (2012) 20:29369–29377

IN PRESS

- **G. de Vito**, V. Cappello, I. Tonazzini, M. Cecchini & V. Piazza · *Journal of Biophotonics* · RP-CARS reveals molecular spatial order anomalies in myelin of an animal model of Krabbe disease (2016)

ACKNOWLEDGEMENTS

First of all, I would like to thank Professor Fabio Beltram for granting me the possibility to undertake this academic path and for allowing me access to the advanced facilities of the NEST laboratory.

I would like to thank my advisor, Dr. Vincenzo Piazza, for always tutoring me with patience and care, as well as for giving me an example to follow of scientific rigour and passion and dedication to scientific work.

I would also like to thank Dr. Gian Michele Ratto for having introduced me to the world of scientific research, for having taught me always to maintain a creative vision, and for his deeply honest and useful advice. I would also like to thank Dr. Silvia Landi for selflessly giving me a hand every time I needed it in Dr. Ratto's laboratory.

I would like to thank Dr. Marco Cecchini and Dr. Ilaria Tonazzini for their kind help with the Twitcher mice.

A particular acknowledgement goes to Professor Eric Potma of the University of California-Irvine, for giving me the precious opportunity to spend months in his laboratory, for trusting me from the very beginning and for kindly teaching me the principles of SHG/SFG microscopy. I would like to thank Dr. Janaka Chamith Ranasinghesagara of the same University for the great help he gave me with the HF-WEFS code. I would also like to thank the members of Prof. Potma's research group: Adam, Alba, Julie, Junghoon, Faezeh, Alex, Ryan and Brian, and the visiting scholar Chris, for their advice and help and, most of all, for making me feel at home in their laboratory.

I would like to thank Federica Bacarella for her help with the microscopy acquisitions of the Twitcher mice nerve samples.

Among the ex-Ph.D. students, I would like to thank Marco, Sebastian and Sandro for the interesting conversations, the company and the useful advice.

Finally I want to thank my family for morally supporting me over the years of my education, my ex-flatmate and friend Luca for our fruitful discussions about our mutual work, and my fiancée, Emanuela, for always being at my side, in particular during the writing of this thesis.

A final mention goes to my pet shrimp for always keeping me company on my office desk during the Ph.D. years.

BIBLIOGRAPHY

[1] A. van Leeuwenhoek, "Letter on the protozoa," *Philosophical Transactions of the Royal Society*, 1677.

[2] I. Ghiran, "Introduction to Fluorescence Microscopy," in *Light Microscopy* (H. Chiarini-Garcia and R. C. N. Melo, eds.), no. 689 in Methods in Molecular Biology, pp. 93–136, Humana Press, Jan. 2011.

[3] A. H. Coons, H. J. Creech, and R. N. Jones, "Immunological Properties of an Antibody Containing a Fluorescent Group.," *Experimental Biology and Medicine*, vol. 47, pp. 200–202, Jan. 1941.

[4] M. Minsky, "Confocal scanning microscope," 1955.

[5] R. Y. Tsien, L. Ernst, and A. Waggoner, "Fluorophores for Confocal Microscopy: Photophysics and Photochemistry," in *Handbook of Biological Confocal Microscopy* (J. B. Pawley, ed.), pp. 338–352, Springer US, 2006.

[6] E. J. G. Peterman, H. Sosa, and W. E. Moerner, "Single-Molecule Fluorescence Spectroscopy and Microscopy of Biomolecular Motors," *Annual Review of Physical Chemistry*, vol. 55, no. 1, pp. 79–96, 2004.

[7] T. Ha, "Single-molecule fluorescence methods for the study of nucleic acids," *Current Opinion in Structural Biology*, vol. 11, pp. 287–292, June 2001.

[8] A. Ishijima and T. Yanagida, "Single molecule nanobioscience," *Trends in Biochemical Sciences*, vol. 26, pp. 438–444, July 2001.

[9] R. Roy, S. Hohng, and T. Ha, "A practical guide to single-molecule FRET," *Nature Methods*, vol. 5, pp. 507–516, June 2008.

[10] W. E. Moerner and D. P. Fromm, "Methods of single-molecule fluorescence spectroscopy and microscopy," *Review of Scientific Instruments*, vol. 74, pp. 3597–3619, Aug. 2003.

[11] H. P. Lu, L. Xun, and X. S. Xie, "Single-Molecule Enzymatic Dynamics," *Science*, vol. 282, pp. 1877–1882, Dec. 1998.

[12] N. G. Walter, C.-Y. Huang, A. J. Manzo, and M. A. Sobhy, "Do-it-yourself guide: How to use the modern single-molecule toolkit," *Nature Methods*, vol. 5, pp. 475–489, June 2008.

[13] L. S. Churchman, Z. Ökten, R. S. Rock, J. F. Dawson, and J. A. Spudich, "Single molecule high-resolution colocalization of Cy3 and Cy5 attached to macromolecules measures intramolecular distances through time," *Proceedings of the National Academy of Sciences of the United States of America*, vol. 102, pp. 1419–1423, Jan. 2005.

[14] M. F. García-Parajó, J.-A. Veerman, R. Bouwhuis, R. Vallée, and N. F. van Hulst, "Optical Probing of Single Fluorescent Molecules and Proteins," *ChemPhysChem*, vol. 2, pp. 347–360, June 2001.

[15] M. P. Gordon, T. Ha, and P. R. Selvin, "Single-molecule high-resolution imaging with photobleaching," *Proceedings of the National Academy of Sciences of the United States of America*, vol. 101, pp. 6462–6465, Apr. 2004.

[16] Abbe, "The Relation of Aperture and Power in the Microscope (continued).," *Journal of the Royal Microscopical Society*, vol. 2, pp. 460–473, Aug. 1882.

[17] A. Diaspro, *Nanoscopy and Multidimensional Optical Fluorescence Microscopy*. CRC Press, Apr. 2010.

[18] S. W. Hell, "Far-Field Optical Nanoscopy," *Science*, vol. 316, pp. 1153–1158, May 2007.

[19] T. J. Gould and S. T. Hess, "Chapter 12 Nanoscale Biological Fluorescence Imaging: Breaking the Diffraction Barrier," vol. 89 of *Biophysical Tools for Biologists, Volume Two: In Vivo Techniques*, pp. 329–358, Academic Press, 2008.

[20] S. W. Hell, "Microscopy and its focal switch," *Nature Methods*, vol. 6, pp. 24–32, Jan. 2009.

[21] K. I. Willig, J. Keller, M. Bossi, and S. W. Hell, "STED microscopy resolves nanoparticle assemblies," *New Journal of Physics*, vol. 8, no. 6, p. 106, 2006.

[22] T. J. Gould, V. V. Verkhusha, and S. T. Hess, "Imaging biological structures with fluorescence photoactivation localization microscopy," *Nature Protocols*, vol. 4, pp. 291–308, Feb. 2009.

[23] E. Betzig, G. H. Patterson, R. Sougrat, O. W. Lindwasser, S. Olenych, J. S. Bonifacino, M. W. Davidson, J. Lippincott-Schwartz, and H. F. Hess, "Imaging Intracellular Fluorescent Proteins at Nanometer Resolution," *Science*, vol. 313, pp. 1642–1645, Sept. 2006.

[24] S. T. Hess, T. P. K. Girirajan, and M. D. Mason, "Ultra-High Resolution Imaging by Fluorescence Photoactivation Localization Microscopy," *Biophysical Journal*, vol. 91, pp. 4258–4272, Dec. 2006.

[25] M. J. Rust, M. Bates, and X. Zhuang, "Sub-diffraction-limit imaging by stochastic optical reconstruction microscopy (STORM)," *Nature Methods*, vol. 3, pp. 793–796, Oct. 2006.

[26] A. Egner, S. Verrier, A. Goroshkov, H.-D. Söling, and S. W. Hell, "4Pi-microscopy of the Golgi apparatus in live mammalian cells," *Journal of Structural Biology*, vol. 147, pp. 70–76, July 2004.

[27] B. Huang, S. A. Jones, B. Brandenburg, and X. Zhuang, "Whole-cell 3D STORM reveals interactions between cellular structures with nanometer-scale resolution," *Nature Methods*, vol. 5, pp. 1047–1052, Dec. 2008.

[28] B. Huang, W. Wang, M. Bates, and X. Zhuang, "Three-Dimensional Super-Resolution Imaging by Stochastic Optical Reconstruction Microscopy," *Science*, vol. 319, pp. 810–813, Feb. 2008.

[29] E. G. Reynaud, U. Kržič, K. Greger, and E. H. K. Stelzer, "Light sheet-based fluorescence microscopy: More dimensions, more photons, and less photodamage," *HFSP Journal*, vol. 2, pp. 266–275, Oct. 2008.

[30] J. Lippincott-Schwartz and S. Manley, "Putting super-resolution fluorescence microscopy to work," *Nature Methods*, vol. 6, pp. 21–23, Jan. 2009.

[31] S. W. Hell, R. Schmidt, and A. Egner, "Diffraction-unlimited three-dimensional optical nanoscopy with opposing lenses," *Nature Photonics*, vol. 3, pp. 381–387, July 2009.

[32] R. K. Chhetri, F. Amat, Y. Wan, B. Höckendorf, W. C. Lemon, and P. J. Keller, "Whole-animal functional and developmental imaging with isotropic spatial resolution," *Nature Methods*, vol. 12, pp. 1171–1178, Oct. 2015.

[33] W. C. Lemon, S. R. Pulver, B. Höckendorf, K. McDole, K. Branson, J. Freeman, and P. J. Keller, "Whole-central nervous system functional imaging in larval Drosophila," *Nature Communications*, vol. 6, p. 7924, Aug. 2015.

[34] P. J. Keller and M. B. Ahrens, "Visualizing Whole-Brain Activity and Development at the Single-Cell Level Using Light-Sheet Microscopy," *Neuron*, vol. 85, pp. 462–483, Feb. 2015.

[35] P. J. Keller, M. B. Ahrens, and J. Freeman, "Light-sheet imaging for systems neuroscience," *Nature Methods*, vol. 12, pp. 27–29, Dec. 2014.

[36] M. B. Ahrens, M. B. Orger, D. N. Robson, J. M. Li, and P. J. Keller, "Whole-brain functional imaging at cellular resolution using light-sheet microscopy," *Nature Methods*, vol. 10, pp. 413–420, Mar. 2013.

[37] R. Prevedel, Y.-G. Yoon, M. Hoffmann, N. Pak, G. Wetzstein, S. Kato, T. Schrödel, R. Raskar, M. Zimmer, E. S. Boyden, and A. Vaziri, "Simultaneous whole-animal 3D imaging of neuronal activity using light-field microscopy," *Nature Methods*, vol. 11, pp. 727–730, July 2014.

[38] T. Schrödel, R. Prevedel, K. Aumayr, M. Zimmer, and A. Vaziri, "Brain-wide 3D imaging of neuronal activity in Caenorhabditis elegans with sculpted light," *Nature Methods*, vol. 10, pp. 1013–1020, Oct. 2013.

[39] S. Wolf, W. Supatto, G. Debrégeas, P. Mahou, S. G. Kruglik, J.-M. Sintes, E. Beaurepaire, and R. Candelier, "Whole-brain functional imaging with two-photon light-sheet microscopy," *Nature Methods*, vol. 12, pp. 379–380, May 2015.

[40] D. Arosio, F. Ricci, L. Marchetti, R. Gualdani, L. Albertazzi, and F. Beltram, "Simultaneous intracellular chloride and pH measurements using a GFP-based sensor," *Nature Methods*, vol. 7, pp. 516–518, Jan. 2010.

[41] D. Arosio and G. M. Ratto, "Twenty years of fluorescence imaging of intracellular chloride," *Frontiers in Cellular Neuroscience*, vol. 8, Aug. 2014.

[42] S. Jayaraman, J. Biwersi, and A. S. Verkman, "Synthesis and characterization of dual-wavelength Cl–sensitive fluorescent indicators for ratio imaging," *American Journal of Physiology - Cell Physiology*, vol. 276, pp. C747–C757, Mar. 1999.

[43] S. D. Watts, K. L. Suchland, S. G. Amara, and S. L. Ingram, "A Sensitive Membrane-Targeted Biosensor for Monitoring Changes in Intracellular Chloride in Neuronal Processes," *PLOS ONE*, vol. 7, no. 4, p. e35373, 10-apr-2012.

[44] T. Kuner and G. J. Augustine, "A Genetically Encoded Ratiometric Indicator for Chloride: Capturing Chloride Transients in Cultured Hippocampal Neurons," *Neuron*, vol. 27, pp. 447–459, Sept. 2000.

[45] J. S. Grimley, L. Li, W. Wang, L. Wen, L. S. Beese, H. W. Hellinga, and G. J. Augustine, "Visualization of Synaptic Inhibition with an Optogenetic Sensor Developed by Cell-Free Protein Engineering Automation," *The Journal of Neuroscience*, vol. 33, pp. 16297–16309, Sept. 2013.

[46] J. V. Raimondo, A. Irkle, W. Wefelmeyer, S. E. Newey, and C. J. Akerman, "Genetically encoded proton sensors reveal activity-dependent pH changes in neurons," *Frontiers in Molecular Neuroscience*, vol. 5, May 2012.

[47] O. Markova, M. Mukhtarov, E. Real, Y. Jacob, and P. Bregestovski, "Genetically encoded chloride indicator with improved sensitivity," *Journal of Neuroscience Methods*, vol. 170, pp. 67–76, May 2008.

[48] R. Y. Tsien, "Fluorescence measurement and photochemical manipulation of cytosolic free calcium," *Trends in Neurosciences*, vol. 11, pp. 419–424, Jan. 1988.

[49] A. Minta, J. P. Kao, and R. Y. Tsien, "Fluorescent indicators for cytosolic calcium based on rhodamine and fluorescein chromophores," *The Journal of Biological Chemistry*, vol. 264, pp. 8171–8178, May 1989.

[50] J. P. Kao, A. T. Harootunian, and R. Y. Tsien, "Photochemically generated cytosolic calcium pulses and their detection by fluo-3," *The Journal of Biological Chemistry*, vol. 264, pp. 8179–8184, May 1989.

[51] C. Stosiek, O. Garaschuk, K. Holthoff, and A. Konnerth, "In vivo two-photon calcium imaging of neuronal networks," *Proceedings of the National Academy of Sciences*, vol. 100, pp. 7319–7324, Oct. 2003.

[52] M. B. Cannell, J. R. Berlin, and W. J. Lederer, "Intracellular calcium in cardiac myocytes: Calcium transients measured using fluorescence imaging," *Society of General Physiologists Series*, vol. 42, pp. 201–214, 1987.

[53] M. V. Ivannikov and G. T. Macleod, "Mitochondrial Free Ca^{2+} Levels and Their Effects on Energy Metabolism in Drosophila Motor Nerve Terminals," *Biophysical Journal*, vol. 104, pp. 2353–2361, June 2013.

[54] T. Thestrup, J. Litzlbauer, I. Bartholomäus, M. Mues, L. Russo, H. Dana, Y. Kovalchuk, Y. Liang, G. Kalamakis, Y. Laukat, S. Becker, G. Witte, A. Geiger, T. Allen, L. C. Rome, T.-W. Chen, D. S. Kim, O. Garaschuk, C. Griesinger, and O. Griesbeck, "Optimized ratiometric calcium sensors for functional in vivo imaging of neurons and T lymphocytes," *Nature Methods*, vol. 11, pp. 175–182, Feb. 2014.

[55] Y. Kovalchuk, R. Homma, Y. Liang, A. Maslyukov, M. Hermes, T. Thestrup, O. Griesbeck, J. Ninkovic, L. B. Cohen, and O. Garaschuk, "In vivo odourant response properties of migrating adult-born neurons in the mouse olfactory bulb," *Nature Communications*, vol. 6, p. 6349, Feb. 2015.

[56] K.-P. Yip and I. Kurtz, "Confocal Fluorescence Microscopy Measurements of pH and Calcium in Living Cells," in *Methods in Cell Biology* (B. Matsumoto, ed.), vol. 70, pp. 417–427, Academic Press, Jan. 2003.

[57] M. Kneen, J. Farinas, Y. Li, and A. S. Verkman, "Green Fluorescent Protein as a Noninvasive Intracellular pH Indicator," *Biophysical Journal*, vol. 74, pp. 1591–1599, Mar. 1998.

[58] J. Llopis, J. M. McCaffery, A. Miyawaki, M. G. Farquhar, and R. Y. Tsien, "Measurement of cytosolic, mitochondrial, and Golgi pH in single living cells with green fluorescent proteins," *Proceedings of the National Academy of Sciences*, vol. 95, pp. 6803–6808, Sept. 1998.

[59] A. Miyawaki, J. Llopis, R. Heim, J. M. McCaffery, J. A. Adams, M. Ikura, and R. Y. Tsien, "Fluorescent indicators for Ca^{2+} based on green fluorescent proteins and calmodulin," *Nature*, vol. 388, pp. 882–887, Aug. 1997.

[60] A. Miyawaki, O. Griesbeck, R. Heim, and R. Y. Tsien, "Dynamic and quantitative Ca^{2+} measurements using improved cameleons," *Proceedings of the National Academy of Sciences*, vol. 96, pp. 2135–2140, Feb. 1999.

[61] T. Nagai, S. Yamada, T. Tominaga, M. Ichikawa, and A. Miyawaki, "Expanded dynamic range of fluorescent indicators for Ca^{2+} by circularly permuted yellow fluorescent proteins," *Proceedings of the National Academy of Sciences of the United States of America*, vol. 101, pp. 10554–10559, July 2004.

[62] T. Nagai, A. Sawano, E. S. Park, and A. Miyawaki, "Circularly permuted green fluorescent proteins engineered to sense Ca^{2+}," *Proceedings of the National Academy of Sciences*, vol. 98, pp. 3197–3202, Mar. 2001.

[63] L. Albertazzi, B. Storti, M. Brondi, S. Sulis Sato, G. Michele Ratto, G. Signore, and F. Beltram, "Synthesis, Cellular Delivery and In vivo Application of Dendrimer-based pH Sensors," *Journal of Visualized Experiments : JoVE*, Sept. 2013.

[64] R. Bizzarri, C. Arcangeli, D. Arosio, F. Ricci, P. Faraci, F. Cardarelli, and F. Beltram, "Development of a Novel GFP-based Ratiometric Excitation and Emission pH Indicator for Intracellular Studies," *Biophysical Journal*, vol. 90, pp. 3300–3314, May 2006.

[65] R. Y. Tsien, "Fluorescent Probes of Cell Signaling," *Annual Review of Neuroscience*, vol. 12, no. 1, pp. 227–253, 1989.

[66] I. Kurtz and R. S. Balaban, "Fluorescence emission spectroscopy of 1,4-dihydroxyphthalonitrile. A method for determining intracellular pH in cultured cells.," *Biophysical Journal*, vol. 48, pp. 499–508, Sept. 1985.

[67] I. Kurtz and C. Emmons, "Measurement of Intracellular pH with a Laser Scanning Confocal Microscope," in *Methods in Cell Biology* (G. Meurant, ed.), vol. 38, pp. 183–193, Academic Press, Nov. 1993.

[68] L. Li, H. Szmacinski, and J. R. Lakowicz, "Synthesis and Luminescence Spectral Characterization of Long-Lifetime Lipid Metal–Ligand Probes," *Analytical Biochemistry*, vol. 244, pp. 80–85, Jan. 1997.

[69] F. N. Castellano and J. R. Lakowicz, "A Water-Soluble Luminescence Oxygen Sensor," *Photochemistry and Photobiology*, vol. 67, pp. 179–183, Feb. 1998.

[70] J. Ji, N. Rosenzweig, I. Jones, and Z. Rosenzweig, "Novel fluorescent oxygen indicator for intracellular oxygen measurements," *Journal of Biomedical Optics*, vol. 7, no. 3, pp. 404–409, 2002.

[71] G. Signore, R. Nifosì, L. Albertazzi, and R. Bizzarri, "A Novel Coumarin Fluorescent Sensor to Probe Polarity Around Biomolecules," *Journal of Biomedical Nanotechnology*, vol. 5, pp. 722–729, Dec. 2009.

[72] G. Signore, R. Nifosì, L. Albertazzi, B. Storti, and R. Bizzarri, "Polarity-Sensitive Coumarins Tailored to Live Cell Imaging," *Journal of the American Chemical Society*, vol. 132, pp. 1276–1288, Feb. 2010.

[73] T. Parasassi, E. K. Krasnowska, L. Bagatolli, and E. Gratton, "Laurdan and Prodan as Polarity-Sensitive Fluorescent Membrane Probes," *Journal of Fluorescence*, vol. 8, pp. 365–373, Dec. 1998.

[74] Y. E. Kim, J. Chen, J. R. Chan, and R. Langen, "Engineering a polarity-sensitive biosensor for time-lapse imaging of apoptotic processes and degeneration," *Nature Methods*, vol. 7, pp. 67–73, Jan. 2010.

[75] A. Battisti, S. Panettieri, G. Abbandonato, E. Jacchetti, F. Cardarelli, G. Signore, F. Beltram, and R. Bizzarri, "Imaging intracellular viscosity by a new molecular rotor suitable for phasor analysis of fluorescence lifetime," *Analytical and Bioanalytical Chemistry*, vol. 405, pp. 6223–6233, June 2013.

[76] M. K. Kuimova, "Mapping viscosity in cells using molecular rotors," *Physical Chemistry Chemical Physics*, vol. 14, no. 37, p. 12671, 2012.

[77] J. Sutharsan, D. Lichlyter, N. E. Wright, M. Dakanali, M. A. Haidekker, and E. A. Theodorakis, "Molecular rotors: Synthesis and evaluation as viscosity sensors," *Tetrahedron*, vol. 66, pp. 2582–2588, Apr. 2010.

[78] C. D. Primio, V. Quercioli, A. Allouch, R. Gijsbers, F. Christ, Z. Debyser, D. Arosio, and A. Cereseto, "Single-Cell Imaging of HIV-1 Provirus (SCIP)," *Proceedings of the National Academy of Sciences*, vol. 110, pp. 5636–5641, Feb. 2013.

[79] Y. Sato, M. Mukai, J. Ueda, M. Muraki, T. J. Stasevich, N. Horikoshi, T. Kujirai, H. Kita, T. Kimura, S. Hira, Y. Okada, Y. Hayashi-Takanaka, C. Obuse, H. Kurumizaka, A. Kawahara, K. Yamagata, N. Nozaki, and H. Kimura, "Genetically encoded system to track histone modification in vivo," *Scientific Reports*, vol. 3, Aug. 2013.

[80] I. Johnson, "Pratical Considerations in the Selection and Application of Fluorescent Probes," in *Handbook of Biological Confocal Microscopy* (J. B. Pawley, ed.), pp. 353–367, Springer US, 2006.

[81] A. Kohler, "A microphotographic device for ultraviolet light (lambda= 275 mu) and investigations into organic tissues using this device," *Physikalische Zeitschrift*, vol. 5, pp. 666–673, 1904.

[82] M. Göppert-Mayer, "Über Elementarakte mit zwei Quantensprüngen," *Annalen der Physik*, vol. 401, pp. 273–294, Jan. 1931.

[83] W. Denk, J. H. Strickler, and W. W. Webb, "Two-photon laser scanning fluorescence microscopy," *Science*, vol. 248, pp. 73–76, Apr. 1990.

[84] B. Banerjee, T. Renkoski, L. R. Graves, N. S. Rial, V. L. Tsikitis, V. Nfonsam, J. Pugh, P. Tiwari, H. Gavini, and U. Utzinger, "Tryptophan autofluorescence imaging of neoplasms of the human colon," *Journal of Biomedical Optics*, vol. 17, no. 1, pp. 0160031–0160037, 2012.

[85] C. Li, R. K. Pastila, C. Pitsillides, J. M. Runnels, M. Puoris'haag, D. Côté, and C. P. Lin, "Imaging leukocyte trafficking in vivo with two-photon-excited endogenous tryptophan fluorescence," *Optics Express*, vol. 18, p. 988, Jan. 2010.

[86] J. V. Rocheleau, W. S. Head, and D. W. Piston, "Quantitative NAD(P)H/Flavoprotein Autofluorescence Imaging Reveals Metabolic Mechanisms of Pancreatic Islet Pyruvate Response," *Journal of Biological Chemistry*, vol. 279, pp. 31780–31787, July 2004.

[87] Q. Yu and A. A. Heikal, "Two-photon autofluorescence dynamics imaging reveals sensitivity of intracellular NADH concentration and conformation to cell physiology at the single-cell level," *Journal of Photochemistry and Photobiology B: Biology*, vol. 95, pp. 46–57, Apr. 2009.

[88] E. Dimitrow, I. Riemann, A. Ehlers, M. J. Koehler, J. Norgauer, P. Elsner, K. König, and M. Kaatz, "Spectral fluorescence lifetime detection and selective melanin imaging by multiphoton laser tomography for melanoma diagnosis," *Experimental Dermatology*, vol. 18, pp. 509–515, June 2009.

[89] C. N. Keilhauer and F. C. Delori, "Near-Infrared Autofluorescence Imaging of the Fundus: Visualization of Ocular Melanin," *Investigative Opthalmology & Visual Science*, vol. 47, p. 3556, Aug. 2006.

[90] H. J. Swatland, "Fiber-Optic Reflectance and Autofluorescence of Bovine Elastin and Differences Between Intramuscular and Extramuscular Tendon," *Journal of Animal Science*, vol. 64, pp. 1038–1043, Apr. 1987.

[91] A. Zoumi, X. Lu, G. S. Kassab, and B. J. Tromberg, "Imaging Coronary Artery Microstructure Using Second-Harmonic and Two-Photon Fluorescence Microscopy," *Biophysical Journal*, vol. 87, pp. 2778–2786, Oct. 2004.

[92] C. J. R. Sheppard and R. Kompfner, "Resonant scanning optical microscope," *Applied Optics*, vol. 17, p. 2879, Sept. 1978.

[93] I. Freund and M. Deutsch, "Second-harmonic microscopy of biological tissue," *Optics Letters*, vol. 11, p. 94, Feb. 1986.

[94] W. R. Zipfel, R. M. Williams, and W. W. Webb, "Nonlinear magic: Multiphoton microscopy in the biosciences," *Nature Biotechnology*, vol. 21, pp. 1369–1377, Nov. 2003.

[95] R. W. Boyd and B. R. Masters, "Nonlinear optical spectroscopy," in *Handbook of Biomedical Nonlinear Optical Microscopy* (B. R. Masters and P. T. C. So, eds.), Oxford University Press, 2008.

[96] R. Cicchi, N. Vogler, D. Kapsokalyvas, B. Dietzek, J. Popp, and F. S. Pavone, "From molecular structure to tissue architecture: Collagen organization probed by SHG microscopy," *Journal of Biophotonics*, vol. 6, pp. 129–142, Feb. 2013.

[97] J. Mertz, "Application of Second-Harmonic Generation Microscopy," in *Handbook of Biomedical Nonlinear Optical Microscopy* (B. R. Masters and P. T. C. So, eds.), Oxford University Press, 2008.

[98] S. V. Plotnikov, A. C. Millard, P. J. Campagnola, and W. A. Mohler, "Characterization of the Myosin-Based Source for Second-Harmonic Generation from Muscle Sarcomeres," *Biophysical Journal*, vol. 90, pp. 693–703, Jan. 2006.

[99] P. J. Campagnola, "Second-harmonic generation imaging microscopy," in *Handbook of Biomedical Nonlinear Optical Microscopy* (B. R. Masters and P. T. C. So, eds.), Oxford University Press, 2008.

[100] D. Débarre, W. Supatto, A.-M. Pena, A. Fabre, T. Tordjmann, L. Combettes, M.-C. Schanne-Klein, and E. Beaurepaire, "Imaging lipid bodies in cells and tissues using third-harmonic generation microscopy," *Nature Methods*, vol. 3, pp. 47–53, Jan. 2006.

[101] J. M. Bélisle, S. Costantino, M. L. Leimanis, M.-J. Bellemare, D. Scott Bohle, E. Georges, and P. W. Wiseman, "Sensitive Detection of Malaria Infection by Third Harmonic Generation Imaging," *Biophysical Journal*, vol. 94, pp. L26–L28, Feb. 2008.

[102] N. J. Everall, "Confocal Raman Microscopy: Performance, Pitfalls, and Best Practice," *Applied Spectroscopy*, vol. 63, pp. 245A–262A, Sept. 2009.

[103] D. J. Gardiner, "Introduction to Raman Scattering," in *Practical Raman Spectroscopy* (D. D. J. Gardiner and D. P. R. Graves, eds.), pp. 1–12, Springer Berlin Heidelberg, 1989.

[104] H.-J. van Manen, Y. M. Kraan, D. Roos, and C. Otto, "Single-cell Raman and fluorescence microscopy reveal the association of lipid bodies with phagosomes in leukocytes," *Proceedings of the National Academy of Sciences of the United States of America*, vol. 102, pp. 10159–10164, July 2005.

[105] P. D. Maker and R. W. Terhune, "Study of Optical Effects Due to an Induced Polarization Third Order in the Electric Field Strength," *Physical Review*, vol. 137, pp. A801–A818, Feb. 1965.

[106] J.-X. Cheng and X. S. Xie, *Coherent Raman Scattering Microscopy*. CRC Press, Oct. 2012.

[107] J.-X. Cheng, A. Volkmer, and X. S. Xie, "Theoretical and experimental characterization of coherent anti-Stokes Raman scattering microscopy," *Journal of the Optical Society of America B*, vol. 19, p. 1363, June 2002.

[108] J.-x. Cheng, A. Volkmer, L. D. Book, and X. S. Xie, "An Epi-Detected Coherent Anti-Stokes Raman Scattering (E-CARS) Microscope with High Spectral Resolution and High Sensitivity," *The Journal of Physical Chemistry B*, vol. 105, pp. 1277–1280, Feb. 2001.

[109] C. L. Evans and X. S. Xie, "Coherent Anti-Stokes Raman Scattering Microscopy: Chemical Imaging for Biology and Medicine," *Annual Review of Analytical Chemistry*, vol. 1, no. 1, pp. 883–909, 2008.

[110] H. Lotem, R. T. Lynch, and N. Bloembergen, "Interference between Raman resonances in four-wave difference mixing," *Physical Review A*, vol. 14, pp. 1748–1755, Nov. 1976.

[111] S. Maeda, T. Kamisuki, and Y. Adachi, "Condensed phase CARS," *Advances in spectroscopy*, vol. 15, pp. 253–297, 1988.

[112] R. W. Hellwarth, "Third-order optical susceptibilities of liquids and solids," *Progress in Quantum Electronics*, vol. 5, pp. 1–68, 1977.

[113] E. O. Potma, X. S. Xie, A. Volkmer, and J.-X. Cheng, "Coherent Raman Scattering under Tightly Focused Conditions," in *Coherent Raman Scattering Microscopy* (J.-X. Cheng and X. S. Xie, eds.), Cellular and Clinical Imaging, CRC Press, Oct. 2012.

[114] A. Zumbusch, G. R. Holtom, and X. S. Xie, "Three-Dimensional Vibrational Imaging by Coherent Anti-Stokes Raman Scattering," *Physical Review Letters*, vol. 82, pp. 4142–4145, May 1999.

[115] T. Bernas, M. Zarębski, R. R. Cook, and J. W. Dobrucki, "Minimizing photobleaching during confocal microscopy of fluorescent probes bound to chromatin: Role of anoxia and photon flux," *Journal of Microscopy*, vol. 215, pp. 281–296, Sept. 2004.

[116] J.-X. Cheng, L. D. Book, and X. S. Xie, "Polarization coherent anti-Stokes Raman scattering microscopy," *Optics Letters*, vol. 26, p. 1341, Sept. 2001.

[117] A. Volkmer, L. D. Book, and X. S. Xie, "Time-resolved coherent anti-Stokes Raman scattering microscopy: Imaging based on Raman free induction decay," *Applied Physics Letters*, vol. 80, pp. 1505–1507, Mar. 2002.

[118] M. D. Duncan, J. Reintjes, and T. J. Manuccia, "Scanning coherent anti-Stokes Raman microscope," *Optics Letters*, vol. 7, p. 350, Aug. 1982.

[119] J.-X. Cheng, Y. K. Jia, G. Zheng, and X. S. Xie, "Laser-Scanning Coherent Anti-Stokes Raman Scattering Microscopy and Applications to Cell Biology," *Biophysical Journal*, vol. 83, pp. 502–509, July 2002.

[120] C. L. Evans, E. O. Potma, M. Puoris'haag, D. Côté, C. P. Lin, and X. S. Xie, "Chemical imaging of tissue in vivo with video-rate coherent anti-Stokes Raman scattering microscopy," *Proceedings of the National Academy of Sciences of the United States of America*, vol. 102, pp. 16807–16812, Nov. 2005.

[121] G. Eckhardt, R. W. Hellwarth, F. J. McClung, S. E. Schwarz, D. Weiner, and E. J. Woodbury, "Stimulated Raman Scattering From Organic Liquids," *Physical Review Letters*, vol. 9, pp. 455–457, Dec. 1962.

[122] P. Kukura, D. W. McCamant, and R. A. Mathies, "Femtosecond Stimulated Raman Spectroscopy," *Annual Review of Physical Chemistry*, vol. 58, no. 1, pp. 461–488, 2007.

[123] C. W. Freudiger and X. S. Xie, "Stimulated Raman Scattering Microscopy," in *Coherent Raman Scattering Microscopy* (J.-X. Cheng and X. S. Xie, eds.), Cellular and Clinical Imaging, CRC Press, Oct. 2012.

[124] M. N. Slipchenko, R. A. Oglesbee, D. Zhang, W. Wu, and J.-X. Cheng, "Heterodyne detected nonlinear optical imaging in a lock-in free manner," *Journal of Biophotonics*, vol. 5, pp. 801–807, Oct. 2012.

[125] E. Ploetz, S. Laimgruber, S. Berner, W. Zinth, and P. Gilch, "Femtosecond stimulated Raman microscopy," *Applied Physics B*, vol. 87, pp. 389–393, Apr. 2007.

[126] C. W. Freudiger, W. Min, B. G. Saar, S. Lu, G. R. Holtom, C. He, J. C. Tsai, J. X. Kang, and X. S. Xie, "Label-Free Biomedical Imaging with High Sensitivity by Stimulated Raman Scattering Microscopy," *Science*, vol. 322, pp. 1857–1861, Dec. 2008.

[127] Y. Ozeki, F. Dake, S. 'ichiro Kajiyama, K. Fukui, and K. Itoh, "Analysis and experimental assessment of the sensitivity of stimulated Raman scattering microscopy," *Optics Express*, vol. 17, p. 3651, Mar. 2009.

[128] P. Nandakumar, A. Kovalev, and A. Volkmer, "Vibrational imaging based on stimulated Raman scattering microscopy," *New Journal of Physics*, vol. 11, no. 3, p. 033026, 2009.

[129] B. G. Saar, C. W. Freudiger, J. Reichman, C. M. Stanley, G. R. Holtom, and X. S. Xie, "Video-Rate Molecular Imaging in Vivo with Stimulated Raman Scattering," *Science*, vol. 330, pp. 1368–1370, Dec. 2010.

[130] C. H. Camp Jr, Y. J. Lee, J. M. Heddleston, C. M. Hartshorn, A. R. H. Walker, J. N. Rich, J. D. Lathia, and M. T. Cicerone, "High-speed coherent Raman fingerprint imaging of biological tissues," *Nature Photonics*, vol. 8, pp. 627–634, Aug. 2014.

[131] M. Müller and J. M. Schins, "Imaging the Thermodynamic State of Lipid Membranes with Multiplex CARS Microscopy," *The Journal of Physical Chemistry B*, vol. 106, pp. 3715–3723, Apr. 2002.

[132] J.-x. Cheng, A. Volkmer, L. D. Book, and X. S. Xie, "Multiplex Coherent Anti-Stokes Raman Scattering Microspectroscopy and Study of Lipid Vesicles," *The Journal of Physical Chemistry B*, vol. 106, pp. 8493–8498, Aug. 2002.

[133] M. Hashimoto, T. Araki, and S. Kawata, "Molecular vibration imaging in the fingerprint region by use of coherent anti-Stokes Raman scattering microscopy with a collinear configuration," *Optics Letters*, vol. 25, p. 1768, Dec. 2000.

[134] Y. Ozeki, W. Umemura, Y. Otsuka, S. Satoh, H. Hashimoto, K. Sumimura, N. Nishizawa, K. Fukui, and K. Itoh, "High-speed molecular spectral imaging of tissue with stimulated Raman scattering," *Nature Photonics*, vol. 6, pp. 845–851, Dec. 2012.

[135] I. Weissflog, N. Vogler, D. Akimov, A. Dellith, D. Schachtschabel, A. Svatos, W. Boland, B. Dietzek, and J. Popp, "Toward in Vivo Chemical Imaging of Epicuticular Waxes," *Plant Physiology*, vol. 154, pp. 604–610, Oct. 2010.

[136] J. C. Mansfield, G. R. Littlejohn, M. P. Seymour, R. J. Lind, S. Perfect, and J. Moger, "Label-free Chemically Specific Imaging in Planta with Stimulated Raman Scattering Microscopy," *Analytical Chemistry*, vol. 85, pp. 5055–5063, May 2013.

[137] R. C. Burruss, A. D. Slepkov, A. F. Pegoraro, and A. Stolow, "Unraveling the complexity of deep gas accumulations with three-dimensional multimodal CARS microscopy," *Geology*, vol. 40, pp. 1063–1066, Dec. 2012.

[138] Y. Wang, C.-Y. Lin, A. Nikolaenko, V. Raghunathan, and E. O. Potma, "Four-wave mixing microscopy of nanostructures," *Advances in Optics and Photonics*, vol. 3, p. 1, Mar. 2011.

[139] Y. Fu, W. Sun, Y. Shi, R. Shi, and J.-X. Cheng, "Glutamate excitotoxicity inflicts paranodal myelin splitting and retraction.," *PLoS One*, vol. 4, no. 8, p. e6705, 2009.

[140] T. B. Huff, Y. Shi, W. Sun, W. Wu, R. Shi, and J.-X. Cheng, "Real-time CARS imaging reveals a calpain-dependent pathway for paranodal myelin retraction during high-frequency stimulation.," *PLoS One*, vol. 6, no. 3, p. e17176, 2011.

[141] H. Wang, Y. Fu, P. Zickmund, R. Shi, and J.-X. Cheng, "Coherent anti-stokes Raman scattering imaging of axonal myelin in live spinal tissues.," *Biophys J*, vol. 89, pp. 581–591, July 2005.

[142] D. A. Kirschner and A. E. Blaurock, "Organization, Phylogenetic Variations and Dynamic Transitions of Myelin," in *Myelin: Biology and Chemistry* (R. E. Martenson, ed.), CRC Press, Feb. 1992.

[143] R. Virchow, "Ueber das ausgebreitete Vorkommen einer dem Nervenmark analogen Substanz in den thierischen Geweben," *Archiv für pathologische Anatomie und Physiologie und für klinische Medicin*, vol. 6, pp. 562–572, Dec. 1854.

[144] R. H. Quarles, W. B. Macklin, and P. Morell, "Myelin formation, structure and biochemistry," in *Basic Neurochemistry: Molecular, Cellular and Medical Aspects* (G. J. Siegel, R. W. Albers, S. T. Brady, and D. L. Price, eds.), New York: Academic Press Elsevier, seventh edition ed., 2006.

[145] C. Hildebrand and R. Hahn, "Relation between myelin sheath thickness and axon size in spinal cord white matter of some vertebrate species," *Journal of the Neurological Sciences*, vol. 38, pp. 421–434, Oct. 1978.

[146] A. J. Barkovich, "Concepts of Myelin and Myelination in Neuroradiology," *American Journal of Neuroradiology*, vol. 21, pp. 1099–1109, Jan. 2000.

[147] G. Gopalakrishnan, A. Awasthi, W. Belkaid, O. De Faria, D. Liazoghli, D. R. Colman, and A. S. Dhaunchak, "Lipidome and proteome map of myelin membranes," *Journal of Neuroscience Research*, vol. 91, pp. 321–334, Mar. 2013.

[148] R. H. Quarles, P. Morell, and H. F. McFarland, "Diseases Involving Myelin," in *Basic Neurochemistry: Molecular, Cellular and Medical Aspects* (G. J. Siegel, R. W. Albers, S. T. Brady, and D. L. Price, eds.), New York: Academic Press Elsevier, seventh edition ed., 2006.

[149] C. M. Poser, "Leukodystrophy and the concept of dysmyelination," *Archives of Neurology*, vol. 4, pp. 323–332, Mar. 1961.

[150] S. Love, "Demyelinating diseases," *Journal of Clinical Pathology*, vol. 59, pp. 1151–1159, Nov. 2006.

[151] J. Azulay, "Diagnostic des polyneuropathies axonales chroniques : les polyradiculonévrites chroniques méconnues," *Revue Neurologique*, vol. 162, no. 12, pp. 1292–1295, 2006.

[152] J. H. Stone, "Polyarteritis Nodosa," *JAMA*, vol. 288, pp. 1632–1639, Oct. 2002.

[153] V. Crespi, G. M. Fabrizi, P. Mandich, D. Pareyson, F. Salvi, L. Santoro, A. Schenone, and F. Taroni, "Guidelines for the diagnosis of Charcot-Marie-Tooth disease and related neuropathies," *The Italian Journal of Neurological Sciences*, vol. 20, pp. 207–216, Oct. 1999.

[154] L. C. Schmued, "A rapid, sensitive histochemical stain for myelin in frozen brain sections.," *Journal of Histochemistry & Cytochemistry*, vol. 38, pp. 717–720, Jan. 1990.

[155] C. W. M. Adams, "A histochemical method for the simultaneous demonstration of normal and degenerating myelin," *The Journal of Pathology and Bacteriology*, vol. 77, pp. 648–650, Apr. 1959.

[156] C. W. M. Adams, O. B. Bayliss, J. F. Hallpike, and D. R. Turner, "Histochemistry of Myelin—XII Anionic Staining of Myelin Basic Proteins for Histology, Electrophoresis and Electron Microscopy," *Journal of Neurochemistry*, vol. 18, pp. 389–394, Mar. 1971.

[157] Z. Xiang, E. E. Nesterov, J. Skoch, T. Lin, B. T. Hyman, T. M. Swager, B. J. Bacskai, and S. A. Reeves, "Detection of myelination using a novel histological probe," *Journal of Histochemistry & Cytochemistry*, vol. 53, no. 12, pp. 1511–1516, 2005.

[158] C. Wang, D. C. Popescu, C. Wu, J. Zhu, W. Macklin, and Y. Wang, "In Situ Fluorescence Imaging of Myelination," *Journal of Histochemistry and Cytochemistry*, vol. 58, pp. 611–621, July 2010.

[159] F. S. Sjöstrand, "The lamellated structure of the nerve myelin sheath as revealed by high resolution electron microscopy," *Experientia*, vol. 9, pp. 68–69, Feb. 1953.

[160] H. Fernández-morán and J. B. Finean, "Electron Microscope and Low-Angle X-Ray Diffraction Studies of the Nerve Myelin Sheath," *The Journal of Biophysical and Biochemical Cytology*, vol. 3, pp. 725–748, Sept. 1957.

[161] F. Knerlich-Lukoschus, B. von der Ropp-Brenner, R. Lucius, H. M. Mehdorn, and J. Held-Feindt, "Chemokine expression in the white matter spinal cord precursor niche after force-defined spinal cord contusion injuries in adult rats," *Glia*, vol. 58, pp. 916–931, June 2010.

[162] W. Guo, E. L. Crossey, L. Zhang, S. Zucca, O. L. George, C. F. Valenzuela, and X. Zhao, "Alcohol Exposure Decreases CREB Binding Protein Expression and Histone Acetylation in the Developing Cerebellum," *PLoS ONE*, vol. 6, May 2011.

[163] M. van der Knaap and J. Valk, *Magnetic Resonance of Myelination and Myelin Disorders*. Springer US, 2005.

[164] S. C. L. Deoni, E. Mercure, A. Blasi, D. Gasston, A. Thomson, M. Johnson, S. C. R. Williams, and D. G. M. Murphy, "Mapping Infant Brain Myelination with Magnetic Resonance Imaging," *The Journal of Neuroscience*, vol. 31, pp. 784–791, Dec. 2011.

[165] C. Laule, I. M. Vavasour, S. H. Kolind, D. K. B. Li, T. L. Traboulsee, G. R. W. Moore, and A. L. MacKay, "Magnetic Resonance Imaging of Myelin," *Neurotherapeutics*, vol. 4, pp. 460–484, July 2007.

[166] C. L. Sommer, S. Brandner, P. J. Dyck, Y. Harati, C. LaCroix, M. Lammens, L. Magy, S. I. Mellgren, M. Morbin, C. Navarro, H. C. Powell, A. E. Schenone, E. Tan, A. Urtizberea, and J. Weis, "Peripheral Nerve Society Guideline on processing and evaluation of nerve biopsies," *Journal of the Peripheral Nervous System*, vol. 15, pp. 164–175, Sept. 2010.

[167] Y. Fu, H. Wang, T. B. Huff, R. Shi, and J.-X. Cheng, "Coherent anti-stokes Raman scattering imaging of myelin degradation reveals a calcium-dependent pathway in lyso-PtdCho-induced demyelination," *Journal of neuroscience research*, vol. 85, no. 13, pp. 2870–2881, 2007.

[168] H. Ouyang, W. Sun, Y. Fu, J. Li, J.-X. Cheng, E. Nauman, and R. Shi, "Compression induces acute demyelination and potassium channel exposure in spinal cord.," *J Neurotrauma*, vol. 27, pp. 1109–1120, June 2010.

[169] Y. Fu, T. J. Frederick, T. B. Huff, G. E. Goings, S. D. Miller, and J.-X. Cheng, "Paranodal myelin retraction in relapsing experimental autoimmune encephalomyelitis visualized by coherent anti-Stokes Raman scattering microscopy.," *J Biomed Opt*, vol. 16, p. 106006, Oct. 2011.

[170] J. Imitola, D. Côté, S. Rasmussen, X. S. Xie, Y. Liu, T. Chitnis, R. L. Sidman, C. P. Lin, and S. J. Khoury, "Multimodal coherent anti-Stokes Raman scattering microscopy reveals microglia-associated myelin and axonal dysfunction in multiple sclerosis-like lesions in mice.," *J Biomed Opt*, vol. 16, p. 021109, Feb. 2011.

[171] S. Bégin, E. Bélanger, S. Laffray, B. Aubé, E. Chamma, J. Bélisle, S. Lacroix, Y. De Koninck, and D. Côté, "Local assessment of myelin health in a multiple sclerosis mouse model using a 2D Fourier transform approach.," *Biomed Opt Express*, vol. 4, no. 10, pp. 2003–2014, 2013.

[172] Y. Shi, D. Zhang, T. B. Huff, X. Wang, R. Shi, X.-M. Xu, and J.-X. Cheng, "Longitudinal in vivo coherent anti-Stokes Raman scattering imaging of demyelination and remyelination in injured spinal cord.," *J Biomed Opt*, vol. 16, p. 106012, Oct. 2011.

[173] Y. Fu, T. M. Talavage, and J.-X. Cheng, "New imaging techniques in the diagnosis of multiple sclerosis.," *Expert Opin Med Diagn*, vol. 2, pp. 1055–1065, Sept. 2008.

[174] T. Meyer, M. Chemnitz, M. Baumgartl, T. Gottschall, T. Pascher, C. Matthäus, B. F. M. Romeike, B. R. Brehm, J. Limpert, A. Tünnermann, M. Schmitt, B. Dietzek, and J. Popp, "Expanding multimodal microscopy by high spectral resolution coherent anti-Stokes Raman scattering imaging for clinical disease diagnostics.," *Anal Chem*, vol. 85, pp. 6703–6715, July 2013.

[175] E. Bélanger, S. Bégin, S. Laffray, Y. De Koninck, R. Vallée, and D. Côté, "Quantitative myelin imaging with coherent anti-Stokes Raman scattering microscopy: Alleviating the excitation polarization dependence with circularly polarized laser beams.," *Opt Express*, vol. 17, pp. 18419–18432, Oct. 2009.

[176] Y. Fu, T. B. Huff, H.-W. Wang, H. Wang, and J.-X. Cheng, "Ex vivo and in vivo imaging of myelin fibers in mouse brain by coherent anti-Stokes Raman scattering microscopy.," *Opt Express*, vol. 16, pp. 19396–19409, Nov. 2008.

[177] C.-B. Juang, L. Finzi, and C. J. Bustamante, "Design and application of a computer-controlled confocal scanning differential polarization microscope," *Review of Scientific Instruments*, vol. 59, pp. 2399–2408, Nov. 1988.

[178] G. Steinbach, I. Pomozi, O. Zsiros, L. Menczel, and G. Garab, "Imaging anisotropy using differential polarization laser scanning confocal microscopy," *Acta Histochemica*, vol. 111, pp. 317–326, July 2009.

[179] A. Kress, X. Wang, H. Ranchon, J. Savatier, H. Rigneault, P. Ferrand, and S. Brasselet, "Mapping the Local Organization of Cell Membranes Using Excitation-Polarization-Resolved Confocal Fluorescence Microscopy," *Biophysical Journal*, vol. 105, pp. 127–136, July 2013.

[180] A. Gasecka, T.-J. Han, C. Favard, B. R. Cho, and S. Brasselet, "Quantitative Imaging of Molecular Order in Lipid Membranes Using Two-Photon Fluorescence Polarimetry," *Biophysical Journal*, vol. 97, pp. 2854–2862, Nov. 2009.

[181] M. Savoini, X. Wu, M. Celebrano, J. Ziegler, P. Biagioni, S. C. J. Meskers, L. Duò, B. Hecht, and M. Finazzi, "Circular Dichroism Probed by Two-Photon Fluorescence Microscopy in Enantiopure Chiral Polyfluorene Thin Films," *Journal of the American Chemical Society*, vol. 134, pp. 5832–5835, Apr. 2012.

[182] P. Ferrand, P. Gasecka, A. Kress, X. Wang, F.-Z. Bioud, J. Duboisset, and S. Brasselet, "Ultimate Use of Two-Photon Fluorescence Microscopy to Map Orientational Behavior of Fluorophores," *Biophysical Journal*, vol. 106, pp. 2330–2339, June 2014.

[183] F. Tiaho, G. Recher, and D. Rouède, "Estimation of helical angles of myosin and collagen by second harmonic generation imaging microscopy," *Optics Express*, vol. 15, no. 19, p. 12286, 2007.

[184] I. Gusachenko, G. Latour, and M.-C. Schanne-Klein, "Polarization-resolved Second Harmonic microscopy in anisotropic thick tissues," *Optics Express*, vol. 18, p. 19339, Aug. 2010.

[185] J. Duboisset, D. Aït-Belkacem, M. Roche, H. Rigneault, and S. Brasselet, "Generic model of the molecular orientational distribution probed by polarization-resolved second-harmonic generation," *Physical Review A*, vol. 85, p. 043829, Apr. 2012.

[186] N. Mazumder, J. Qiu, M. R. Foreman, C. M. Romero, C.-W. Hu, H.-R. Tsai, P. Török, and F.-J. Kao, "Polarization-resolved second harmonic generation microscopy with a four-channel Stokes-polarimeter," *Optics Express*, vol. 20, pp. 14090–14099, June 2012.

[187] V. K. Gupta and J. A. Kornfield, "Polarization modulation laser scanning microscopy: A powerful tool to image molecular orientation and order," *Review of Scientific Instruments*, vol. 65, pp. 2823–2828, Sept. 1994.

[188] E. O. Potma and X. S. Xie, "Detection of single lipid bilayers with coherent anti-Stokes Raman scattering (CARS) microscopy," *Journal of Raman Spectroscopy*, vol. 34, pp. 642–650, Sept. 2003.

[189] C. Zhang, J. Wang, J. Jasensky, and Z. Chen, "Molecular Orientation Analysis of Alkyl Methylene Groups from Quantitative Coherent Anti-Stokes Raman Scattering Spectroscopy," *The Journal of Physical Chemistry Letters*, vol. 6, pp. 1369–1374, Apr. 2015.

[190] Y. J. Lee, "Determination of 3D molecular orientation by concurrent polarization analysis of multiple Raman modes in broadband CARS spectroscopy," *Optics Express*, vol. 23, p. 29279, Nov. 2015.

[191] J.-X. Cheng, S. Pautot, D. A. Weitz, and X. S. Xie, "Ordering of water molecules between phospholipid bilayers visualized by coherent anti-Stokes Raman scattering microscopy," *Proceedings of the National Academy of Sciences*, vol. 100, pp. 9826–9830, Aug. 2003.

[192] A. D. Slepkov, A. Ridsdale, A. F. Pegoraro, D. J. Moffatt, and A. Stolow, "Multimodal CARS microscopy of structured carbohydrate biopolymers," *Biomedical Optics Express*, vol. 1, p. 1347, Dec. 2010.

[193] M. Zimmerley, R. Younger, T. Valenton, D. C. Oertel, J. L. Ward, and E. O. Potma, "Molecular Orientation in Dry and Hydrated Cellulose Fibers: A Coherent Anti-Stokes Raman Scattering Microscopy Study," *The Journal of Physical Chemistry B*, vol. 114, pp. 10200–10208, Aug. 2010.

[194] E. Bélanger, R. Turcotte, A. Daradich, G. Sadetsky, P. Gravel, K. Bachand, Y. De Koninck, and D. C. Côté, "Maintaining polarization in polarimetric multiphoton microscopy," *Journal of Biophotonics*, vol. 8, pp. 884–888, Nov. 2015.

[195] F.-Z. Bioud, P. Gasecka, P. Ferrand, H. Rigneault, J. Duboisset, and S. Brasselet, "Structure of molecular packing probed by polarization-resolved nonlinear four-wave mixing and coherent anti-Stokes Raman-scattering microscopy," *Physical Review A*, vol. 89, p. 013836, Jan. 2014.

[196] F. Munhoz, H. Rigneault, and S. Brasselet, "Polarization-resolved four-wave mixing microscopy for structural imaging in thick tissues," *JOSA B*, vol. 29, no. 6, pp. 1541–1550, 2012.

[197] J. Duboisset, P. Berto, P. Gasecka, F.-Z. Bioud, P. Ferrand, H. Rigneault, and S. Brasselet, "Molecular Orientational Order Probed by Coherent Anti-Stokes Raman Scattering (CARS) and Stimulated Raman Scattering (SRS) Microscopy: A Spectral Comparative Study," *The Journal of Physical Chemistry B*, vol. 119, pp. 3242–3249, Feb. 2015.

[198] P. Gasecka, *Polarization Resolved Nonlinear Multimodal Microscopy in Lipids: From Model Membranes to Myelin in Tissues.* PhD thesis, Université Aix-Marseille, Dec. 2015.

[199] C. Cleff, A. Gasecka, P. Ferrand, H. Rigneault, S. Brasselet, and J. Duboisset, "Direct imaging of molecular symmetry by coherent anti-stokes Raman scattering," *Nature Communications*, vol. 7, p. 11562, May 2016.

[200] N. Corporation, "Supercontinuum Generation in SCG-800 Photonic Crystal Fiber," tech. rep., Technology and Applications Center Newport Corporation, 2006.

[201] Y. J. Lee, S. H. Parekh, Y. H. Kim, and M. T. Cicerone, "Optimized continuum from a photonic crystal fiber for broadband time-resolved coherent anti-Stokes Raman scattering," *Optics Express*, vol. 18, p. 4371, Mar. 2010.

[202] G. Ciofani, S. Danti, S. Moscato, L. Albertazzi, D. D'Alessandro, D. Dinucci, F. Chiellini, M. Petrini, and A. Menciassi, "Preparation of stable dispersion of barium titanate nanoparticles: Potential applications in biomedicine," *Colloids and Surfaces B: Biointerfaces*, vol. 76, pp. 535–543, Apr. 2010.

[203] A. Rocca, A. Marino, V. Rocca, S. Moscato, G. de Vito, V. Piazza, B. Mazzolai, V. Mattoli, T. J. Ngo-Anh, and G. Ciofani, "Barium titanate nanoparticles and hypergravity stimulation improve differentiation of mesenchymal stem cells into osteoblasts," *International Journal of Nanomedicine*, vol. 10, pp. 433–445, Jan. 2015.

[204] A. Marino, J. Barsotti, G. de Vito, C. Filippeschi, B. Mazzolai, V. Piazza, M. Labardi, V. Mattoli, and G. Ciofani, "Two-Photon Lithography of 3D Nanocomposite Piezoelectric Scaffolds for Cell Stimulation," *ACS Applied Materials & Interfaces*, vol. 7, pp. 25574–25579, Nov. 2015.

[205] G. de Vito, A. Bifone, and V. Piazza, "Rotating-polarization CARS microscopy: Combining chemical and molecular orientation sensitivity," *Optics Express*, vol. 20, no. 28, pp. 29369–29377, 2012.

[206] C. Shang and H. Hsu, "The spatial symmetric forms of third-order nonlinear susceptibility," *IEEE Journal of Quantum Electronics*, vol. 23, pp. 177–179, Feb. 1987.

[207] G. de Vito, I. Tonazzini, M. Cecchini, and V. Piazza, "RP-CARS: Label-free optical readout of the myelin intrinsic healthiness," *Optics Express*, vol. 22, p. 13733, June 2014.

[208] T. Huff and J.-X. Cheng, "In vivo coherent anti-Stokes Raman scattering imaging of sciatic nerve tissue," *Journal of Microscopy*, vol. 225, pp. 175–182, Feb. 2007.

[209] I. Rocha-Mendoza, W. Langbein, and P. Borri, "Coherent anti-Stokes Raman microspectroscopy using spectral focusing with glass dispersion," *Applied Physics Letters*, vol. 93, p. 201103, Nov. 2008.

[210] E. Gershgoren, R. A. Bartels, J. T. Fourkas, R. Tobey, M. M. Murnane, and H. C. Kapteyn, "Simplified setup for high-resolution spectroscopy that uses ultrashort pulses," *Optics Letters*, vol. 28, p. 361, Mar. 2003.

[211] T. Hellerer, A. M. K. Enejder, and A. Zumbusch, "Spectral focusing: High spectral resolution spectroscopy with broad-bandwidth laser pulses," *Applied Physics Letters*, vol. 85, pp. 25–27, July 2004.

[212] G. de Vito and V. Piazza, "Fast signal analysis in Rotating-Polarization CARS microscopy," *Optical Data Processing and Storage*, vol. 1, pp. 1–5, Feb. 2014.

[213] P. Schön, F. Munhoz, A. Gasecka, S. Brustlein, and S. Brasselet, "Polarization distortion effects in polarimetric two-photon microscopy," *Optics Express*, vol. 16, p. 20891, Dec. 2008.

[214] H. Kang, B. Jia, and M. Gu, "Polarization characterization in the focal volume of high numerical aperture objectives," *Optics Express*, vol. 18, p. 10813, May 2010.

[215] G. de Vito, A. Canta, P. Marmiroli, and V. Piazza, "A large-field polarization-resolved laser scanning microscope: Applications to CARS imaging," *Journal of Microscopy*, vol. 260, no. 2, pp. 194–199, 2015.

[216] V. Piazza, G. de Vito, E. Farrokhtakin, G. Ciofani, and V. Mattoli, "Femtosecond laser pulse characterization and optimization for CARS microscopy," *PLOS ONE*, 2016.

[217] R. Trebino, K. W. DeLong, D. N. Fittinghoff, J. N. Sweetser, M. A. Krumbügel, B. A. Richman, and D. J. Kane, "Measuring ultrashort laser pulses in the time-frequency domain using frequency-resolved optical gating," *Review of Scientific Instruments*, vol. 68, pp. 3277–3295, Sept. 1997.

[218] D. J. Kane and R. Trebino, "Single-shot measurement of the intensity and phase of an arbitrary ultrashort pulse by using frequency-resolved optical gating," *Optics Letters*, vol. 18, p. 823, May 1993.

[219] E. FarrokhTakin, G. Ciofani, G. L. Puleo, G. de Vito, C. Filippeschi, B. Mazzolai, V. Piazza, and V. Mattoli, "Barium titanate core-gold shell nanoparticles for hyperthermia treatments," *International Journal of Nanomedicine*, vol. 8, pp. 2319–2331, 2013.

[220] E. FarrokhTakin, G. Ciofani, M. Gemmi, V. Piazza, B. Mazzolai, and V. Mattoli, "Synthesis and characterization of new barium titanate core–gold shell nanoparticles," *Colloids and Surfaces A: Physicochemical and Engineering Aspects*, vol. 415, pp. 247–254, Dec. 2012.

[221] K. P. Knutsen, B. M. Messer, R. M. Onorato, and R. J. Saykally, "Chirped Coherent Anti-Stokes Raman Scattering for High Spectral Resolution Spectroscopy and Chemically Selective Imaging," *The Journal of Physical Chemistry B*, vol. 110, pp. 5854–5864, Mar. 2006.

[222] G. Ayala, P. Carmona, M. de Cózar, and J. Monreal, "Vibrational spectra and structure of myelin membranes," *European Biophysics Journal*, vol. 14, pp. 219–225, Feb. 1987.

[223] M. Pézolet and D. Georgescauld, "Raman spectroscopy of nerve fibers. A study of membrane lipids under steady state conditions," *Biophysical Journal*, vol. 47, pp. 367–372, Mar. 1985.

[224] P. Rao and B. Segal, "Experimental Autoimmune Encephalomyelitis," in *Autoimmunity* (A. Perl and A. P. MD, eds.), no. 102 in Methods in Molecular Medicine™, pp. 363–375, Humana Press, Jan. 2004.

[225] W. Rasband, "ImageJ." http://imagej.nih.gov/ij/, 1997-2016. U. S. National Institutes of Health, Bethesda, Maryland, USA.

[226] G. Paxinos, *The Mouse Brain in Stereotaxic Coordinates*. Academic press, 2004.

[227] S. Bégin, O. Dupont-Therrien, E. Bélanger, A. Daradich, S. Laffray, Y. De Koninck, and D. C. Côté, "Automated method for the segmentation and morphometry of nerve fibers in large-scale CARS images of spinal cord tissue," *Biomedical Optics Express*, vol. 5, p. 4145, Dec. 2014.

[228] T. Duval, A. Gasecka, P. Pouliot, D. Côté, N. Stikov, and J. Cohen-Adad, "Validation of MRI microstructure measurements with Coherent Anti-Stokes Raman Scattering (CARS)," (Toronto), 2015.

[229] R. E. Martenson, *Myelin*. CRC Press, Feb. 1992.

[230] T. L. Mazely and W. M. H. Iii, "Third-order susceptibility tensors of partially ordered systems," *The Journal of Chemical Physics*, vol. 87, pp. 1962–1966, Aug. 1987.

[231] S. M. HALL and N. Gregson, "The in vivo and ultrastructural effects of injection of lysophosphatidyl choline into myelinated peripheral nerve fibres of the adult mouse," *Journal of Cell Science*, vol. 9, no. 3, pp. 769–789, 1971.

[232] T. Coetzee, N. Fujita, J. Dupree, R. Shi, A. Blight, K. Suzuki, K. Suzuki, and B. Popko, "Myelination in the Absence of Galactocerebroside and Sulfatide: Normal Structure with Abnormal Function and Regional Instability," *Cell*, vol. 86, pp. 209–219, July 1996.

[233] C. O. Hanemann, A. A. W. M. Gabreëls-Festen, and P. De Jonghe, "Axon damage in CMT due to mutation in myelin protein Po," *Neuromuscular Disorders*, vol. 11, pp. 753–756, Nov. 2001.

[234] S. P. J. Fancy, S. E. Baranzini, C. Zhao, D.-I. Yuk, K.-A. Irvine, S. Kaing, N. Sanai, R. J. M. Franklin, and D. H. Rowitch, "Dysregulation of the Wnt pathway inhibits timely myelination and remyelination in the mammalian CNS," *Genes & Development*, vol. 23, pp. 1571–1585, Jan. 2009.

[235] National Library of Medicine, "Krabbe Disease." `http://ghr.nlm.nih.gov/condition/krabbe-disease`, June 2015.

[236] D. A. Wenger, M. A. Rafi, and P. Luzi, "Molecular genetics of Krabbe disease (globoid cell leukodystrophy): Diagnostic and clinical implications," *Human Mutation*, vol. 10, pp. 268–279, 1997.

[237] K. Suzuki, "Twenty Five Years of the "Psychosine Hypothesis": A Personal Perspective of its History and Present Status," *Neurochemical Research*, vol. 23, pp. 251–259, Mar. 1998.

[238] V. Voccoli, I. Tonazzini, G. Signore, M. Caleo, and M. Cecchini, "Role of extracellular calcium and mitochondrial oxygen species in psychosine-induced oligodendrocyte cell death," *Cell Death & Disease*, vol. 5, p. e1529, Nov. 2014.

[239] A. B. White, M. I. Givogri, A. Lopez-Rosas, H. Cao, R. van Breemen, G. Thinakaran, and E. R. Bongarzone, "Psychosine Accumulates in Membrane Microdomains in the Brain of Krabbe Patients, Disrupting the Raft Architecture," *The Journal of Neuroscience*, vol. 29, pp. 6068–6077, May 2009.

[240] J. A. Hawkins-Salsbury, A. R. Parameswar, X. Jiang, P. H. Schlesinger, E. Bongarzone, D. S. Ory, A. V. Demchenko, and M. S. Sands, "Psychosine, the cytotoxic sphingolipid that accumulates in globoid cell leukodystrophy, alters membrane architecture," *Journal of Lipid Research*, vol. 54, pp. 3303–3311, Dec. 2013.

[241] C. A. Teixeira, C. O. Miranda, V. F. Sousa, T. E. Santos, A. R. Malheiro, M. Solomon, G. H. Maegawa, P. Brites, and M. M. Sousa, "Early axonal loss accompanied by impaired endocytosis, abnormal axonal transport, and decreased microtubule stability occur in the model of Krabbe's disease," *Neurobiology of Disease*, vol. 66, pp. 92–103, June 2014.

[242] G. Pannuzzo, V. Cardile, E. Costantino-Ceccarini, E. Alvares, D. Mazzone, and V. Perciavalle, "A galactose-free diet enriched in soy isoflavones and antioxidants results in delayed onset of symptoms of Krabbe disease in twitcher mice," *Molecular Genetics and Metabolism*, vol. 100, pp. 234–240, July 2010.

[243] P. Formichi, E. Radi, C. Battisti, A. Pasqui, G. Pompella, P. E. Lazzerini, F. Laghi-Pasini, A. Leonini, A. Di Stefano, and A. Federico, "Psychosine-induced apoptosis and cytokine activation in immune peripheral cells of Krabbe patients," *Journal of Cellular Physiology*, vol. 212, pp. 737–743, Sept. 2007.

[244] S. Giri, M. Khan, R. Rattan, I. Singh, and A. K. Singh, "Krabbe disease: Psychosine-mediated activation of phospholipase A2 in oligodendrocyte cell death," *Journal of Lipid Research*, vol. 47, pp. 1478–1492, Jan. 2006.

[245] E. Haq, S. Giri, I. Singh, and A. K. Singh, "Molecular mechanism of psychosine-induced cell death in human oligodendrocyte cell line," *Journal of Neurochemistry*, vol. 86, pp. 1428–1440, Sept. 2003.

[246] M. Khan, E. Haq, S. Giri, I. Singh, and A. K. Singh, "Peroxisomal participation in psychosine-mediated toxicity: Implications for Krabbe's disease," *Journal of Neuroscience Research*, vol. 80, pp. 845–854, June 2005.

[247] E. Haq, M. A. Contreras, S. Giri, I. Singh, and A. K. Singh, "Dysfunction of peroxisomes in twitcher mice brain: A possible mechanism of psychosine-induced disease," *Biochemical and Biophysical Research Communications*, vol. 343, pp. 229–238, Apr. 2006.

[248] L. Cantuti-Castelvetri, E. Maravilla, M. Marshall, T. Tamayo, L. D'auria, J. Monge, J. Jeffries, T. Sural-Fehr, A. Lopez-Rosas, G. Li, K. Garcia, R. van Breemen, C. Vite, J. Garcia, and E. R. Bongarzone, "Mechanism of Neuromuscular Dysfunction in Krabbe Disease," *The Journal of Neuroscience*, vol. 35, pp. 1606–1616, Jan. 2015.

[249] K. Ijichi, G. D. Brown, C. S. Moore, J.-P. Lee, P. N. Winokur, R. Pagarigan, E. Y. Snyder, E. R. Bongarzone, and S. J. Crocker, "MMP-3 mediates psychosine-induced globoid cell formation: Implications for leukodystrophy pathology," *Glia*, vol. 61, pp. 765–777, May 2013.

[250] L. Cantuti Castelvetri, M. I. Givogri, H. Zhu, B. Smith, A. Lopez-Rosas, X. Qiu, R. van Breemen, and E. R. Bongarzone, "Axonopathy is a compounding factor in the pathogenesis of Krabbe disease," *Acta Neuropathologica*, vol. 122, pp. 35–48, Mar. 2011.

[251] A. Ricca, N. Rufo, S. Ungari, F. Morena, S. Martino, W. Kulik, V. Alberizzi, A. Bolino, F. Bianchi, U. Del Carro, A. Biffi, and A. Gritti, "Combined gene/cell therapies provide long-term and pervasive rescue of multiple pathological symptoms in a murine model of globoid cell leukodystrophy," *Human Molecular Genetics*, vol. 24, pp. 3372–3389, June 2015.

[252] A. Lattanzi, C. Salvagno, C. Maderna, F. Benedicenti, F. Morena, W. Kulik, L. Naldini, E. Montini, S. Martino, and A. Gritti, "Therapeutic benefit of lentiviral-mediated neonatal intracerebral gene therapy in a mouse model of globoid cell leukodystrophy," *Human Molecular Genetics*, vol. 23, pp. 3250–3268, June 2014.

[253] B. A. Scruggs, X. Zhang, A. C. Bowles, P. A. Gold, J. A. Semon, J. M. Fisher-Perkins, S. Zhang, R. W. Bonvillain, L. Myers, S. C. Li, A. V. Kalueff, and B. A. Bunnell, "Multipotent Stromal Cells Alleviate Inflammation, Neuropathology, and Symptoms Associated with Globoid Cell Leukodystrophy in the Twitcher Mouse," *STEM CELLS*, vol. 31, pp. 1523–1534, Aug. 2013.

[254] K. Suzuki, "Globoid Cell Leukodystrophy (Krabbe's Disease): Update," *Journal of Child Neurology*, vol. 18, pp. 595–603, Jan. 2003.

[255] K. Suzuki and K. Suzuki, "The Twitcher Mouse: A Model for Krabbe Disease and for Experimental Therapies," *Brain Pathology*, vol. 5, pp. 249–258, July 1995.

[256] K. Tanaka, H. Nagara, T. Kobayashi, and I. Goto, "The twitcher mouse: Accumulation of galactosylsphingosine and pathology of the sciatic nerve," *Brain Research*, vol. 454, pp. 340–346, June 1988.

[257] J. M. Jacobs, F. Scaravilli, and F. T. De Aranda, "The pathogenesis of globoid cell leucodystrophy in peripheral nerve of the mouse mutant twitcher," *Journal of the Neurological Sciences*, vol. 55, pp. 285–304, Sept. 1982.

[258] B. Smith, F. Galbiati, L. Cantuti Castelvetri, M. I. Givogri, A. Lopez-Rosas, and E. R. Bongarzone, "Peripheral neuropathy in the Twitcher mouse involves the activation of axonal caspase 3," *ASN NEURO*, vol. 3, pp. 213–222, Oct. 2011.

[259] G. de Vito, V. Cappello, I. Tonazzini, M. Cecchini, and V. Piazza, "RP-CARS reveals molecular spatial order anomalies in myelin of an animal model of Krabbe disease," *Journal of Biophotonics*, Mar. 2016.

[260] F. Galbiati, M. Givogri, L. Cantuti, A. Lopez Rosas, H. Cao, R. van Breemen, and E. Bongarzone, "Combined hematopoietic and lentiviral gene-transfer therapies in newborn Twitcher mice reveal contemporaneous neurodegeneration and demyelination in Krabbe disease," *Journal of Neuroscience Research*, vol. 87, pp. 1748–1759, June 2009.

[261] P. W. Laird, A. Zijderveld, K. Linders, M. A. Rudnicki, R. Jaenisch, and A. Berns, "Simplified mammalian DNA isolation procedure.," *Nucleic Acids Research*, vol. 19, p. 4293, Aug. 1991.

[262] N. Sakai, K. Inui, N. Tatsumi, H. Fukushima, T. Nishigaki, M. Taniike, J. Nishimoto, H. Tsukamoto, I. Yanagihara, K. Ozono, and S. Okada, "Molecular cloning and expression of cDNA for murine galactocerebrosidase and mutation analysis of the twitcher mouse, a model of Krabbe's disease," *Journal of Neurochemistry*, vol. 66, pp. 1118–1124, Mar. 1996.

[263] T. W. Ridler and S. Calvard, "Picture thresholding using an iterative selection method," *IEEE transactions on Systems, Man and Cybernetics*, vol. 8, no. 8, pp. 630–632, 1978.

[264] R Core Team, *R: A Language and Environment for Statistical Computing*. Vienna, Austria: R Foundation for Statistical Computing, 2015.

[265] K. V. Mardia, J. M. Bibby, and J. T. Kent, *Multivariate Analysis*. Probability and mathematical statistics, London; New York: Academic Press, 1979.

[266] H. B. de Aguiar, P. Gasecka, and S. Brasselet, "Quantitative analysis of light scattering in polarization-resolved nonlinear microscopy," *Optics Express*, vol. 23, p. 8960, Apr. 2015.

[267] J. M. Boggs, "Myelin basic protein: A multifunctional protein," *Cellular and Molecular Life Sciences CMLS*, vol. 63, pp. 1945–1961, June 2006.

[268] H. Takahashi, H. Igisu, and K. Suzuki, "The twitcher mouse: An ultrastructural study on the oligodendroglia," *Acta Neuropathologica*, vol. 59, pp. 159–166, Sept. 1983.

[269] World Health Organization, "Global burden of neurological disorders estimates and projections," in *Neurological Disorders: Public Health Challenges*, World Health Organization, 2007.

[270] N. E. Bharucha, N. (Canada), A. E. Bharucha, E. P. Bharucha, and L. . Bom), "Prevalence of peripheral neuropathy in the Parsi community of Bombay," *Neurology*, vol. 41, pp. 1315–1315, Jan. 1991.

[271] G. Savettieri, W. A. Rocca, G. Salemi, F. Meneghini, F. Grigoletto, L. Morgante, A. Reggio, V. Costa, M. A. Coraci, R. D. Perri, and F. t. S. N.-E. S. S. Group, "Prevalence of diabetic neuropathy with somatic symptoms A door-to-door survey in two Sicilian municipalities," *Neurology*, vol. 43, pp. 1115–1115, Jan. 1993.

[272] L. Monticelli and E. Beghi, "Chronic symmetric polyneuropathy in the elderly. A field screening investigation in two regions of Italy: Background and methods of assessment. The Italian General Practitioner Study Group (IGPSG).," *Neuroepidemiology*, vol. 12, no. 2, pp. 96–105, 1993.

[273] E. Beghi, L. Monticelli, and the Italian General Practitioner Study Group, "Chronic Symmetric Symptomatic Polyneuropathy in the Elderly," *Journal of Clinical Epidemiology*, vol. 51, pp. 697–702, Aug. 1998.

[274] E. W. Gregg, P. Sorlie, R. Paulose-Ram, Q. Gu, M. S. Eberhardt, M. Wolz, V. Burt, L. Curtin, M. Engelgau, and L. Geiss, "Prevalence of Lower-Extremity Disease in the U.S. Adult Population \>40 Years of Age With and Without Diabetes: 1999-2000 National Health and Nutrition Examination Survey," *Diabetes Care*, vol. 27, pp. 1591–1597, July 2004.

[275] F. Leblhuber, K. Schroecksnadel, M. Beran-Praher, H. Haller, K. Steiner, and D. Fuchs, "Polyneuropathy and dementia in old age: Common inflammatory and vascular parameters," *Journal of Neural Transmission*, vol. 118, pp. 721–725, Feb. 2011.

[276] D. Ceballos, J. Cuadras, E. Verdú, and X. Navarro, "Morphometric and ultrastructural changes with ageing in mouse peripheral nerve," *Journal of Anatomy*, vol. 195, pp. 563–576, Nov. 1999.

[277] M. Suzuki, "Peripheral neuropathy in the elderly," in *Handbook of Clinical Neurology*, vol. 115, pp. 803–813, Elsevier, 2013.

[278] N. Deshpande, E. J. Metter, S. Ling, R. Conwit, and L. Ferrucci, "Physiological correlates of age-related decline in vibrotactile sensitivity," *Neurobiology of Aging*, vol. 29, pp. 765–773, May 2008.

[279] Y. Fujimaki, S. Kuwabara, Y. Sato, S. Isose, K. Shibuya, Y. Sekiguchi, S. Nasu, Y. Noto, J. Taniguchi, and S. Misawa, "The effects of age, gender, and body mass index on amplitude of sensory nerve action potentials: Multivariate analyses," *Clinical Neurophysiology*, vol. 120, pp. 1683–1686, Sept. 2009.

[280] A. Jeronimo, C. A. D. Jeronimo, O. A. R. Filho, L. S. Sanada, and V. P. S. Fazan, "A morphometric study on the longitudinal and lateral symmetry of the sural nerve in mature and aging female rats," *Brain Research*, vol. 1222, pp. 51–60, July 2008.

[281] R. C. Melcangi, I. Azcoitia, M. Ballabio, I. Cavarretta, L. C. Gonzalez, E. Leonelli, V. Magnaghi, S. Veiga, and L. M. Garcia-Segura, "Neuroactive steroids influence peripheral myelination: A promising opportunity for preventing or treating age-dependent dysfunctions of peripheral nerves," *Progress in Neurobiology*, vol. 71, pp. 57–66, Sept. 2003.

[282] D. Shen, Q. Zhang, X. Gao, X. Gu, and F. Ding, "Age-related changes in myelin morphology, electrophysiological property and myelin-associated protein expression of mouse sciatic nerves," *Neuroscience Letters*, vol. 502, pp. 162–167, Sept. 2011.

[283] E. Verdú, M. Butí, and X. Navarro, "Functional changes of the peripheral nervous system with aging in the mouse," *Neurobiology of Aging*, vol. 17, pp. 73–77, Jan. 1996.

[284] E. Verdú, D. Ceballos, J. J. Vilches, and X. Navarro, "Influence of aging on peripheral nerve function and regeneration," *Journal of the Peripheral Nervous System*, vol. 5, pp. 191–208, Dec. 2000.

[285] J. D. Schmelzer and P. A. Low, "Electrophysiological studies on the effect of age on caudal nerve of the rat," *Experimental Neurology*, vol. 96, pp. 612–620, June 1987.

[286] A. Canta, A. Chiorazzi, V. A. Carozzi, C. Meregalli, N. Oggioni, M. Bossi, V. Rodriguez-Menendez, F. Avezza, L. Crippa, R. Lombardi, G. de Vito, V. Piazza, G. Cavaletti, and P. Marmiroli, "Age-related changes in the function and structure of the peripheral sensory pathway in mice," *Neurobiology of Aging*, vol. 45, pp. 136–148, Sept. 2016.

[287] J. P. Serra, *Image Analysis and Mathematical Morphology*. Academic Press, 1982.

[288] K. V. Mardia and P. E. Jupp, *Directional Statistics*. 1999.

[289] J. C. Ranasinghesagara, C. K. Hayakawa, M. A. Davis, A. K. Dunn, E. O. Potma, and V. Venugopalan, "Rapid computation of the amplitude and phase of tightly focused optical fields distorted by scattering particles," *Journal of the Optical Society of America A*, vol. 31, p. 1520, July 2014.

[290] E. Wolf, "Electromagnetic Diffraction in Optical Systems. I. An Integral Representation of the Image Field," *Proceedings of the Royal Society of London A: Mathematical, Physical and Engineering Sciences*, vol. 253, pp. 349–357, Dec. 1959.

[291] B. Richards and E. Wolf, "Electromagnetic Diffraction in Optical Systems. II. Structure of the Image Field in an Aplanatic System," *Proceedings of the Royal Society of London A: Mathematical, Physical and Engineering Sciences*, vol. 253, pp. 358–379, Dec. 1959.

[292] H. C. van de Hulst, *Light Scattering by Small Particles*. Wiley, 1957.

[293] M. S. Starosta and A. K. Dunn, "Three-Dimensional Computation of Focused Beam Propagation through Multiple Biological Cells," *Optics Express*, vol. 17, p. 12455, July 2009.

[294] T. Chomiak and B. Hu, "What Is the Optimal Value of the g-Ratio for Myelinated Fibers in the Rat CNS? A Theoretical Approach," *PLOS ONE*, vol. 4, no. 11, p. e7754, 13-nov-2009.

[295] A. Stanmore, S. Bradbury, and A. G. Weddell, "A quantitative study of peripheral nerve fibres in the mouse following the administration of drugs. 1. Age changes in untreated CBA mice from 3 to 21 months of age.," *Journal of Anatomy*, vol. 127, pp. 101–115, Sept. 1978.

[296] K. F. A. Ross, "The immersion refractometry of living cells by phase contrast and interference microscopy," in *General Cytochemical Methods* (J. F. Danielli, ed.), vol. 2, Academic Press, 1961.

[297] A. Rubio, J. L. Corkill, and M. L. Cohen, "Theory of graphitic boron nitride nanotubes," *Physical Review B*, vol. 49, pp. 5081–5084, Feb. 1994.

[298] N. G. Chopra, R. J. Luyken, K. Cherrey, V. H. Crespi, M. L. Cohen, S. G. Louie, and A. Zettl, "Boron Nitride Nanotubes," *Science*, vol. 269, pp. 966–967, Aug. 1995.

[299] J. Wang, C. H. Lee, and Y. K. Yap, "Recent advancements in boron nitride nanotubes," *Nanoscale*, vol. 2, pp. 2028–2034, Oct. 2010.

[300] C. Y. Zhi, Y. Bando, C. C. Tang, Q. Huang, and D. Golberg, "Boron nitride nanotubes: Functionalization and composites," *Journal of Materials Chemistry*, vol. 18, pp. 3900–3908, Aug. 2008.

[301] X. Chen, P. Wu, M. Rousseas, D. Okawa, Z. Gartner, A. Zettl, and C. R. Bertozzi, "Boron Nitride Nanotubes Are Noncytotoxic and Can Be Functionalized for Interaction with Proteins and Cells," *Journal of the American Chemical Society*, vol. 131, pp. 890–891, Jan. 2009.

[302] G. Ciofani, S. Danti, D. D'Alessandro, L. Ricotti, S. Moscato, G. Bertoni, A. Falqui, S. Berrettini, M. Petrini, V. Mattoli, and A. Menciassi, "Enhancement of Neurite Outgrowth in Neuronal-Like Cells following Boron Nitride Nanotube-Mediated Stimulation," *ACS Nano*, vol. 4, pp. 6267–6277, Oct. 2010.

[303] G. Ciofani, S. Danti, G. G. Genchi, B. Mazzolai, and V. Mattoli, "Boron Nitride Nanotubes: Biocompatibility and Potential Spill-Over in Nanomedicine," *Small*, vol. 9, pp. 1672–1685, May 2013.

[304] D. Lahiri, F. Rouzaud, T. Richard, A. K. Keshri, S. R. Bakshi, L. Kos, and A. Agarwal, "Boron nitride nanotube reinforced polylactide–polycaprolactone copolymer composite: Mechanical properties and cytocompatibility with osteoblasts and macrophages in vitro," *Acta Biomaterialia*, vol. 6, pp. 3524–3533, Sept. 2010.

[305] G. Ciofani, S. Danti, D. D'Alessandro, S. Moscato, and A. Menciassi, "Assessing cytotoxicity of boron nitride nanotubes: Interference with the MTT assay," *Biochemical and Biophysical Research Communications*, vol. 394, pp. 405–411, Apr. 2010.

[306] G. Ciofani, L. Ricotti, S. Danti, S. Moscato, C. Nesti, D. D'Alessandro, D. Dinucci, F. Chiellini, A. Pietrabissa, M. Petrini, and A. Menciassi, "Investigation of interactions between poly-l-lysine-coated boron nitride nanotubes and C2C12 cells: Up-take, cytocompatibility, and differentiation," *International Journal of Nanomedicine*, vol. 5, pp. 285–298, 2010.

[307] D. C. F. Soares, T. H. Ferreira, C. d. A. Ferreira, V. N. Cardoso, and E. M. B. de Sousa, "Boron nitride nanotubes radiolabeled with ^{99m}Tc: Preparation, physicochemical characterization, biodistribution study, and scintigraphic imaging in Swiss mice," *International Journal of Pharmaceutics*, vol. 423, pp. 489–495, Feb. 2012.

[308] G. Ciofani, S. Danti, S. Nitti, B. Mazzolai, V. Mattoli, and M. Giorgi, "Biocompatibility of boron nitride nanotubes: An up-date of in vivo toxicological investigation," *International Journal of Pharmaceutics*, vol. 444, pp. 85–88, Feb. 2013.

[309] L. Horváth, A. Magrez, D. Golberg, C. Zhi, Y. Bando, R. Smajda, E. Horváth, L. Forró, and B. Schwaller, "In Vitro Investigation of the Cellular Toxicity of Boron Nitride Nanotubes," *ACS Nano*, vol. 5, pp. 3800–3810, May 2011.

[310] G. Ciofani, S. Del Turco, A. Rocca, G. de Vito, V. Cappello, M. Yamaguchi, X. Li, B. Mazzolai, G. Basta, M. Gemmi, V. Piazza, D. Golberg, and V. Mattoli, "Cytocompatibility evaluation of gum Arabic-coated ultra-pure boron nitride nanotubes on human cells," *Nanomedicine*, vol. 9, pp. 773–788, Feb. 2014.

[311] Y.-J. Park, K.-S. Hwang, J.-E. Song, J. L. Ong, and H. Ralph Rawls, "Growth of calcium phosphate on poling treated ferroelectric BaTiO3 ceramics," *Biomaterials*, vol. 23, pp. 3859–3864, Sept. 2002.

[312] D. Staedler, T. Magouroux, R. Hadji, C. Joulaud, J. Extermann, S. Schwung, S. Passemard, C. Kasparian, G. Clarke, M. Gerrmann, R. L. Dantec, Y. Mugnier, D. Rytz, D. Ciepielewski, C. Galez, S. Gerber-Lemaire, L. Juillerat-Jeanneret, L. Bonacina, and J.-P. Wolf, "Harmonic Nanocrystals for Biolabeling: A Survey of Optical Properties and Biocompatibility," *ACS Nano*, vol. 6, pp. 2542–2549, Mar. 2012.

[313] G. Ciofani, S. Danti, D. D'Alessandro, S. Moscato, M. Petrini, and A. Menciassi, "Barium Titanate Nanoparticles: Highly Cytocompatible Dispersions in Glycol-chitosan and Doxorubicin Complexes for Cancer Therapy," *Nanoscale Research Letters*, vol. 5, pp. 1093–1101, May 2010.

[314] G. Ciofani, L. Ricotti, C. Canale, D. D'Alessandro, S. Berrettini, B. Mazzolai, and V. Mattoli, "Effects of barium titanate nanoparticles on proliferation and differentiation of rat mesenchymal stem cells," *Colloids and Surfaces B: Biointerfaces*, vol. 102, pp. 312–320, Feb. 2013.

[315] M. Dhanasekaran, S. Indumathi, R. P. Lissa, R. Harikrishnan, J. S. Rajkumar, and D. Sudarsanam, "A comprehensive study on optimization of proliferation and differentiation potency of bone marrow derived mesenchymal stem cells under prolonged culture condition," *Cytotechnology*, vol. 65, pp. 187–197, June 2012.

[316] J. M. Oliveira, R. A. Sousa, N. Kotobuki, M. Tadokoro, M. Hirose, J. F. Mano, R. L. Reis, and H. Ohgushi, "The osteogenic differentiation of rat bone marrow stromal cells cultured with dexamethasone-loaded carboxymethylchitosan/poly(amidoamine) dendrimer nanoparticles," *Biomaterials*, vol. 30, pp. 804–813, Feb. 2009.

[317] K. Yang, W. Cao, X. Hao, X. Xue, J. Zhao, J. Liu, Y. Zhao, J. Meng, B. Sun, J. Zhang, and X.-j. Liang, "Metallofullerene nanoparticles promote osteogenic differentiation of bone marrow stromal cells through BMP signaling pathway," *Nanoscale*, vol. 5, pp. 1205–1212, Jan. 2013.

[318] J.-T. Lee, J.-W. Jung, J.-Y. Choi, and T.-G. Kwon, "Enhanced bone morphogenic protein adenoviral gene delivery to bone marrow stromal cells using magnetic nanoparticle," *Journal of the Korean Association of Oral and Maxillofacial Surgeons*, vol. 39, no. 3, p. 112, 2013.

[319] J. C. Chen and C. R. Jacobs, "Mechanically induced osteogenic lineage commitment of stem cells," *Stem Cell Research & Therapy*, vol. 4, p. 107, Sept. 2013.

[320] D. H. Slentz, G. A. Truskey, and W. E. Kraus, "Effects of chronic exposure to simulated microgravity on skeletal muscle cell proliferation and differentiation," *In Vitro Cellular & Developmental Biology - Animal*, vol. 37, pp. 148–156, Mar. 2001.

[321] A. Adrian, K. Schoppmann, J. Sromicki, S. Brungs, M. von der Wiesche, B. Hock, W. Kolanus, R. Hemmersbach, and O. Ullrich, "The oxidative burst reaction in mammalian cells depends on gravity," *Cell Communication and Signaling*, vol. 11, p. 98, 2013.

[322] J. Van Loon, M. Van Laar, J. Korterik, F. Segerink, R. Wubbels, H. De Jong, and N. Van Hulst, "An atomic force microscope operating at hypergravity for in situ measurement of cellular mechano-response," *Journal of Microscopy*, vol. 233, pp. 234–243, Feb. 2009.

[323] S. J. Oldenburg, R. D. Averitt, S. L. Westcott, and N. J. Halas, "Nanoengineering of optical resonances," *Chemical Physics Letters*, vol. 288, pp. 243–247, May 1998.

[324] S. Liu, Z. Liang, F. Gao, J. Yu, S. Luo, J. N. Calata, and G. Lu, "A Facile Approach to the Synthesis of Gold Nanoshells with Near Infrared Responsive Properties," *Chinese Journal of Chemistry*, vol. 27, pp. 1079–1085, June 2009.

[325] W. Shi, Y. Sahoo, M. T. Swihart, and P. N. Prasad, "Gold Nanoshells on Polystyrene Cores for Control of Surface Plasmon Resonance," *Langmuir*, vol. 21, pp. 1610–1617, Feb. 2005.

[326] M. Hu, J. Chen, Z.-Y. Li, L. Au, G. V. Hartland, X. Li, M. Marquez, and Y. Xia, "Gold nanostructures: Engineering their plasmonic properties for biomedical applications," *Chemical Society Reviews*, vol. 35, pp. 1084–1094, Oct. 2006.

[327] J. Yguerabide and E. E. Yguerabide, "Light-Scattering Submicroscopic Particles as Highly Fluorescent Analogs and Their Use as Tracer Labels in Clinical and Biological Applications: I. Theory," *Analytical Biochemistry*, vol. 262, pp. 137–156, Sept. 1998.

[328] J. Yguerabide and E. E. Yguerabide, "Light-Scattering Submicroscopic Particles as Highly Fluorescent Analogs and Their Use as Tracer Labels in Clinical and Biological Applications: II. Experimental Characterization," *Analytical Biochemistry*, vol. 262, pp. 157–176, Sept. 1998.

[329] C. B. Raub, E. J. Orwin, and R. Haskell, "Immunogold labeling to enhance contrast in optical coherence microscopy of tissue engineered corneal constructs," in *26th Annual International Conference of the IEEE Engineering in Medicine and Biology Society, 2004. IEMBS '04*, vol. 1, pp. 1210–1213, Sept. 2004.

[330] K. Sokolov, M. Follen, J. Aaron, I. Pavlova, A. Malpica, R. Lotan, and R. Richards-Kortum, "Real-Time Vital Optical Imaging of Precancer Using Anti-Epidermal Growth Factor Receptor Antibodies Conjugated to Gold Nanoparticles," *Cancer Research*, vol. 63, pp. 1999–2004, Jan. 2003.

[331] T. D. Yang, W. Choi, T. H. Yoon, K. J. Lee, J.-S. Lee, S. H. Han, M.-G. Lee, H. S. Yim, K. M. Choi, M. W. Park, K.-Y. Jung, and S.-K. Baek, "Real-time phase-contrast imaging of photothermal treatment of head and neck squamous cell carcinoma: An in vitro study of macrophages as a vector for the delivery of gold nanoshells," *Journal of Biomedical Optics*, vol. 17, no. 12, pp. 128003–128003, 2012.

[332] R. J. Bernardi, A. R. Lowery, P. A. Thompson, S. M. Blaney, and J. L. West, "Immunonanoshells for targeted photothermal ablation in medulloblastoma and glioma: An in vitro evaluation using human cell lines," *Journal of Neuro-Oncology*, vol. 86, pp. 165–172, Sept. 2007.

[333] J. A. Schwartz, A. M. Shetty, R. E. Price, R. J. Stafford, J. C. Wang, R. K. Uthamanthil, K. Pham, R. J. McNichols, C. L. Coleman, and J. D. Payne, "Feasibility Study of Particle-Assisted Laser Ablation of Brain Tumors in Orthotopic Canine Model," *Cancer Research*, vol. 69, pp. 1659–1667, Feb. 2009.

[334] J. M. Stern, J. Stanfield, W. Kabbani, J.-T. Hsieh, and J. A. Cadeddu, "Selective Prostate Cancer Thermal Ablation With Laser Activated Gold Nanoshells," *The Journal of Urology*, vol. 179, pp. 748–753, Feb. 2008.

[335] A. M. Gobin, D. P. O'Neal, D. M. Watkins, N. J. Halas, R. A. Drezek, and J. L. West, "Near infrared laser-tissue welding using nanoshells as an exogenous absorber," *Lasers in Surgery and Medicine*, vol. 37, pp. 123–129, Aug. 2005.

[336] G. B. Braun, A. Pallaoro, G. Wu, D. Missirlis, J. A. Zasadzinski, M. Tirrell, and N. O. Reich, "Laser-Activated Gene Silencing via Gold Nanoshell-siRNA Conjugates," *ACS Nano*, vol. 3, pp. 2007–2015, July 2009.

[337] L. O. Svaasand, C. J. Gomer, and E. Morinelli, "On the physical rationale of laser induced hyperthermia," *Lasers in Medical Science*, vol. 5, pp. 121–128, June 1990.

[338] X. Huang, P. K. Jain, I. H. El-Sayed, and M. A. El-Sayed, "Plasmonic photothermal therapy (PPTT) using gold nanoparticles," *Lasers in Medical Science*, vol. 23, pp. 217–228, Aug. 2007.

[339] M. Yonezawa, T. Otsuka, N. Matsui, H. Tsuji, K. H. Kato, A. Moriyama, and T. Kato, "Hyperthermia induces apoptosis in malignant fibrous histiocytoma cells in vitro," *International Journal of Cancer*, vol. 66, pp. 347–351, May 1996.

[340] R. D. Issels, "Hyperthermia adds to chemotherapy," *European Journal of Cancer*, vol. 44, pp. 2546–2554, Nov. 2008.

[341] B. V. Harmon, A. M. Corder, R. J. Collins, G. C. Gobé, J. Allen, D. J. Allan, and J. F. R. Kerr, "Cell Death Induced in a Murine Mastocytoma by 42–47°C Heating in Vitro: Evidence that the Form of Death Changes from Apoptosis to Necrosis Above a Critical Heat Load," *International Journal of Radiation Biology*, vol. 58, pp. 845–858, Jan. 1990.

[342] F.-Y. Cheng, C.-T. Chen, and C.-S. Yeh, "Comparative efficiencies of photothermal destruction of malignant cells using antibody-coated silica@Au nanoshells, hollow Au/Ag nanospheres and Au nanorods," *Nanotechnology*, vol. 20, no. 42, p. 425104, 2009.

[343] S.-Y. Liu, Z.-S. Liang, F. Gao, S.-F. Luo, and G.-Q. Lu, "In vitro photothermal study of gold nanoshells functionalized with small targeting peptides to liver cancer cells," *Journal of Materials Science: Materials in Medicine*, vol. 21, pp. 665–674, Oct. 2009.

[344] E. S. Day, P. A. Thompson, L. Zhang, N. A. Lewinski, N. Ahmed, R. A. Drezek, S. M. Blaney, and J. L. West, "Nanoshell-mediated photothermal therapy improves survival in a murine glioma model," *Journal of Neuro-Oncology*, vol. 104, pp. 55–63, Nov. 2010.

[345] L. C. Kennedy, L. R. Bickford, N. A. Lewinski, A. J. Coughlin, Y. Hu, E. S. Day, J. L. West, and R. A. Drezek, "A New Era for Cancer Treatment: Gold-Nanoparticle-Mediated Thermal Therapies," *Small*, vol. 7, pp. 169–183, Jan. 2011.

[346] J. M. Stern and J. A. Cadeddu, "Emerging use of nanoparticles for the therapeutic ablation of urologic malignancies," *Urologic Oncology: Seminars and Original Investigations*, vol. 26, pp. 93–96, Jan. 2008.

[347] B. H. Cumpston, S. P. Ananthavel, S. Barlow, D. L. Dyer, J. E. Ehrlich, L. L. Erskine, A. A. Heikal, S. M. Kuebler, I.-Y. S. Lee, D. McCord-Maughon, J. Qin, H. Röckel, M. Rumi, X.-L. Wu, S. R. Marder, and J. W. Perry, "Two-photon polymerization initiators for three-dimensional optical data storage and microfabrication," *Nature*, vol. 398, pp. 51–54, Mar. 1999.

[348] K. C. Hribar, P. Soman, J. Warner, P. Chung, and S. Chen, "Light-assisted direct-write of 3D functional biomaterials," *Lab Chip*, vol. 14, no. 2, pp. 268–275, 2014.

[349] M. T. Raimondi, S. M. Eaton, M. M. Nava, M. Laganà, G. Cerullo, and R. Osellame, "Two-photon laser polymerization: From fundamentals to biomedical application in tissue engineering and regenerative medicine," *Journal of Applied Biomaterials & Functional Materials*, vol. 10, no. 1, pp. 55–65, 2012.

[350] M. Farsari, M. Vamvakaki, and B. N. Chichkov, "Multiphoton polymerization of hybrid materials," *Journal of Optics*, vol. 12, no. 12, p. 124001, 2010.

[351] N. Royo-Gascon, M. Wininger, J. I. Scheinbeim, B. L. Firestein, and W. Craelius, "Piezoelectric Substrates Promote Neurite Growth in Rat Spinal Cord Neurons," *Annals of Biomedical Engineering*, vol. 41, pp. 112–122, Aug. 2012.

[352] Y.-S. Lee and T. L. Arinzeh, "The Influence of Piezoelectric Scaffolds on Neural Differentiation of Human Neural Stem/Progenitor Cells," *Tissue Engineering Part A*, vol. 18, pp. 2063–2072, May 2012.

[353] H.-F. Guo, Z.-S. Li, S.-W. Dong, W.-J. Chen, L. Deng, Y.-F. Wang, and D.-J. Ying, "Piezoelectric PU/PVDF electrospun scaffolds for wound healing applications," *Colloids and Surfaces B: Biointerfaces*, vol. 96, pp. 29–36, Aug. 2012.

[354] X. Wang, J. Song, J. Liu, and Z. L. Wang, "Direct-Current Nanogenerator Driven by Ultrasonic Waves," *Science*, vol. 316, pp. 102–105, Apr. 2007.

[355] A. Marino, C. Filippeschi, G. G. Genchi, V. Mattoli, B. Mazzolai, and G. Ciofani, "The Osteoprint: A bioinspired two-photon polymerized 3-D structure for the enhancement of bone-like cell differentiation," *Acta Biomaterialia*, vol. 10, pp. 4304–4313, Oct. 2014.

[356] H. G. Breunig, M. Weinigel, R. Bückle, M. Kellner-Höfer, J. Lademann, M. E. Darvin, W. Sterry, and K. König, "Clinical coherent anti-Stokes Raman scattering and multiphoton tomography of human skin with a femtosecond laser and photonic crystal fiber," *Laser Physics Letters*, vol. 10, no. 2, p. 025604, 2013.

[357] M. Weinigel, H. G. Breunig, M. Kellner-Höfer, R. Bückle, M. E. Darvin, M. Klemp, J. Lademann, and K. König, "In vivo histology: Optical biopsies with chemical contrast using clinical multiphoton/coherent anti-Stokes Raman scattering tomography," *Laser Physics Letters*, vol. 11, no. 5, p. 055601, 2014.

[358] M. Weinigel, H. G. Breunig, A. Uchugonova, and K. König, "Multipurpose nonlinear optical imaging system for in vivo and ex vivo multimodal histology," *Journal of Medical Imaging*, vol. 2, no. 1, pp. 016003–016003, 2015.

[359] F. Légaré, C. L. Evans, F. Ganikhanov, and X. S. Xie, "Towards CARS Endoscopy," *Optics Express*, vol. 14, no. 10, p. 4427, 2006.

[360] E. Bélanger, J. Crépeau, S. Laffray, R. Vallée, Y. De Koninck, and D. Côté, "Live animal myelin histomorphometry of the spinal cord with video-rate multimodal nonlinear microendoscopy.," *J Biomed Opt*, vol. 17, p. 021107, Feb. 2012.

INDEX

autofluorescence, 2, 9

barium titanate core - gold shell nanoparticles, 49, 98, 99
barium titanate nanoparticles, 25, 94, 96, 97, 99–101
boron nitride nanotubes, 93–95
brain, 29, 31, 56, 57, 85, 87

compensation lens, 33, 34, 39, 40
confocal microscopy, 1, 16, 67

electronic microscopy, 16, 49, 62, 67
endoscopy, 106
erythrocyte ghost, 17, 19, 20

fingerprint region, 8–10
Four Wave Mixing, 3–6, 12, 21, 25, 44–49, 95, 97, 100, 101

geologic samples, 9, 11

histochemistry, 16

immunofluorescence, 1, 16, 67

Krabbe disease, 15, 67, 79, 104
Krebs-Henseleit buffer, 42, 54, 66, 77

liver, 10
lysophosphatidylcholine, 16, 20, 21, 62, 63, 65

magnetic resonance imaging, 16, 56
multiple sclerosis, 15, 16, 54, 105

nanocomposite scaffold, 99–101
neuropathy, 16, 79, 80, 105
non resonant background, 6, 7, 9, 53, 66, 78

plant samples, 9, 11, 17, 105

Raman microscopy, 2, 7
Ranvier node, 12, 13

saltatory conduction, 12
Schmidt-Lanterman incisures, 53, 54
Schwann cell, 12, 67, 76
sciatic nerve, 20, 53, 54, 56, 65–67, 69, 70, 75, 76, 79, 81, 82, 85, 103, 104
Second Harmonic Generation, 2, 17, 25, 94, 100
spinal cord, 12, 20, 42, 43, 53, 55
Stimulated Raman Scattering, 8
Sum Frequency Generation, 2, 25, 44–49, 94, 95, 97, 100, 101
supercontinuum generator, 23, 24

Third Harmonic Generation, 2, 3
third order susceptibility tensor, 3, 4, 6, 17, 26, 28, 58, 59, 85, 86
twitcher mouse, 67–79, 104
two-photon
  lithography, 99, 100
  microscopy, 2, 7, 16, 17, 36